UNIVERSITÀ DI PARMA

Dottorato di Ricerca in Fisica

Ciclo XXX

Novel TCO contacts for fabrication of CIGS bifacial solar cells

Coordinator:
Prof. Cristiano Viappiani

Supervisors:
Prof. Roberto Fornari
Dott. Edmondo Gilioli

Candidate: Nicholas Cavallari

A mio papà

Abstract

Object of this thesis is the development of viable technological processes for the fabrication of efficient bifacial solar cells. To this extent, a great effort was first made in order to prepare transparent conductive electrodes based on different oxide compounds and, secondly, to deposit the absorber and form the cell junction on such transparent back contacts. The new technological procedures were coupled to extensive simulation and characterization of both individual materials and working devices, which provided the necessary feedback for technology optimization.

The bifacial solar cells (BFSC) considered in this thesis are all based on the compound $Cu(In_{1-x},Ga_x)Se_2$ (CIGS), which is a very efficient light absorber. A major task of this work consisted in replacing the standard molybdenum back contact with a suitable transparent conductive oxide (TCO), and then tuning the physical properties of both TCO and absorber in order to maximize the transport of the photo-generated carriers across their interface.

For all studied devices, both the absorber and the back TCO were grown via low-temperature pulsed electron deposition (LTPED). LTPED is a non-equilibrium deposition technique that relies on the ablation of a ceramic target by short and high-energy electron pulses. At IMEM-CNR in Parma, CIGS is deposited via LTPED at T=250°C. As it will be shown in the thesis, thanks to this low T (compared to alternative growth methods), high-quality CIGS may be obtained without post-deposition selenization on alternative and novel substrates, including TCOs.

Conventional and new TCOs deposited by LTPED on glass were investigated in order to correlate their optical, electrical, morphological, compositional and structural properties with deposition parameters. All materials exhibited excellent optical transmittance when deposited at a substrate temperature of 100°C, but differed considerably from the point of view of electrical parameters. Only n-type TCOs provided the needed electrical conductivity, therefore a detailed study of the p-type CIGS/n-type TCO interface was carried out to identify in which conditions this junction exhibits an ohmic-like behavior (thanks to pronounced tunneling).

CIGS-based BFSCs were then fabricated using the best TCOs as back contacts. Among all important results, a most remarkable achievement of this study was that aluminum zinc oxide (AZO) can be used as efficient back electrode. Actually, the existing literature states that at the deposition temperature of standard methods (550°C) a thin insulating Ga_2O_3 layer forms between CIGS and AZO, which impedes an efficient current flow. In this work, it is demonstrated that LTPED allows the deposition of CIGS on AZO without formation

of the detrimental Ga_2O_3 interlayer, thus opening new routes towards building integrated photovoltaic applications, considering that AZO is a low-cost and non-toxic material.

The positive results presented above were achieved in small-area cells, so that they need to be implemented also in large-area devices. A novel approach to large-area BFSCs was hence investigated in the course of the PhD work, namely the deposition of selected TCO on a glass substrate with a pre-deposited metallic grid. This was seen to ensure a more efficient collection of the photo-generated carriers and to reduce power loss at the back contact. As a matter of fact, a prototype with this architecture and four-times larger area exhibited the same efficiency of a small cell with no metallic grid. This is very encouraging in view of the practical application of TCOs to bifacial technology.

Index

Introduction

$Cu(In_{1-x},Ga_x)Se_2$ (CIGS) is a p-type semiconductor used as light absorber in thin-film solar cells. This compound displays theoretical photovoltaic conversion efficiency close to 30% and possesses the highest absorption coefficient among all semiconductors, therefore it is the most promising material for thin-film photovoltaic applications such as flexible devices, building integrated photovoltaics, deposition on alternative substrates, solar cells for space application.

In the last years, CIGS-based solar cells have reached efficiency higher than 22% in laboratory-scale devices and 17% for photovoltaic modules on standard glass substrates. However, the conventional and widely used CIGS deposition techniques, like thermal co-evaporation or sputtering, require high temperatures (>500°C) to grow good-quality CIGS layers and, generally, a post-deposition treatment is needed to adjust film stoichiometry which involves toxic gases such as H_2Se of H_2S. For these reasons, the deposition of CIGS on alternative substrates (plastic, ultrathin glass, etc.) is still less mature even if promising results have been obtained on laboratory-scale devices. Clearly, several advantages would be possible with a deposition technique working both at low temperature (cost and time reduction, utilization of alternative substrates) and without hazardous gases (environmental concerns).

At IMEM-CNR in Parma, a novel technique called Low-Temperature Pulsed Electron Deposition (LTPED) has been developed to realize CIGS-based solar cells. LTPED relies on the ablation of a ceramic target by short and high-energy electron beams generated by an electron gun working in pulsed mode. The power density of these pulses is so high that the target material is converted into a cloud of plasma independently of its thermodynamic properties: the non-equilibrium nature of the transformation allows for a very fast evaporation even for materials with an incongruent melting point. For this reason, the stoichiometry of the target is practically conserved in the plasma cloud and in the growing film, making LTPED suitable to deposit ternary or quaternary compounds, such as CIGS, with a complicated phase diagram. In fact, LTPED allows the fabrication of high-efficiency CIGS-based solar cells using a single-stage process working at a substrate temperature as low as 250°C, much lower than the temperature used in the conventional techniques. So far, non-optimized devices have reached a photovoltaic conversion efficiency of 17% without the employment of gallium grading or anti-reflection coating. A promising consequence of the very low temperature set in LTPED is that CIGS can be deposited on various alternative and novel substrates. In particular, replacing the standard opaque substrate of a CIGS-based solar cell with a transparent conductive oxide (TCO) allows the fabrication of bifacial solar cells.

A bifacial solar cell (BFSC) is a device capable of absorbing light both from its front and back sides. It is achieved by replacing the standard metallic back electrode by a TCO contact, which allows direct or diffused sunlight to reach the absorber also from the back of the cell. With respect to a conventional one-side structure, a BFSC can increase the generated current up to 20%. The typical field of application of these devices is building integrated photovoltaics (BIPV), in which photovoltaic materials are used to replace or integrate conventional building features like rooftops or facades. In fact, ideal installations of a BFSC would be in vertical elements whose front and back surfaces are alternatively exposed to sunlight illumination or in situations where the back side can take advantage of reflected/diffused light from the surrounding environment. The majority of BFSCs are silicon-based devices already reaching remarkably high efficiencies; however, a thin-film BFSC would have several advantages compared to a silicon-based one, like the possibility of deposition on flexible substrates and the savings of raw materials.

At present, literature reports data for CIGS-based BFSC realized on Indium Tin Oxide (ITO), Fluorine Tin Oxide (FTO) and Aluminum Zinc Oxide (AZO). The first two electrodes already achieved relatively high performances with conversion efficiencies up to 15%. On the contrary, devices realized so far on AZO showed almost zero efficiency. The reason for this failure was identified to be the formation of a thin Ga_2O_3 insulating layer of at the interface CIGS/AZO, which acts as blocking agent for the photo-generated current. The insulating layers form at the usual deposition T>500°C of standard growth methods. Starting from this experimental evidence, it was decided to assess the suitability of LTPED for realization of CIGS bifacial cells on AZO back contact. Indeed, AZO is a low-cost and no-toxic alternative to ITO and FTO, and the achievement of a working BFSC on AZO would be a very important innovation in the field of BIPV.

The target of this thesis is to fabricate CIGS-based BFSC on different TCOs as back contacts. To achieve this goal, two key aspect of a BFSC were investigated and optimized: the TCO itself and the back interface CIGS/TCO. It will be shown that, thanks to these developments, it was possible to realize high efficiency BFSCs with performances comparable or even superior to state-of-the-art.

The first chapter describes the basic principles of solar cells, and then discusses the properties of CIGS and the standard architecture of a CIGS-based solar cell. Chapter 2 reports on the deposition of different TCOs via LTPED while chapter 3 deals with the properties of these TCOs, assessed by a large variety of characterization methods, also made in cooperation with external groups. Finally, chapter 4 describes the fabrication of CIGS-based BFSC and presents an original approach to obtain large area BFSCs. The thesis terminates with the closing remarks and work perspectives.

The first part of the experimental activity focused on the deposition and the characterization of TCO realized via LTPED. Optical, electrical, morphological, compositional and structural properties of the deposited TCO were correlated in detail with deposition parameters in order to find the optimal experimental setup for every material. Then, the various TCO were optically and electrically compared in view of their application as back contacts for BFSCs. Selected materials exhibited optical transmittance above 85% (between 400 nm

and 1200 nm) and electrical resistivity lower than $3.5 \cdot 10^{-4}\ \Omega \cdot cm$ when deposited at a substrate temperature of 100°C. This important achievement shows that LTPED is capable of depositing high quality TCOs at a very low temperature.

Regarding the choice of the TCO to be developed, two different approaches were followed in parallel:

- Deposition and study of a novel p-type TCO with the chemical formula $CuGaO_2$: this material would be an ideal candidate to be used as a back contact in a CIGS-based BFSC since it should form an ohmic contact when coupled with CIGS.
- Deposition of conventional n-type TCO (ITO and doped zinc oxide) at very low temperatures (T<200°C). Different elements were studied as dopants in zinc oxide: aluminum (the most used dopant), gallium and indium, and their concentration were modified accordingly to the optimization process.

As it will be discussed in detail in the chapter 2, the deposition of the right phase of $CuGaO_2$ proved to be an extremely complicated task. Furthermore, the conductivity was always very low so that it was impossible to exploit this compound for the subsequent fabrication of BFSCs. Therefore, most of the experimental activity deals with the realization of CIGS-based BFSCs deposited on ITO, AZO and ZnO:Ga. All three TCOs are n-doped, and the deposition of CIGS onto an n-doped semiconductor requires the formation of a tunnel junction. So, a preliminary theoretical simulation of the CIGS/TCO interface was conducted to identify in which situation this junction exhibits an ohmic-like behavior. The introduction of a very thin layer of NaF and the subsequent electrical measurements performed on the structures confirm the ohmicity of the electrical contact: this is a fundamental requirement to realize a working BFSC.

As explained in detail in chapter 4, this study proves that CIGS-based BFSC fabricated by LTPED on ITO, AZO and ZnO:Ga back contacts show efficiencies exceeding the current literature values. Remarkably, during LTPED deposition of CIGS on AZO no formation of gallium oxide at the interface CIGS/AZO was observed, as confirmed by experimental characterization.

The last section of chapter 4 proposes a novel approach to realize large-area BFSCs: the deposition of the TCO on a glass substrate containing a metallic grid, which would ensure a more efficient collection of the photo-generated carriers resulting in a reduced power loss from the back contact. A preliminary device employing this architecture showed very promising results: it displayed efficiency comparable to a structure with no metallic grid over a four times bigger area.

Chapter 1: CIGS-based solar cells

This chapter features a general introduction of CIGS-based solar cells. The discussion begins with an introductive paragraph describing the most important concepts of photovoltaic effects and solar cells. Then, the material properties of CIGS as well as the typical structure of a CIGS-based solar cell realized at IMEM-CNR are reported.

1.1 Introduction

The problem of energy generation is one of the most important challenges that the society will have to deal with in the upcoming years. In fact, projections show that the world power consumption will raise up by 63% in the next 25 years [1] going from the current value of 17.7 TW to about 28 TW. Actually, the majority of the world electric energy is obtained burning fossil fuels [2] which increases the concentration of CO_2 in the atmosphere and the pollution in general. The whole scientific community agrees that greenhouse gases are responsible for the global warming that our planet is experiencing in the last 20-30 years, and facing the consequences of global warming will be another critical challenge for the society of this century. This topic is so important that almost all countries decided to sign up the Paris Agreement in 2015 in view of beginning a gradual reduction of the greenhouse emissions [3]. From these considerations, it is clear that many efforts are made in finding energy sources that do not damage the environment and, at the same time, are low-cost and locally available.

The most promising alternative sustainable energy source is photovoltaic (PV). Actually, electricity produced by PV has achieved a generation cost below 0.03 USD/kWh [4] making PV a competitive alternative to fossil fuels or other energy sources under favorable market opportunities and with adequate insolation. In fact, the total globally installed PV capacity was estimated to be above 300 GW at the end of 2016 [5], with an impressive increase of 75.4 GW with respect to 2015 and more than 100 GW with respect to 2014. This result is primarily due to the recent and very rapid growing of Asian countries, as indicated by figure 1.1. Actually, 1.8% of the world's energy generation is covered by PV, with terrific perspectives of increase in the following years.

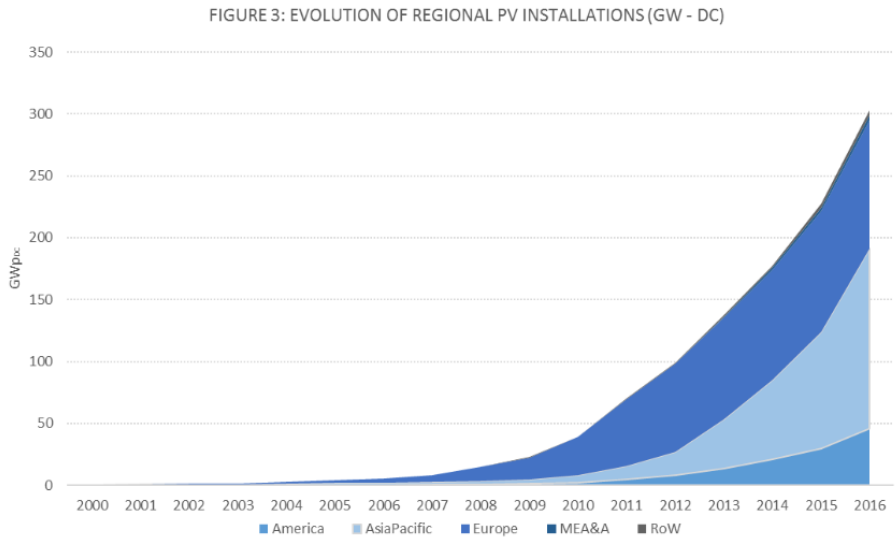

Figure 1.1: Worldwide installed PV capacity at the end of 2016, taken from [5]. MEA&A and Row stands for Middle East and Africa and Rest of the World.

The other side of the coin is that a large part of the global PV market is still driven by financial incentives, and countries that have reduced those incentives have inevitably experienced a much less increase of their installed PV.

For this reason, current research is focused on developing specific technologies aiming at novel applications to expand the PV market: building integrated photovoltaic (BIPV), portable solar cells, devices for solar concentrators, and so on. Among these innovative applications, BIPV is probably the most interesting one, since commercial, residential and public buildings actually uses more than 60% of the electric power in EU and about 75% in the USA. European Union has even identified BIPV as one of the most important PV market in the next 5-10 years and has already funded several research projects aiming at developing BIPV applications or market predictions.

While actually silicon panels do, and undoubtedly will, dominate the solar market of large utility-scale power plants, the most suitable technology for BIPV application is probably thin-film PV, thanks to its low manufacturing cost, its reduced raw materials usage and its wide range of possible applications in BIPV features like facades, windows, rooftops, covers, and so on. Research on thin-film PV has been active for more than 30 years, and nowadays efficiencies comparable to silicon-based devices have been achieved by the two main thin-film absorbers (CdTe and Cu(In,Ga)Se2 (CIGS)) and, more recently, by the new perovskite-based materials and Cu2ZnSnSe4 (CZTS) which however still faces important problems like long-term stability or hysteresis in J-V curves. The next page reports the trend of the best laboratory-scale efficiency of many PV technologies as summarized by the National Renewable Energy Laboratory on externally-certificated results, as per October 2017 report [6].

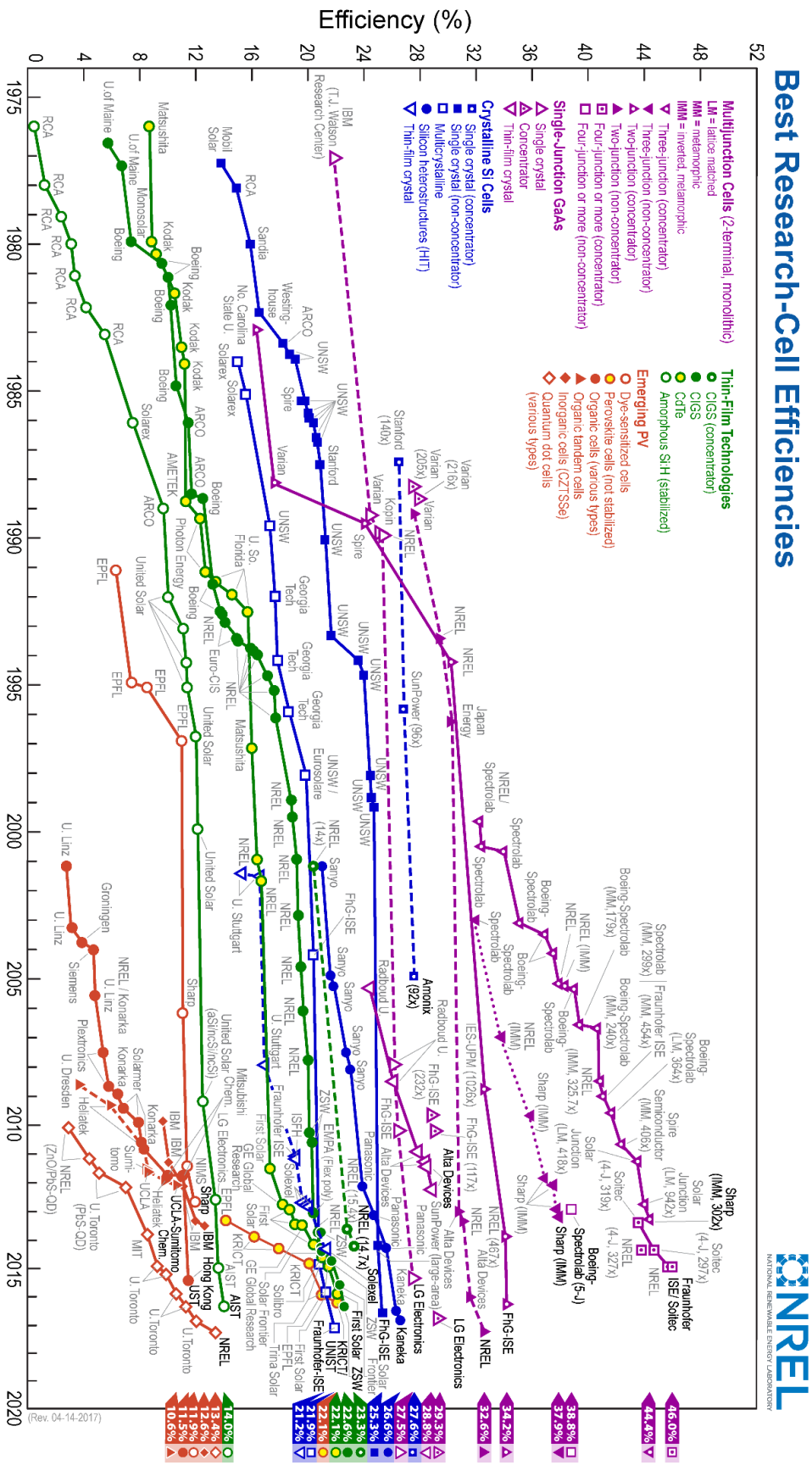

Figure 1.2: Best lab-scale efficiency of different PV technologies, as reported in [6].

1.2 General theory of a solar cell

1.2.1 The p-n junction

A p-n junction is the interface between two semiconductors with different doping, one p-type and one n-type, each with carrier concentration N_A and N_D, respectively. In this situation, in proximity of the interface free electrons diffuse from the n-type semiconductor to the p-type material, forming negatively charged ions while leaving behind ions with a positive charge. As a consequence, near the p-n junction the materials lose their electrical neutrality and most of their mobile carriers, creating what it is known as "space-charge region" or "depletion layer". The unscreened charge on the positive and negative ions creates an electric field (and a built in potential ΔV), and at the equilibrium condition is counterbalance the diffusion of more free carriers. Situation is depicted in figure 1.3(a). In addition, the Fermi Level E_F, defined as the highest occupied energy level at 0K, must remain constant across the junction, causing a bending in both the valence band and the conduction band as sketched in figure 1.3(b).

The width of the depletion region W is inversely proportional to N_A and N_D according to:

$$W = \sqrt{\frac{2\varepsilon}{q}\Delta V\left(\frac{1}{N_D}+\frac{1}{N_A}\right)}$$

where ε is the dielectric constant of the material and q the elementary charge.

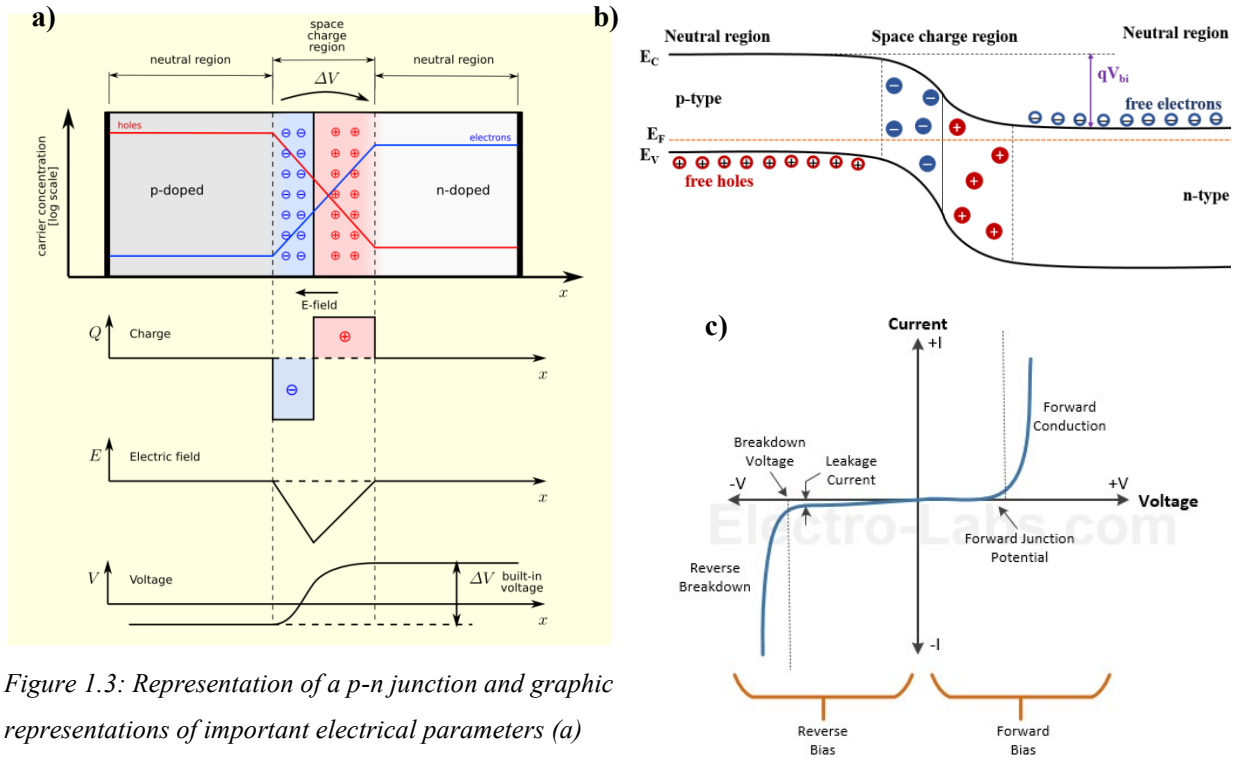

Figure 1.3: Representation of a p-n junction and graphic representations of important electrical parameters (a) and band bending (b) across the junction and typical I-V curve (c).

The p-n junction is the basis of many modern electronic devices like diodes, solar cells, LEDs, transistors and integrated circuits. In an electrical circuit, a p-n junction can be connected either in forward bias or in reverse bias.

In forward bias the p-side of the junction is connected to a positive terminal, and the n-side to a negative terminal. In this situation, electrons injected in the n-type region are pushed toward the junction where they start to neutralize the depletion layer and diminish its width. As the applied voltage increases, the space-charge region eventually becomes sufficiently small to be crossed by the majority carriers, giving rise to a current flowing through the device. On the contrary, in reverse bias the width of the depletion layer increases as increasing applied voltages and only a negligible current flows, originated from the diffusion of the minority carriers. However, at a critical negative voltage the space-charge region breaks down and a big current starts to flow very rapidly. The typical J-V of a p-n junction is represented in figure 1.2(c) and in forward bias it is modeled by the Shockley equation:

$$J = J_0\left(e^{\frac{qV}{nk_bT}} - 1\right)$$

where I and V are respectively the current and the voltage across the junction, q is the elementary charge, n a number called "ideality factor" which account for the difference between a real junction and an ideal junction, T is the temperature, k_b the Boltzmann's constant, J_0 the reverse bias saturation current defined as

$$J_0 = e\left(\sqrt{\frac{D_p}{\tau_p}}\frac{n_i^2}{N_D} + \sqrt{\frac{D_n}{\tau_n}}\frac{n_i^2}{N_A}\right)$$

where $D_{n,p}$ and $\tau_{n,p}$ are the diffusion coefficients and the lifetimes of electrons and holes respectively, $N_{D,A}$ are the donor and acceptor concentrations at the n side and p side respectively, n_i^2 is the intrinsic carrier concentration (the carrier concentration in semiconductor with no external doping).

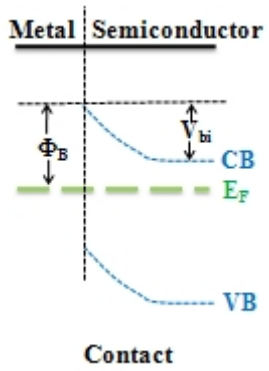

Figure 1.4: Band diagram in a Schottky barrier for electrons.

A very similar case to a p-n junction is a Schottky barrier, hence the potential energy barrier for carriers at a metal-semiconductor interface: this junction has a rectifying behavior and can be used as a diode. The energy bands at a Schottky barrier for electrons are depicted in figure 1.4. From here, one can define the barrier height Φ_B as the difference between the Fermi level in the metal and the junction valence band of the semiconductor. If is sufficiently low, the junction behaves as an ohmic contact, otherwise the semiconductor is depleted near the interface and rectification prevails. In first approximation, Φ_B can be obtained from the difference between the metal work function and the semiconductor electron or hole affinity:

$$\Phi_B \sim \Phi_{Metal} - \chi_{semiconductor}$$

1.2.2 Heavily doped p-n junction

A semiconductor with a carrier concentration greater than its density of available states in the conduction band (or the valence band) is defined as degenerate. In this situation, the Fermi level lies within the conduction band (or the valence band for p-type semiconductors) and the material behaves essentially as a metal.

If two degenerate semiconductors are used in a p-n junction, the resulting depletion layer has a very small width, with typical values around 10 nm. Figure 1.5 summarizes carrier transport in a heavily doped p-n junction. In this situation, if no external bias is supplied (step 1) the conduction band of the n-type material overlaps with the valence band of the p-type material, resulting in free electrons and holes with almost the same energy levels. An equal number of particles tunnels in the opposite directions, so the total net current is null. Under a small forward bias (step 2) there is a finite probability that a carrier can cross the p-n junction via quantum tunneling rather even it does not have enough energy for barrier overcoming, creating a small forward current. As the external bias increase (step 3), there is an increased overlapping of the conduction and valence bands producing a maximum current flow. The band overlapping diminishes for even greater applied voltage (step 4) causing a small reduction in the tunnel current, and eventually (step 5) the structure begins to operate as a normal p-n junction, with electrons moving by conduction rather than by tunneling. Nowadays, tunnel junctions are extensively employed in tunnel diodes, in multi-junction solar cells and in superconducting tunnel junctions.

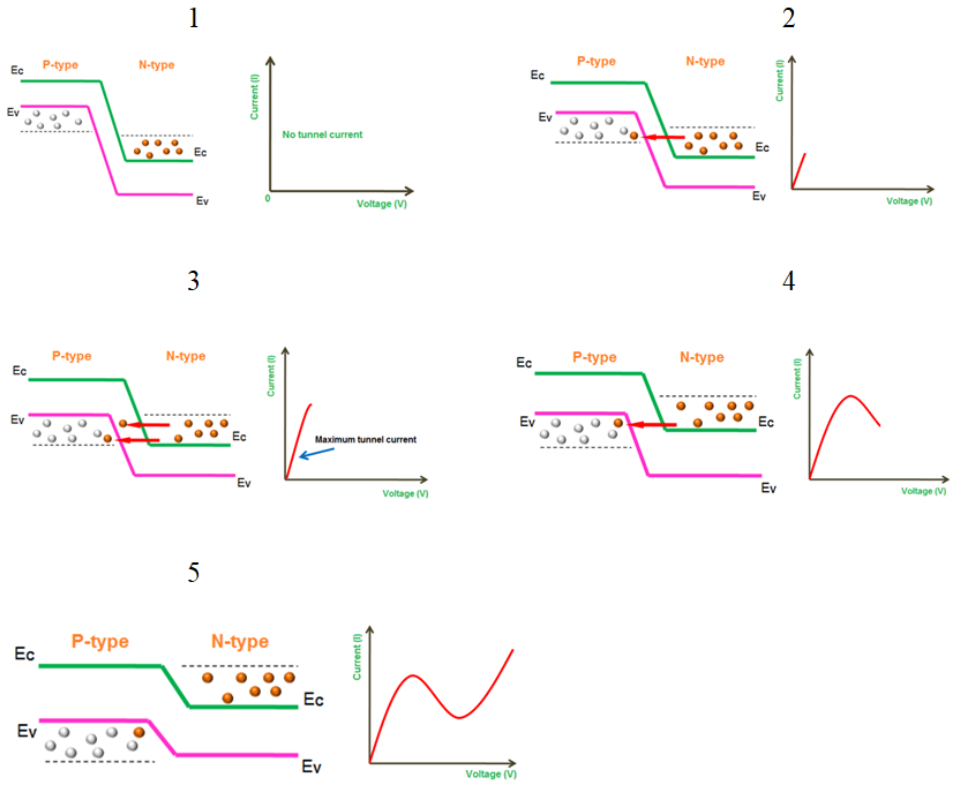

Figure 1.5: Carrier transport and corresponding I-V through a tunnel junction with increasing applied voltage.

1.3 Principles of a solar cell

A solar cell is a device that converts electromagnetic radiation into electrical current thanks to the photovoltaic effect. Consider a semiconductor material with energy gap E_G and a photon with energy $E \geq E_G$, and assume that the latter is absorbed inside the semiconductor. In this case, the energy of the photon can be transferred to an electron in the semiconductor valence band, which gains enough energy to be promoted into the conduction band leaving behind a positive charge (a hole): an electron hole pair is generated. The photogenerated carriers tend to recombine quickly unless they are separated either by thermal diffusion or by the action of an electric field (drift) of a p-n junction. When present, drift is always predominant above diffusion. For this reason, photons absorbed inside the depletion layer of the junction originate electron-hole pairs which are immediately separated by the strong electric field, while absorption near the edge of the space-charge region produces carriers with a finite probability to diffuse and reach the depletion layer. On the contrary, photons absorbed far from the space-charge region do not contribute to carrier generation because the electron-hole pairs recombine almost instantaneously. The illumination of a solar cell has then the effect to accumulate photo-generated carriers at the sides of the junctions establishing a certain voltage; when the device terminals are connected to a load, a current will flow. When the cell is not illuminated the only flowing current is the reverse saturation current J_0 which is due to minority carriers diffusion and recombination from the neutral regions into the depletion layer.

An ideal solar cell is equivalent to a diode, so one can use the Shockley equation to describe how current is affected by voltage under no illumination. Under illumination the curve is identical but shifted downwards, a feature called the "superimposition principle". Figure 1.6 reports typical J-V curves for a solar cell, and the J-V under illumination defines three important quantities: the short circuit current Jsc (identical to the illumination current J_L), the open circuit voltage Voc and the maximum power point Pmp = Vmp·Jmp.

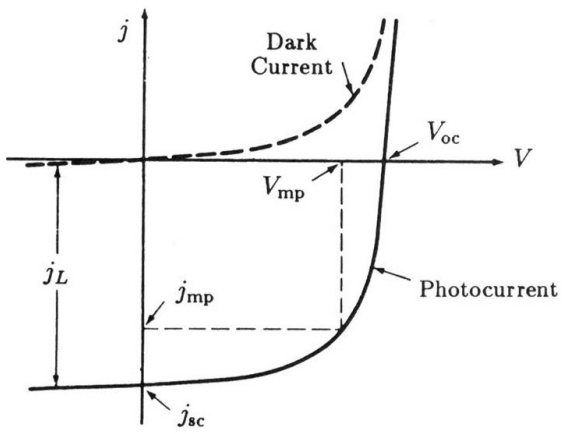

Figure 1.6: J-V curves of a solar cell in dark and under illumination.

From these values it is possible to define the so-called Fill Factor (FF):

$$FF = \frac{V_{mp} \cdot I_{mp}}{V_{oc} \cdot I_{sc}}$$

and the relevant cell efficiency η:

$$\eta = \frac{V_{mp} \cdot I_{mp}}{P} = \frac{V_{OC} \cdot I_{sc} \cdot FF}{P}$$

being P the total incident power on the solar cell.

A real cell can be modeled as an ideal current generator (in parallel with a diode) with two resistances, one in series called "series resistance" Rs and one in parallel called "shunt resistance" Rsh, as reported in figure 1.7.

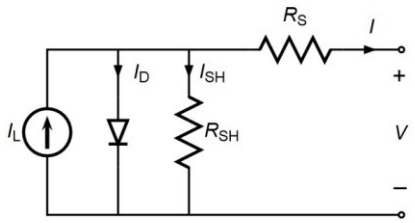

Figure 1.7: Equivalent circuit of a real solar cell.

In this case, the equation that describes the dependence of current from the various electrical parameters is the Shockley equation modified to account for the effects of Rs and Rsh:

$$J = J_L - J_0 \left(e^{\frac{q(V+JR_S)}{nK_BT}} - 1 \right) - \frac{V + JR_s}{R_{sh}}$$

Here, J, J_L and J_0 are respectively the current density, the current density under illumination and the dark saturation current density, T is the temperature, V is the voltage applied at the sides of the cell and *n* is the ideality factor. Note that this is an implicit equation in J which requires numerical procedures to be solved.

In a solar cell, the series resistance has three causes: the movement of carriers through the absorbing layer, the contact resistance between the electrical contact and the absorber, the resistance of the top and rear electrodes. Rs has a main impact on reducing the FF, but very high values of Rs can also influence Jsc. Rs has a very strong impact on the slope of the J-V curve near Voc but does not influence the value of Voc itself, since there is no current flowing through the cell at Voc. Finding the slope of the J-V curve near Voc is a useful procedure to estimate Rs. Clearly, a good solar cell must possess Rs as low as possible (below 1 $\Omega \cdot cm^2$).

The value of the shunt resistance is essentially related to the presence of defects inside the solar cells. In fact, defects create alternate paths for photogenerated carriers and thus have the detrimental effect to reduce the

external current and voltage generated by the device. Indeed, a high-quality solar cell has a very high value of Rsh, typically above 10^3 Ω·cm^2. The shunt resistance influences the slope of the J-V curve near Jsc, and finding that slope gives an estimation of the value of Rsh. To neglect the effects of the device's area, both Rs and Rsh are typically expressed as resistances per unit area.

Another important quantity is the sheet resistance R□. Using R□ is particularly useful because a squared sample with uniform thickness *t* has a resistance R = R□ regardless from its actual area. R□ is related to the film resistivity ρ according to the relation

$$\rho = R\square \cdot t$$

1.4 CIGS-based solar cells

1.4.1 CIGS material properties

$Cu(In_x,Ga_{1-x})Se_2$ is a solid state solution of Cu_2Se, In_2Se_3 and Ga_2Se_3 where In and Ga occupy the same site. The copper content and the Ga/In ratio define the material phase and electrical properties. CIGS possesses an incongruent melting point and thus is characterized by a complicated phase diagram, reported in figure 1.8(a), with many possible phases forming at different temperatures or copper concentration. Only the α phase is of interest for photovoltaic applications: α-CIGS grows in the chalcopyrite structure (figure 1.8(b)) with a p-type doping due to intrinsic defects (mostly copper vacancies). Given that all other phases are n-doped, it is mandatory to grow the α phase alone. This phase exists only for a copper concentration lower than 25%, and its formation is controlled by the Cu/[Ga+In] ratio: α phase forms only in a narrow region when this ratio ranges from 0.8 (22.2%-at Cu) to just below 1 (25%-at Cu), otherwise other phases are obtained.

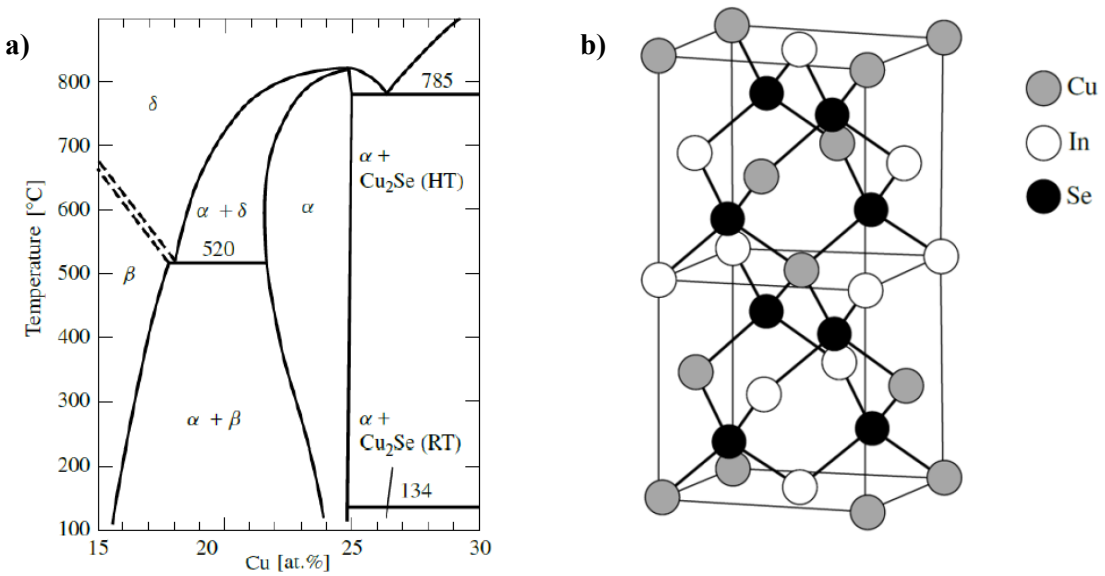

Figure 1.8: Pseudo-binary equilibrium phase diagram of In_2Se_3-Cu_2Se (a) and chalcopyrite structure (b).

The energy gap of CIGS is affected by the Ga/[Ga+In] value, called GGI: increasing the gallium content raises the conduction band while maintaining constant the valence band, resulting in a larger bandgap according to the relation [7]:

$$E_{gap}(x) = (1 - x) \cdot 1.01 + x \cdot 1.65 - b \cdot x \cdot (1 - x)$$

where x=GGI and b is a parameter called "bowing factor" usually ranging between 0.15 and 0.24 eV.

This formula allows for fine bandgap engineering in order to further increase the efficiency of a CIGS cell. In fact, increasing the GGI near the back contact has the effect of establishing an additional drift field for the minority carriers (electrons) which favors carrier collection and minimizes recombination at the back interface, maximizing Jsc. Furthermore, Voc can be increased by a higher GGI, and thus a higher bandgap near the space-charge region. This feature is called "gallium grading" or "bandgap grading" [8] and it is commonly employed in high-efficiency CIGS solar cells. The benefits induced by the gallium grading are particularly important when the absorber is very thin (below 1 μm).

α-CIGS films usually possess a free hole concentration in the order of $10^{15}cm^{-3}$-$10^{17}cm^{-3}$. This value may be changed by modifying the intrinsic composition or, more easily, by introducing and extrinsic doping. The most used dopant is sodium, which can increase the free hole density of around two orders of magnitude and, at the same time, has a positive impact on the CIGS itself: Na is expected to passivate grain boundaries by occupying the Cu vacancies and reducing the antisite defect density.

Another important property of CIGS is that it possesses the highest absorption coefficient *α(hv)* among all semiconductors. For photons with an energy of 0.2 eV higher than CIGS energy gap the absorption coefficient is $2 \cdot 10^{5}cm^{-1}$, two orders of magnitude greater than the silicon one. This allows CIGS to absorb all incident sunlight with a layer one hundredth thinner than Si. In fact, typical CIGS thickness is around 1-2 μm.

1.4.2 Conventional CIGS deposition techniques

The classic deposition techniques for large-area CIGS based solar cells are co-evaporation and sputtering. These two procedures possess some common features: the CIGS is deposited at high temperatures, between 450°C and 600°C, to favor the formation of the desired α-phase. Afterwards, a selenization process is applied to reintroduce the selenium which evaporated from the CIGS lattice, and this procedure makes use of the toxic gas H_2Se.

Thermal coevaporation

Thermal coevaporation is based on the concurrent evaporation of CIGS precursors from several heated sources. It is possible to modify the evaporation rates and/or the substrate temperature during the deposition.

A schematic representation of the typical experimental setup for CIGS coevaporation is reported in figure 1.9.

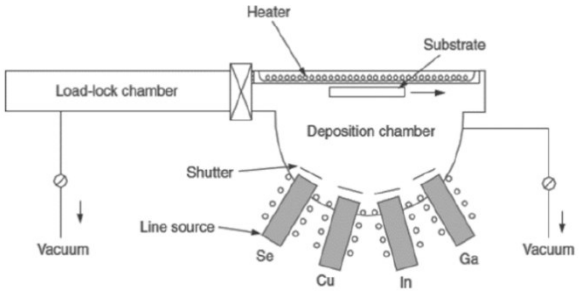

Figure 1.9: Schematic representation of CIGS deposition via coevaporation.

In some cases, the evaporation is realized using three precursors (Cu_2Se, Ga_2Se_3 and In_2Se_3) instead of the classic four elements Cu, In, Ga, Se. Nevertheless, it is mandatory to keep the substrate temperature above 400°C since there is no other alternative for growing the correct chalcopyrite phase for CIGS, and a successive selenization with H_2Se is sometimes performed to adjust the selenium concentration in the film. On the contrary, with this technique it is very easy to introduce the gallium grading by simply tuning the evaporation of indium and gallium during the CIGS deposition.

Sputtering

Sputtering is a widely used deposition technique by the semiconductor industry. Deposition by sputtering is realized by bombarding a solid target with high-energy particles. Those particles can be supplied in several ways such as by a plasma, a radioactive source emitting specific particles or an ion source. When an energetic particle strikes the target it transfers momentum to its atoms causing a collision cascade in the target itself. The cascade then recoils and returns to the target surface. In this case, if the energy of the cascade is higher than the target binding energy, an atom is emitted from the surface. The situation is depicted in figure 1.10.

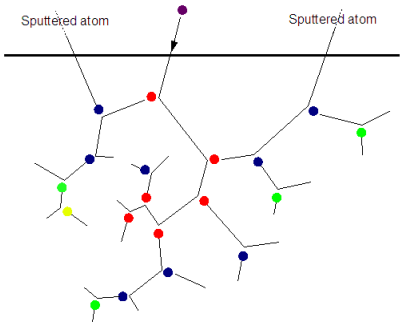

Figure 1.10: The sputtering process.

The average number of atoms emitted by the target for a single incident particle is defined as the "sputtering yield", and depends on various deposition parameters as well as on physical properties of the target. The typical experimental setup for depositing thin-film solar cell make use of an inert gas (argon) as source of bombarding particles, in order to avoid any chemical interaction with the target.

The energetic particles are always accelerated by an external electric field. Whether the external potential is continuous or alternate, the technique is named DC sputtering or RF sputtering. Usually, in DC sputtering the voltage is set above 3 kV, while in RF sputtering the frequency is of the order of MHz. Numerous possible variants of either DC sputtering or RF sputtering have been developed in the past years. Nowadays, sputtering is also used in analysis procedures, such as SIMS measurements (see 3.1.7), as the primary method for surface etching.

Sputtering of materials with high melting point can be performed provided only that a solid target is available, while evaporation in a resistance crucible may be difficult or impossible. Typically, sputtered films have a better adhesion to substrates than evaporated layers. A single target ensures a large number of depositions with no external maintenance, making this technique suitable for ultra-high vacuum applications. It is even possible to realize reactive sputtering by using a reactive gas (ex: oxygen) instead of the classic inert gas. Pulsed lased deposition can be considered as a variant of the sputtering process where the target is hit by light beam rather than by energetic particles. A fine layer-by-layer control can be achieved with such technique, while it is rather difficult with standard sputtering.

Sputtering can be used to deposit CIGS in a solar cell, but the general efficiency of such devices is lower than co-evaporated CIGS. The conventional growth procedure begins with the sequential deposition of precursor layers using targets with different compositions. Then, a high temperature annealing (above 500°C) is performed in an atmosphere of H_2Se or Se_2 to induce selenization in the stacked layers and form the correct phase of CIGS. A typical experimental setup for sputtering of CIGS is reported in figure 1.11.

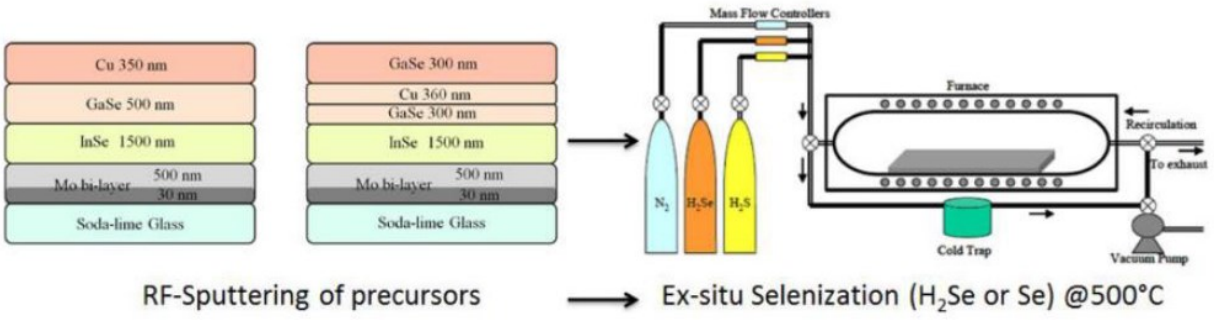

Figure 1.11: schematic representation of CIGS deposition via sputtering: stacking of precursor layers and successive selenization at high substrate temperature.

1.5 CIGS-based solar cells at IMEM-CNR

The typical structure of a CIGS-based thin film solar cell realized at IMEM-CNR in Parma is reported in figure 1.12.

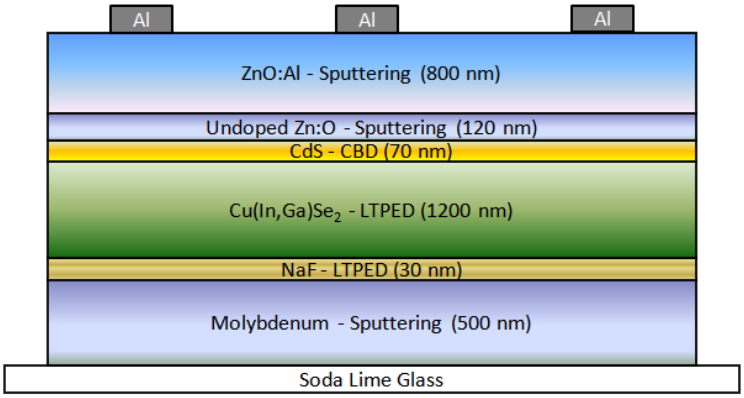

Figure 1.12: typical structure of CIGS-based solar cell realized at IMEM-CNR.

1.5.1 Substrate and back contact

The substrates were commercial 2mm-thick 2.5cm×2.5cm (6.25 cm_2) soda-lime glass, covered with Si_3N_4 and Mo, supplied by Singulus Technologies. Si_3N_4 had a thickness of 100 nm and acted as blocking layer to avoid sodium diffusion from the glass into the CIGS, thereby the sodium content was controlled by the NaF precursor layer only. Mo layer is 700nm-thick deposited by sputtering and was the back contact of the solar cells, with a sheet resistance of 35 μΩ□.

1.5.2 NaF

In all cells, CIGS is deposited via low temperature pulsed electron deposition LTPED (see 2.2). Though it may resemble the Pulsed Laser Deposition, this technique has the unique feature of allowing the deposition of the absorber at a substrate temperature of 250°C, much lower than the conventional deposition techniques, using a quaternary ceramic target with the desired composition. As the very low deposition temperature of LTPED does not allow the migration of sodium towards the CIGS/back interface, a thin layer of NaF is deposited via LTPED on the electrode prior to CIGS growth. NaF ceramic targets are produced at IMEM-CNR using the procedure described in 2.2.6. The thickness of the NaF layer is directly related to the amount of sodium incorporated in CIGS, and its exact thickness is calibrated regularly by shooting 5000 pulses on glass and measuring the resulting thickness with a profilometer. The calculated deposition rate is about 0.02nm/pulse, allowing for a controlled deposition of 8-10 nm of NaF. The deposition of NaF was found to be a good alternative to the standard deposition of $MoSe_2$ [9]: the presence of $MoSe_2$ interlayer is necessary as it reduces the band distortion and leads to quasi-ohmic contacts at the CIGS/Mo interface, which

otherwise would behave as a Schottky barrier. As reported in 4.3, the CIGS/NaF/back electrode shows ohmic-like behavior thanks to interface tunneling rather than reduction of Schottky barrier height, allowing the realization of solar cells with series resistance as low as 0.2 $\Omega \cdot cm^2$.

The effective sodium diffusion in LTPED-deposited CIGS is much lower than in materials deposited or annealed at temperatures above 500°C. Unfortunately, it is not possible to deposit a thicker layer of NaF, because past results have shown that adhesion of NaF to Mo is ensured only if the NaF thickness is below 30 nm. However, it was seen that sodium diffusion is still adequate in CIGS with a thickness up to 1.6 μm.

The adhesion of NaF to the underlying layer is a major concern in light of substituting Mo with a different material, such as a TCO. Indeed, NaF deposition and thickness were separately optimized for every alternative substrate employed in this thesis.

1.5.3 CIGS

As already mentioned, CIGS is grown by LTPED at a substrate temperature of 250°C. So far, high-quality solar cells [10] and CIGS single crystals [11] have been obtained using LTPED in a single-stage deposition without requiring any post deposition selenization at high temperatures. Targets for CIGS depositions are fabricated at IMEM-CNR using a modified liquid encapsulated Czochralski method.

For LTPED deposition of CIGS, the ablation mechanism became dominates over thermal evaporation for accelerating voltages of at least 11.5 kV [12]; previous deposition have shown that the best compromise between CIGS composition and surface morphology occurs with an electron accelerating voltage of 16 kV.

During depositions, the thickness of the layer is monitored in real time using a Raytek Marathon MM pyrometer. In fact, the radiation emitted at 8μm from the growing CIGS presents maxima and minima due to interference phenomena; after an initial calibration, this procedure allows to determine the exact thickness of the deposited film.

All CIGS samples undergo a post-deposition annealing at the same deposition temperature of 250°C for 80 minutes. This annealing is required both to enhance CIGS cristallinity and orientation and to diffuse the sodium across the CIGS layer. The low and constant annealing temperature is chosen in order to avoid any selenium re-evaporation from CIGS. As figure 1.13 reports, the duration of this post deposition annealing affects all photovoltaic parameters, probably due to the very slow sodium diffusion at T=250°C.

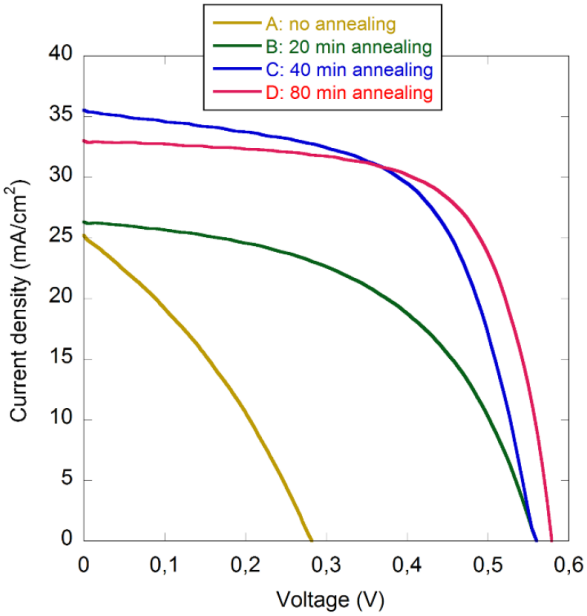

Figure 1.13: JV measurements of solar cells with different annealing time [13].

1.5.4 Buffer Layer

In all CIGS-based solar cells, the upper window layer is composed by a buffer layer and a TCO layer. This widow layer has the function to complete the p-n junction, to collect the photogenerated carriers and to maximize the light reaching the absorber. The presence of a buffer layer ensures good interfacial properties between CIGS and the upper TCO in terms of band structure and lattice matching while reducing recombination at this interface.

The buffer layer for CIGS based solar cells is cadmium sulfide (CdS) deposited via chemical bath deposition (CBD). The deposition is realized using an home-made experimental setup, making use of cadmium sulfate ($CdSO_4$) as cadmium precursor and thiourea ($CS(NH_2)_2$) as sulphur precursor. The standard deposition of CdS begins with the introduction of the CIGS sample in a glass beaker containing a solution of bi-distilled water and ammonia having a pH=12 at room temperature for 5 minutes. This treatment is required to "clean" the CIGS surface from contaminants and oxidation occurred during the unavoidable air exposure. Then, $CdSO_4$ is added, followed by thiourea after two minutes. Afterwards, the beaker is placed inside a hot bath at a temperature T=80°C to initiate the CBD deposition. The growth lasts 20 minutes with the solution magnetically stirred by a magnetic anchor. After 10 minutes the sample is temporarily removed from the chemical bath since it is necessary to renew the chemical solution to avoid the inclusion of big clusters of CdS which have nucleated inside the chemical bath. With this procedure it is possible to grow a 90-100 nm-thick film of CdS, the best compromise to obtain high-quality CIGS-based devices.

During the last year of the PhD, a research project on aiming at improving CdS deposition was initiated. Obtained results were very positive: the standard deposition process has been modified so that i) the growth

time was almost halved, ii) deposition is completed within a single step, iii) the deposited material is smoother and provides a better coverage of the CIGS interface and iv) the deposition temperature was lowered to 60°C. In practice, with the optimized process only 50 nm of CdS are required to form a good quality CdS/CIGS junction, which results in higher buffer layer transmittance and increases the total current generated by the cell. The optimization concerned the concentrations and the stochiometric ratios of the precursors, as indicated by table 1.1.

Process	$[Cd^{2+}]$	$[SC(NH_2)_2]$	Cd : $SC(NH_2)_2$	$[NH_4OH]$	T (°C)
Standard	1.77 mM	0.025 M	1 : 14.2	3 M	80
Optimized	3 mM	0.105 M	1 : 35	1.5 M	60

Table 1.1: Standard and optimized chemical parameters of CdS deposition via CBD.

1.5.5 Front electrode

The solar cell is completed by a layer of 100 nm of undoped ZnO (UZO) and a layer of AZO 800 nm-thick. The presence of UZO is required to drastically reduce shunts in the device, while AZO acts as the transparent electrical contact. Both AZO and UZO are deposited via RF-Magnetron sputtering using a cathode fabricated by Angstrom Science and commercial targets of ZnO:Al and ZnO. The optimal deposition parameters were studied elsewhere [13] and are summarized in table 1.2.

Material	Distance (cm)	Power (W) / Power density (W/cm^2)	Pressure (mbar)	Deposition Temperature	Deposition Rate (nm/min)
UZO	8	100 / ~5	5·10-3	RT	15.4
AZO	8	120 / ~6	5·10-3	RT	32.0

Table 1.2: Sputtering parameters of AZO and UZO deposition.

Note that no antireflection coating is present in the standard structure. An antireflection coating is a specific layer whose function is to reflect the photons coming from inside the solar cell back towards the absorber.

1.5.6. Aluminum contacts

Front metal contacts are required to reduce the series resistance of the solar cell and to increase the fill factor; their contribution is very important in devices with large area such as PV modules. The zones covered by the metallic contact does not contribute to the PV power generation, therefore simulations are usually conducted to identify which geometry ensures the best compromise between shading and electrical improvements.

At IMEM-CNR, the architecture of the cell is completed with the evaporation of aluminum electrical contacts above the AZO layer, and takes place in a vacuum chamber with vacuum higher than $5 \cdot 10^{-6}$ mbar to avoid contaminations. The sample is placed at about 10 cm above a Ta crucible containing 5N aluminum rods with a mass of about 0.3 g. The result is the deposition of about 2000 nm of aluminum electrical contacts. The effective shape of these contacts is obtained using specific metallic masks with different geometries placed in contact of the sample.

The same geometry was used for the evaporation of the metallic grids introduced in 4.5, which however took place in a different chamber using a specifically designed mask.

Chapter 2: Deposition of Transparent Conductive Oxides using Pulsed Electron Deposition

This chapter describes the growth of TCOs using the PED technique.

The first section contains an introduction on the materials studied in this doctoral thesis. The focus is primarily on physical properties, state-of-the-art deposition techniques and open problems affecting each material in light of potential applications in BIPV. Afterwards, the PED process is introduced with a detailed discussion on electron pulse generation, propagation and interaction with target. Two dedicated sections illustrate target preparation and experimental setup of deposition chamber installed at IMEM-CNR. The last section describes the experimental details for each TCO grown at IMEM - CNR using PED technique.

2.1 Description of studied oxides

2.1.1 $CuGaO_2$: an innovative p-type TCO.

P-type transparent conductive oxides (p-type TCO) are a class of materials being discovered and actively studied only in recent times [1] [2]. The interest in p-type TCO research and optimization has rapidly increased [16] due to their potential applications in various topics like transparent electronics, organic solar cells and UV-emitting diodes. Indeed, in 2000 the first (UV)-emitting diode based on a p-n heterojunction composed of p-SCO and n-ZnO was realized [17], followed shortly by other examples of transparent diodes and different UV-emitting diodes [18] [19] together with innovative applications in organic solar cells [20]. A good p-type TCO would also be suitable to form an ohmic contact when coupled to intrinsically p-type semiconductors like CIGS or CdTe.

The origin of the p-type conductivity can be summarized as follows. A typical wide band gap oxide has the valence band edge of oxides strongly localized on oxygen ions, which act as deep traps for holes introduced in the valence band. So, holes cannot move within the crystal lattice even under the influence of an external electric field. It is possible to solve this problem by introducing cations with closed shell levels possessing an energy comparable with the one of *2p* states of oxygen; in this situation, the top of the valence band consists of cation *d* orbitals and oxygen *2p* states. The typical electronic configuration is sketched in figure 2.1.

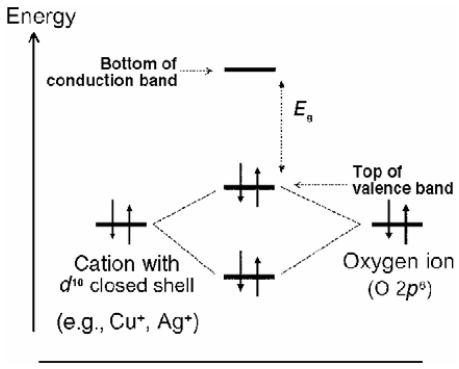

Figure 2.1: Schematic of the chemical bond between an oxide ion and a cation that has a closed-shell electronic configuration with an electron energy assumed equivalent to that of oxygen 2p electrons [21]

The anti-bonding levels now acts as the new valence band edge due to the closed shell configuration of both cation and anion, and this process also reduces the localization of the band edge and the effective mass of carriers. Cu and Ag have the desired d_{10} states for this purpose. In particular, in Cu_2O eight electrons on an oxide ion are distributed among four bonds with four different coordination cations (the structure has a tetrahedral coordination) creating an electronic configuration that increases holes delocalization at the valence band edge. Cu_2O was in fact the first p-type TCO that was discovered and studied. Unfortunately, its energy gap (2.17 eV) [22] and hole mobility are relatively small.

Delafossite Cu-based oxides were later proposed [23] to increase the electrical and optical properties of Cu_2O; the delafossite structure is depicted in figure 2.2. Indeed, two main advantages arise with the introduction of a counter cation with filled *d* orbital whose energy is comparable to the one of 2p orbital of oxygen in Cu_2O:

- holes are less localized due to a reduced Coulomb force induced by oxygen atoms;
- there is a minor probability of d-d transition that could absorb visible light;

Successive investigations revealed that Cu-based TCOs with delafossite structure and chemical formula $CuMO_2$ (M=Al, Ga, Fe, In, Cr, B, Sc, Y) display higher bandgap and hole mobility if compared to other binary p-type TCOs like NiO or TiO [24].

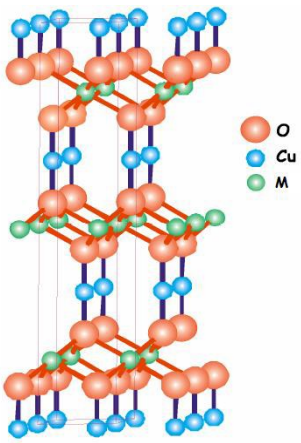

Figure 2.2: Crystal structure of delafossite. The layers of Cu cations and MO_2 are stacked alternately, perpendicular to the c-axis. Different colors refer to different elements as indicated by the legend.

Among many elements used to dope copper oxide, only some of them (Ga, Al, In, Cr, B) achieved moderate or good results. Table 2.1 summarizes the optical and electrical properties of best delafossite copper oxides.

Material	Energy gap (eV)	Resistivity (Ω·cm)	Average Transmittance (%)
$CuGaO_2$	3.6	$6.3 \cdot 10^{-2}$	80
$CuAlO_2$	3.5	0.22	70
$CuInO_2$	3.6	> 1	70
$CuCrO_2$	3.1	1	40

Table 2.1: Comparison of optical and electrical properties of delafossite Copper oxides. Data are taken from [16] and [24].

Among various materials, $CuGaO_2$ displays the best results both for resistivity and optical transmittance, and for this reason it was chosen as the novel material to be studied in this doctoral work.

There are only few literature works reporting an electrical characterization of $CuGaO_2$ samples. The parameters reported in table 1 are obtained on a crystalline epitaxially-grown structure deposited on sapphire [25], while polycrystalline $CuGaO_2$ possesses a resistivity which is typically 10-20% higher.
Lattice constants of the delafossite structure of $CuGaO_2$ are a = 2.98 Å and c = 17.11 Å [26] which are in agreement with theoretical simulations, which also predict a band profile with an almost flat valence band (figure 2.3). This is the cause of the high effective-mass of holes in valence band which leads to a very low hole mobility, around 0.23 $cm^2/V \cdot s$ for this material.

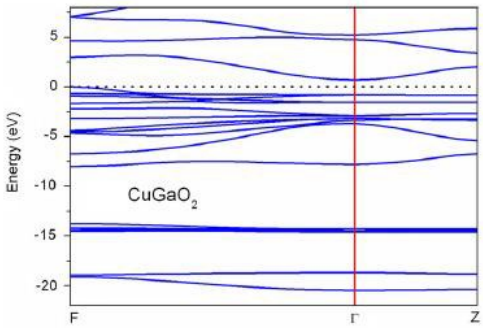

Figure 2.3: Calculated band structure of delafossite $CuGaO_2$ [26]

Electrical conductivity can be increased up to two orders of magnitude when doping $CuGaO_2$ with Fe 0.5%wt [27], which acts as substitutional for Gallium. Despite this enhancement, the conductivity remains many orders of magnitude lower than standard n-type TCOs, see for example [28], and the situation is also

similar for the other delafossite p-type TCOs. This is a major problem affecting this class of materials (and p-type TCO in general) which is yet to be solved.

Although there is no evidence in literature of a phase diagram for the Ga-Cu-O system, some information can still be obtained from the analysis of the similar Cu-Fe-O system [29] [30] and from stability studies of the Cu-Ga-O system [31] [32]. As indicated by figure 2.4, $CuGaO_2$ in delafossite phase is stable only at a very high temperature (above 1000°C for an oxygen pressure of 10^{-2} mbar) when grown oh sapphire; at lower temperatures, the material tends to crystallize in its spinel phase with chemical formula $CuGa_2O_4$.

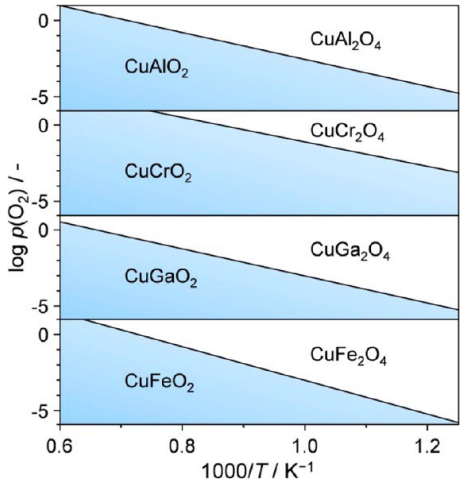

Figure 2.4: Diagrams showing the thermodynamic stability of the delafossite and spinel phases at different temperatures and partial O2 pressure [31]

The necessity of a deposition temperature so high is makes deposition of $CuGaO_2$ quite difficult. Almost all growths of $CuGaO_2$ reported in literature rely on a long high-temperature post deposition annealing; the parameters of the process are rather differently among various sources [33] [34], and analogous indications are valid also for deposition of the similar compound $CuAlO_2$ [35] [36] [37]; only a single work reports $CuGaO_2$ growth without any post- deposition treatment. It is quite clear that there is no evidence of a standard and low-cost procedure to deposit $CuGaO_2$. The majority of samples are realized either by Pulsed Laser Deposition (PLD) or by Sputtering always on sapphire substrates. In this context, PED could potentially improve the growth of $CuGaO_2$: the high energy transmitted to particles inside the plume may be sufficient to induce crystallization in the correct phase even when depositing on low cost substrates like soda lime glass, thus eliminating the necessity of the high-temperature post deposition annealing and costly substrates and opening the way to novel application of this TCO.

2.1.2 Conventional n-type TCOs

Conventional and widely-used n-type TCO are studied since the half of 1900, therefore their optical, electrical and structural properties are well known and optimized [28]. The most used material is Indium Tin

Oxide (ITO), which is now gradually replaced by indium free alternatives like Fluorine Tin Oxide (FTO) or various Zinc Oxides, the most common being Aluminum Zinc Oxide (AZO). This section briefly describes important properties of ITO, FTO and AZO in light of their application as materials for thin-film solar cells and transparent electronics in general.

Indium Tin Oxide

Indium Tin Oxide (ITO) is a ternary compound made of Indium, Tin and Oxygen in various proportions. The typical composition is In_2O_3 doped with 10% wt Tin. This material features excellent optical and electrical properties: it is a high-doped n-type semiconductor with a typical resistivity around 10^{-4} Ω·cm and a transmittance above 80% in the visible region [38] [39]; it possesses a direct band-gap with an energy varying from 3.5 eV to 4.3 eV depending on the effective dopant concentration [40]. Differently to other n-type TCO, this material is almost unaffected by moisture [41], a very useful feature for photovoltaic applications.

ITO is the standard TCO used in many different industrial applications. ITO thin films are employed as transparent conductive coatings in transparent electronics (liquid crystal displays, touch panels, flat panels display, etc.), in organic LEDs and in both conventional and thin-film based solar cells. Airplane glasses are usually covered with a thin layer of ITO to enable a transparent defrosting mechanism. Other examples of usages of these materials are gas sensors, strain gauges for hazardous environment, optical coating and antistatic coating. ITO is primarily deposited on glass using different techniques, the most common being chemical vapor deposition (CVD) [42] and sputtering [43].

The main concern regarding mass-production of ITO is the cost: the price of Indium, a rare material, tends to fluctuate quite rapidly and unpredictably due to market demand [44]. Therefore, research is heavily focused on replacing this material with Indium-free and low cost TCOs. This problem is so important that even numerous European projects [45] [46], funded by the European Union under the Horizon 2020 program, are currently undergoing to find cost-effective and high quality replacements to ITO. To date, the most promising alternatives for Indium Tin Oxide are Fluorine-doped Tin Oxide or Aluminum-doped Zinc Oxide.

Fluorine-doped Tin Oxide

Fluorine-doped Tin Oxide (FTO) is an n-doped ternary compound made of SnO_2 doped with SnF_2 in variable proportions. It possesses electrical and optical properties only inferior to those of ITO: good FTO films displays a typical resistivity around $5 \cdot 10^{-4}$ Ω·cm, an optical transparency above 85% [47] and a direct bandgap above 4 eV [48]. Deposition of high quality layers is usually realized via chemical vapor techniques (CVD or spray pyrolysis) or via sputtering. Unfortunately, each of these techniques requires working with toxic precursors containing fluorine like CF_4, posing a major concern affecting FTO deposition. Research is indeed focused on developing valid non-toxic alternative materials, with best candidate being Aluminum-doped Zinc Oxide.

Zinc Oxides

Zinc Oxide is an inorganic compound with the chemical formula ZnO, natively n-doped due to oxygen vacancies or Zinc interstitials [49]. Carrier concentration in ZnO can be easily controlled by adding specific group-III elements (Al, Ga, In) which acts as substitutionals for Zinc. In fact, the majority of ZnO is in the form of Aluminum Zinc Oxide (AZO), a cheap and non-toxic TCO with an Aluminum concentration usually between 1% and 5% wt.

High quality AZO thin films display a resistance as low as $4 \cdot 10^{-4}$ Ω·cm and a transmittance above 80% in the visible region [50] with a direct energy gap around 3.5 eV [51]; transmittance can be enhanced even above 90% optimizing deposition, thickness and dopant concentration.

The typical deposition method is sputtering, but other techniques like chemical vapor deposition [52], sol-gel process [53] or pulsed laser deposition [54] are reported in literature.

Alternatively, doping Zinc Oxide with Gallium or Indium results in compounds (respectively GAZO and INZO) with similar electrical and optical properties, as reported by [55] and [56], provided that Indium concentration in INZO is very high. The mixed Indium-Gallium Zinc Oxide is a material used in a particular class of transistors.

While AZO is the best cheap and non-toxic candidate to replace ITO in transparent electronics, it is also useful to study both GAZO and INZO as possible TCO candidates in solar cell applications like BFSC.

2.2 The Pulsed Electron Deposition Technique

2.2.1 PED main features

Pulsed electron deposition (PED) is a physical vapor deposition technique (PVD) capable to grow high-quality thin films using a single target at low substrate temperature. The process relies on the ablation of a ceramic target by pulsed electron beams carrying a huge power density (up to 10^8 W/cm^2) delivered in a very short amount of time (in the order of 100 ns). This power density is at least two orders of magnitude higher than the one required evaporating materials (around 10^6 W/cm^2), so electron bombardment results in a non-equilibrium heating of the target's surface. For this reason, the target material is transformed into plasma with no phase transition: a congruent evaporation is possible even for compounds with incongruent melting point. This phenomenon is indeed the "ablation" mentioned above.

Ablation allows the target surface to be converted into plasma independently of its thermodynamic properties, therefore the target stoichiometry is transferred to the plasma and then to the thin film. Moreover, since the plasma has a very high temperature (thousands of K), plasma species are extremely energetic. This big energy is then transferred to adatoms in the growing film giving them a considerable surface mobility. As a consequence, it is possible to deposit samples with good cristallinity even at very low substrate temperature.

These two main features make PED suitable to deposit ternary or quaternary materials with a complicated phase diagram: the correct phase can be grown using a single target with desired stoichiometry and at a low temperature. Literature reports several examples of materials deposited via PED: Zinc Oxide-based semiconductors [57] and other oxides [58], hydroxyapatite [59], FeS_2 [60], high temperature superconductors like $YBa_2Cu_3O_7$ [61]. In the last few years, thin-film group at IMEM-CNR institute in Parma developed a low-temperature PED process (LTPED) to grow CIGS in thin film solar cells at a substrate temperature of 250°C, much lower than the conventional temperature required for CIGS deposition using sputtering or co-evaporation. Details of CIGS deposition via LTPED are found in 1.5.3.

2.2.2 Electron beam generation and propagation

Figure 2.5 [62] reports a schematic representation of the PED source used by the thin-film group at IMEM-CNR institute.

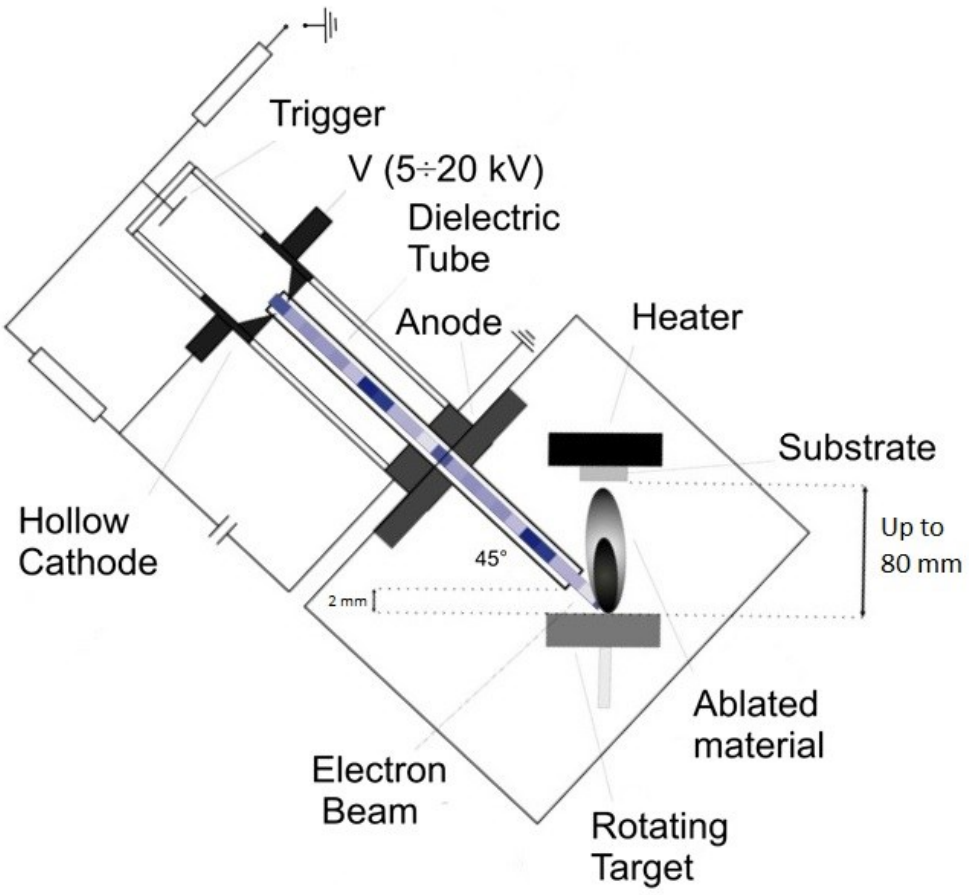

Figure 2.5: Schematic representation of a PED source [62].

Electron pulses are generated in a hollow cathode working in pulsed mode, whose special geometry allows the generation of high currents: the cathode itself is formed by a metal tube with a small exit facing a planar

anode, and this particular geometry increases the probability of background gas ionization generating high amounts of electrons in a single discharge. The electric charge of the cathode is provided by a specific capacitor connected in series to the cathode. The plasma discharged is ignited by a specific trigger circuit whose frequency can be modified by the user.

Electrons are then accelerated by a user-controllable high voltage (usually above 10 kV) and travels inside a dielectric tube towards the target. The tube is made of alumina, and its entrance tube is placed at the exact center of the hollow cathode. Electron collimation is favored by the tube's small diameter and by the magnetic field of the electron discharge [63]. In a typical experimental setup the alumina tube forms a 45° angle with respect to the target's surface and the substrate is placed directly above it. A background low pressure of inert gas is required for ionization and consequent beam propagation, and the resulting electron beam is composed by electrons with different kinetic energy. The discharge process usually takes no more than 100 ns.

The electron energy distribution inside a pulse is crucial for the ablation process. There are at least three different contributions as a function of electron energy in a single beam [63], as reported in figure 2.6:

- An initial small number of electrons with the highest energy, they may travel too deep in the target causing ablation to happen far below the surface;
- A second moderate group of particles with intermediate energy;
- A final pack of electrons with the highest current but the lowest energy, which only induce target heating and incongruent evaporation instead of ablation.

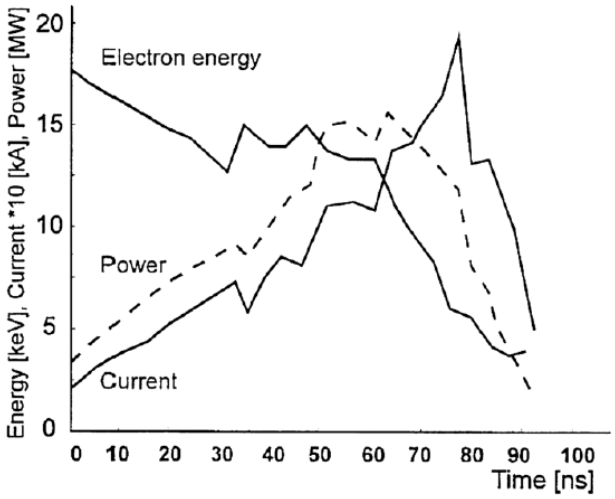

Figure 2.6: Electron energy, current and power of a single electron-beam pulse accelerated by 20 kV tension [63].

The energy distribution also depends on the cathode's temperature. An overheated cathode emits electrons, by thermo-ionic effect, with a generally low energy, thus extending the discharge tail and resulting in an increased incongruent evaporation. Commercial Neocera PEBS20 source ensures the cathode cooling by

limiting the pulse repetition rate in function of the accelerating voltage, so reducing the overall operating power. An example is given in figure 7, where the maximum operating power of the gun is set at 15W. One can see that the pulse repetition rate is maximum (10Hz) for voltages up to 14kV, and then decreases down to 5 Hz at 20 kV.

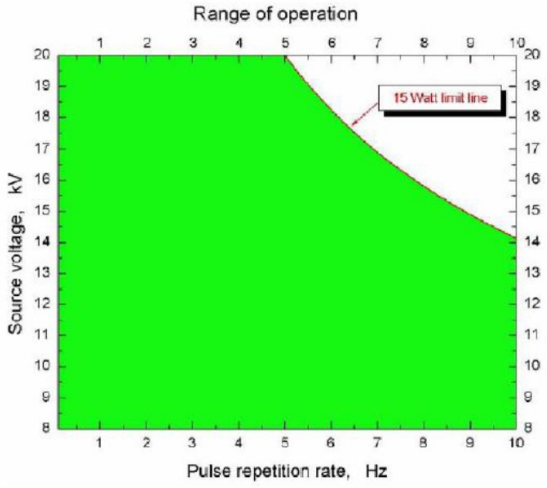

Figure 2.7: Maximum PED voltage of a Neocera PEBS20 source as a function of pulse frequency to keep the power limited at 15W.

The extremely high power of every pulse is compensated by its very short discharge time, so the effective power consumption of a PED source, that is its operating power, is very low; as an example, the gun of figure 2.7 uses no more that 15 W.

2.2.3 Interaction between electron beam and target

As discussed in the previous paragraph, electrons with different energies have different interaction with target material.

To have ablation, high-energy electrons must possess an energy higher than a certain value called “ablation threshold” which depends on the target material (around 10^7 W/cm^2); electrons with lower energies only causes incongruent evaporation.

On the other hand, if the ablation takes place too deep in the target a phenomenon called “hydrodynamic ablation” can occur: the material is converted into plasma below the target surface and the consequent expansion breaks the solid material above it sending target fragments towards the substrate. These solid debris create local variations of thickness and cristallinity in the growing film resulting in detrimental effects. The PED voltage is the crucial parameter to optimize to find the best compromise between these two phenomena when growing good-quality films.

In addition, the penetration range of an electron in the target is (in first approximation) linearly dependent on the energy of that electron inside the beam, as described in [64]. This energy is converted into mechanical, thermal and chemical form. Simulations [65] indicate that only a relatively small fraction of the initial energy is used to ablate the target, and the majority is transferred to the ablated particles as excited states or kinetic energy. This inner energy allows depositing thin films without the need for a high substrate temperature.

Furthermore, simulations indicate that immediately after an electron pulse the target surface reaches up to 7000-10000 K. Then, in few nanoseconds, the temperature drastically drops to 1000-2000K and finally the target thermalizes in a range of milliseconds. Provided that the target has a low enough thermal conductivity, ablation occurs even for materials with high melting point, while incongruent evaporation takes place during the cooling period.

In general, there are four main ablation mechanisms:

- Collisional ablation: a massive particle strikes a target and transfers momentum to its particles, allowing their ejection. This is the dominant process in sputtering deposition and has a lower yield compared to other ablation processes.
- Thermal ablation: energy is transferred to target by coupling with electronic and vibrational modes of the target material.
- Electronic ablation: energy is transmitted to target by an interaction between its atoms' electron shells and the electron beam. It is the dominant process in PED.
- Macroscopic ablation: a drawback of all deposition technique using high-energy beams, it originates large solid particulate which deposits onto the substrate. The target can either exfoliate or suffer hydrodynamic ablation, where the material evaporates below the surface ejecting liquid or solid particulate towards the substrate. This particulate either possesses an irregular shape or a droplet-like form.

The main mechanism of PED is electronic ablation. It originates a dense region of plasma containing many high-energy and ionized particles (ions, excited atoms, free electrons, etc.) expanding perpendicularly to the target surface; it is often called "plasma plume" for its resemblance to a feather, as one can see from figure 2.8.

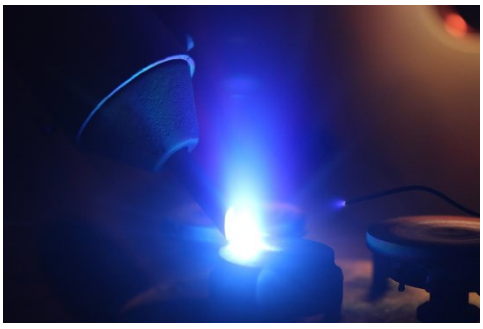

Figure 2.8: - Plasma plume formed by PED ablation of a CIGS target. The electron gun is on the left and its alumina tube drives the electron beam to hit the target surface with an angle of 45°.

Optical emission spectroscopy measurements can identify which excited species are travelling in the plume by analyzing the light emitted from the plume itself. The angular spread of the plume is smaller than the one of a classic thermal evaporation because particles inside the plume undertake a large number of collisions which reduces their angular divergence. The best plume shape is formed when the alumina tube forms a 45° angle with the target surface. This shape is also influenced by the background gas: higher gas pressures tend to form smaller plumes. Experimental observations indicate that the gas pressure has a very little influence on the plasma characteristics only in the range between 10^{-4} and 10^{-2} mbar. A typical deposition uses noble gases (Ar or He) as background gases because they do not interact with plume components. However, it is also possible to form new molecules in the plume itself by using a reactive gas like Oxygen. This is a very useful feature when depositing transparent oxides via PED. Figure 2.9 reports an example of plasma plume expanding in space and in time [58].

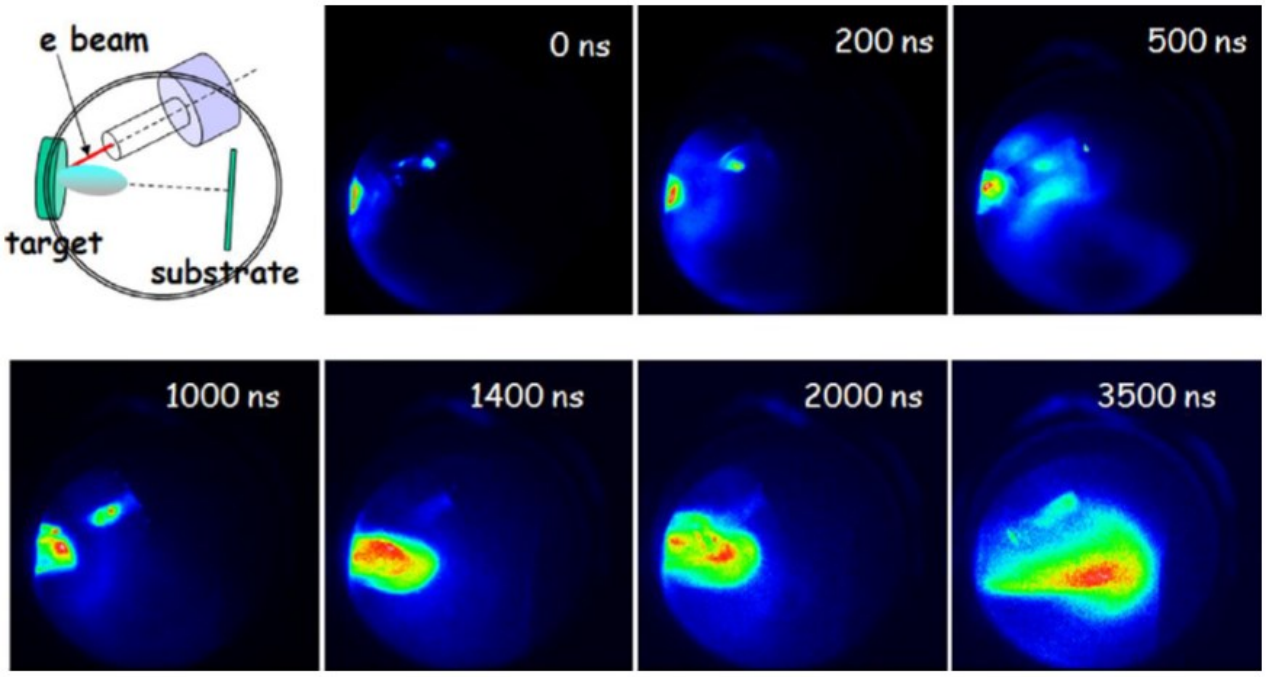

Figure 2.9: Plasma plume expansion in Ar background gas after PED ablation, at several different times.

The other main phenomenon always present during a PED growth is macroscopic ablation, which can only be minimized by optimizing the electron acceleration voltage. This process forms round particles (usually called droplets) with sizes varying from few nanometers to few micrometers. Dimension and density of these droplets depend on the target preparation: dense targets with no cracks or voids avoid the formation of large particles. Remarkably, droplets with a diameter of tens of nanometers play an important role during film deposition. While in the plume, they maintain the target composition because only a small fraction of volatile elements is able to evaporate from their surface. This helps maintaining a good deposition rate with negligible composition variation.

2.2.4 Thin film deposition

The most important parameters of thin-film growth are the film composition and the deposition rate, and in case of PED they depend both on the accelerating voltage and on the distance from the center of the deposition.

Films deposited via PED have an angular profile of the thickness directly related to the plume angular profile: the highest thickness is found on the axis of the plasma plume. The thickness angular distribution depends on both ablation and evaporation (opportunely averaged). Literature reports a model [66] describing these two contributions using a two-cosine function.

In order to grow a high-quality thin film, species arriving on the substrate must possess a certain "surface mobility" which is related to the adatom diffusion length D. D can be expressed as

$$D = D_0 e^{-\frac{\epsilon_D}{kT}}$$

where T is the substrate temperature and $\epsilon_D$is the diffusion activation energy which is usually in the order of 2-3 eV. A sufficiently high adatom diffusion is fundamental to grow good crystalline thin films.

Particles produced by ablation reach the substrate with an energy ranging from 1-2 eV up to 10 eV. This energy is higher than $\epsilon_D$and diffusion process is activated without the need for substrate heating. On the contrary, species produced by conventional deposition techniques working at thermodynamic equilibrium have an inner energy up to 1 eV and thus diffusion is activated only by external energy provided by a heated substrate.

2.2.5 Experimental setup

This section briefly describes the experimental setup of the deposition chamber used to deposit TCOs at IMEM-CNR institute in Parma.

All depositions were made using a commercial Neocera PEBS-20 electron gun. This PED source works with an electron accelerating voltage between 8 kV and 20 kV and with a trigger frequency between 1 Hz and 10 Hz; repetition rate is automatically reduced for high voltages in order to ensure cathode cooling. The dielectric tube used to guide the electrons is an alumina tube with an inner diameter of 3mm. The electron gun is mounted in the deposition chamber so that the dielectric tube forms a 45° with the target surface, and the substrate is placed directly above the target following the standard configuration discussed in 3.2.3 and 3.2.4. Thanks to three external screws, it is possible to slightly modify the PED source position to precisely adjust the gun position without opening the deposition chamber. The latter was kept at a base pressure lower than $5 \cdot 10^{-6}$ mbar by a turbomolecular pump coupled to a rotative pump. The chamber is also equipped with an openable porthole allowing samples introduction and with a manual shutter to better control deposition start and end. The exterior of the deposition chamber is shown in figure 2.10.

Figure 2.10: Deposition chamber installed at IMEM - CNR. The electron gun is mounted on the upper left corner.

The sample holder is specifically designed to house 25mm x 75mm substrates which are placed in contact with a graphite susceptor. Heating is provided by an infrared lamp placed inside this susceptor, and no significant temperature variations were observed along the holder axis. Two chrome-alumel thermocouples monitor the substrate temperature, and they must be manually placed in contact with the substrate itself before each deposition; a correct temperature measurement requires the thermocouples to be positioned perpendicularly to the substrate. This configuration allows reaching a maximum substrate temperature of 450°C.

Sample holder is placed above the target at a variable distance (usually greater than 6 cm) and it is centered above the point in which the electron beam hits the target. A high substrate-to-target distance leads to the deposition of films with a more uniform thickness but with a very low growth rate, while a low distance results in fast depositions with a small uniform area. A good compromise is usually found between 6 cm and 8 cm, depending from the target characteristics.

The target of the PED process is glued to a copper holder using silver conductive paste and placed about 1 mm below the alumina tube tip. The target can be put in rotation by switching on an external motor with user-controllable rotation speed. Rotation ensures a homogeneous target erosion and reduces the heating.

The gas flow is controlled by a manual gauge and measured by a full range vacuum sensor.

The typical substrate for TCO deposition is a low cost 25mm x 75mm Soda Lime Glass (SLG) slide. Other available substrates are 25mm x 75mm quartz slides or 5cm-diameters sapphire disks. The latter have to be manually cut into smaller pieces to be mounted on the substrate holder. Every substrate is cleaned prior to deposition in an ultrasonic bath using in succession acetone, ethanol and isopropyl alcohol (3 minutes each treatment), then it is dried with compressed air and placed on a hot plate at 100°C for 5 minutes.

To summarize, the user-controllable deposition parameters are:

- PED: accelerating voltage, trigger frequency, number of pulses
- Substrate: type, temperature, distance to target
- Gas: type, pressure
- Target: chemical composition

2.2.6 Target preparation

All the targets used in PED depositions were realized at the IMEM-CNR institute following the procedure described below.

1) Raw materials in form of ultrapure powder are weighted and mixed together in a ceramic crucible for at least 2 minutes
2) Mixed powder is encapsulated between two metallic discs inside a metallic cylinder with a diameter of 40 mm.
3) The cylinder is placed under a hydraulic press and subjected to a pressure of at least 200 bar for a minimum time of 5 minutes.
4) The compressed powders are synthered in air for 24h at a temperature higher than 1000°C (effective temperature depends on the composition).
5) The resulting target is a ceramic tablet with a diameter of 40mm and a height of 2-3 mm.

The tablets were preserved in a low-humidity environment before their use. They were glued to the copper holder using silver conductive paste dried by heating at a temperature higher than 200°C for a minimum time of 30 minutes.

2.3 Depositions of TCO

Literature on deposition of oxides via PED is very scarce. No data is available on the deposition via PED of delafossite p-type $CuGaO_2$ and there are only few sources reporting growth of conventional oxides [57] [58] [67], so there is no reliable information on the way deposition parameters affect sample characteristics. Therefore, for each studied material a thorough investigation was conducted to precisely determine the influence of all growth parameters on film properties. Films characterization is reported in chapter 4.

2.3.1 Gallium-doped copper oxide - $CuGaO_2$

Every deposition of $CuGaO_2$ was realized at a substrate-to-target distance of 6 cm. As previous growth tends to damage the target's surface, it was necessary to polish the target before each deposition to ensure that a good quality surface is exposed to electron beams. Literature on deposition of other p-type TCOs [68] [69] suggests that oxygen is necessary to favor the formation of the correct phase, so every growth of $CuGaO_2$ was performed in an O_2 atmosphere. If not specifically indicated, the substrate used for the deposition was low cost Soda Lime Glass (SLG).

The first three series of films were realized to study how every single deposition parameter (PED accelerating voltage, oxygen pressure and substrate temperature) influences device properties. Each series of

samples was therefore realized modifying a single growth parameter between each deposition with the following experimental setups:

1. PED accelerating voltage was varied between 14 kV and 20 kV at steps of 2 kV; these samples were deposited at Room Temperature (RT) using an Oxygen pressure of $1 \cdot 10^{-2}$ mbar;
2. Oxygen pressure was set between $6 \cdot 10^{-3}$ mbar and $1 \cdot 10^{-2}$ mbar at intervals of $1 \cdot 10^{-3}$ mbar, and also a single growth at $2 \cdot 10^{-2}$ mbar was performed; these growth were performed with a PED accelerating voltage of 16 kV at RT.
3. Substrate temperature ranged between 300°C and 450°C at steps of 50°C; these films were deposited at an oxygen pressure of $1 \cdot 10^{-2}$ mbar accelerating the electrons with 16 kV.

The composition of the first samples was always copper-deficient, as discussed in 3.2.1, so depositions from non-stoichiometric targets were performed. Two series of samples were therefore realized using a target with relative composition of 75% Cu and 25% Ga. All growths were realized with a PED accelerating voltage of 16 kV, either varying the oxygen pressure or the substrate temperature, with these experimental settings:

1. Oxygen pressure varied between $6 \cdot 10^{-3}$ mbar and $2 \cdot 10^{-2}$ mbar, depositing at RT.
2. Substrate temperature was set between 250°C and 450°C with an oxygen pressure of $1 \cdot 10^{-2}$ mbar.

As-deposited samples did not show a crystalline structure, so it was decided to perform a high-temperature post-deposition annealing. To this extent, it was necessary to substitute SLG with quartz or sapphire in order to reach the higher annealing temperature needed for crystallizing the film in the correct phase, as suggested by literature [37]. So, two final series of samples were deposited using either quartz or sapphire substrates.

A limited number of films were grown on quartz at 400°C at different oxygen pressures from $6 \cdot 10^{-3}$ mbar to $1 \cdot 10^{-2}$ mbar keeping constant the electron accelerating voltage at 20 kV and using both the stoichiometric and the non-stoichiometric target. Samples were then annealed at temperatures above 1000°C for a duration of 4h to 12h.

Numerous depositions were performed on sapphire substrates with the same experimental setup: PED voltage = 20 kV, oxygen pressure = $1 \cdot 10^{-2}$ mbar, substrate temperature = 400°C. Growths were realized using both the stoichiometric and the non-stoichiometric target. These samples underwent different high temperature annealing processes with a temperature of either 1000°C or 1200°C and a variable time ranging between 4 hours to 12 hours in order to study how post-deposition annealing influences film structure. All annealing treatments were performed in air.

By analyzing the results discussed in 3.2.1 it was possible to identify optimal growth conditions to deposit $CuGaO_2$ with our commercial PED source, which are summarized in table 2.2.

PED accelerating voltage	16 kV
Background gas type	Oxygen
Background gas pressure	10^{-2} mbar
Substrate type	Polished sapphire
Substrate-to-target distance	6 cm
Substrate temperature	At least 400°C
Post deposition annealing	4 hour in air at T = 1000°C

Table 2.2: Best growth conditions for $CuGaO_2$ deposition via PED.

2.3.2 Conventional TCOs

Indium Tin Oxide

All growths of ITO via PED were realized on Soda Lime Glass substrates using In_2O_3:SnO_2 (90/10 wt). targets which were polished every three depositions. Preliminary analysis showed that PED accelerating voltage does not have significant effects on film properties, and therefore it was set to 15 kV for every deposition. This value was chosen because it maintains the maximum trigger frequency (10 Hz) resulting in minimum deposition time. Moreover, it was found that background gas pressure only influences deposition rate; it was set at $8 \cdot 10^{-3}$ mbar in every deposition because with this pressure the plume has the best shape. Finally, films are sufficiently uniform even with a substrate-to-target distance of 6 cm.

The most important parameter that influences film properties is substrate temperature. The first series of samples were deposited at different temperatures ranging from RT to 300°C using Argon as background gas. These samples were all either semitransparent or opaque with high resistivity, so they underwent two different annealing processes in order to enhance their optical and electrical properties: i) a standard annealing in air for 1 hour at 400°C or ii) a "Rapid Thermal Annealing" (RTA) in an N_2 inert atmosphere at 400°C for a variable amount of time, from minutes up to 1 hour. The main feature of RTA is that only few minutes are needed to heat the sample from RT to 400°C, while standard annealing can take up to 1 hour to reach the same temperature. Samples annealed in air showed a considerable improvement in optical transmittance and electrical properties, while RTA only enhanced electrical parameters moderately. See 3.2.2 for further information.

In light of these results, a second series of sample were deposited using Oxygen as background gas with substrate temperature ranging from RT to 300°C. All films exhibited excellent optical and electrical properties even when deposited at 100°C without requiring any post-deposition annealing, at the sole cost of a slightly reduced deposition rate compared to the deposition with Argon. Again, the substrate temperature is the crucial parameter that influences film properties.

As optical, electrical and structural analysis of ITO films deposited by PED indicates, the optimal growth conditions are summarized in table 2.3. In this configuration, the average deposition rate is 0.14 Å/pulse.

PED accelerating voltage	15 kV
Background gas type	Oxygen
Background gas pressure	$8 \cdot 10^{-3}$ mbar
Substrate type	Low cost soda lime glass
Substrate-to-target distance	6 cm
Substrate temperature	100 °C
Post deposition annealing	Not necessary

Table 2.3: Optimal growth conditions for ITO deposition via PED.

Aluminum Zinc Oxide, Gallium Zinc Oxide and Indium Zinc Oxide

Deposition of AZO, GAZO and INZO via PED were very similar. In all three cases, PED voltage and gas pressure did not influence film properties, and so were set as constant respectively at 15 kV and $6 \cdot 10^{-3}$ mbar to ensure minimum deposition time and optimal plume profile. All growths were performed on low-cost SLG substrates, using either Argon or Oxygen as indicated further on. Film uniformity is acceptable even with a substrate-to-target distance of 6 cm.
The following compositions were analyzed:

- ZnO:Al 2%wt (AZO2 samples)
- ZnO:Al 5%wt (AZO5 samples)
- ZnO:Ga 2%wt (GAZO2 samples)
- ZnO:In 2%wt (INZO2 samples)
- ZnO:In 9%wt (INZO9 samples)

A 2% wt doping is the standard concentration used by the majority of literature works, so it was realized for every dopant. The former was instead increased for AZO and INZO in order to raise respectively the carrier concentration and the electron mobility. No difference was found when depositing AZO and INZO with different dopant concentration. Targets were always polished after two depositions (three for GAZO2).

Similarly to ITO, the most important parameter that influences film properties is substrate temperature. All ZnO samples were grown between RT and 300°C in Argon atmosphere. Optical, electrical and structural characterization revealed that, apart for AZO2, best samples were obtained at 100°C with no post-deposition treatment; instead, AZO2 displays the best characteristics at 200°C.

Contrarily to what happens with ITO, there is no enhancement in optical transmittance or electrical properties if AZO or INZO films are deposited with oxygen instead of argon as background gas. This is

particularly relevant for INZO films: their transmittance is always smaller than AZO or GAZO and cannot be improved by using oxygen.

Application of AZO films to BFSC required to obtain samples with a high thickness (up to 800 micron), involving growths that lasted more than four hours. To avoid an excessive heating of target and PED cathode, a long deposition was usually split in shorter steps separated by a time interval sufficiently long to allow adequate cathode cooling. For a comparison, a single sample was instead deposited in a single 4-hour run and it showed no differences with the films deposited using the "stepped" procedure.

The optimal experimental setup was found to be the same for every considered material, and it is reported in table 2.4. Average deposition rate was different for AZO (0.05 Å/pulse), GAZO (0.09 Å/pulse) and IZO (0.12 Å/pulse) deposition being directly related to the actual physics properties of the targets.

PED accelerating voltage	15 kV
Background gas type	Argon
Background gas pressure	$6 \cdot 10^{-3}$ mbar
Substrate type	Low cost soda lime glass
Substrate-to-target distance	6 cm
Substrate temperature	100 °C (200°C only for AZO2)
Post deposition annealing	Not necessary

Table 2.4: Optimal growth conditions for AZO, GAZO and INZO deposition via PED.

2.4 Conclusions

High quality films of ITO, AZO, GAZO, IZO, and the novel material $CuGaO_2$, were successfully deposited using the PED technique with good reproducibility and uniformity. This proves that PED is a low-cost and reliable deposition technique to grow both conventional and novel TCOs.
PED deposition of each material mentioned above was optimized to achieve the best electrical and optical properties and optimal configurations are reported. The depositions of AZO, INZO and GAZO are very similar and share the same best growth conditions.

Chapter 3: Characterization of TCOs thin film grown by PED

This chapter reports electrical, optical, structural, morphological and compositional characterization of samples described in chapter 3. The discussion is introduced by a paragraph describing the various characterization procedures that were used to analyze the samples discussed afterwards. A separate section is dedicated to each studied material, stressing important results and achievements.

3.1 Main characterization techniques for layers and devices

3.1.1 UV-VIS-IR spectroscopy

UltraViolet-Visibile-InfraRed spectroscopy is an optical technique which allows to measure absorbance (*ABS*) or reflectance (*R%*) of a certain sample; transmittance (*T%*) can then be calculated using the following equation:

$$T\% = 10^{2-ABS}$$

ABS, *R%* and *T%* are defined as the fractions of electromagnetic power that are absorbed, reflected and transmitted by a thin film, respectively. Therefore, these values are usually expressed as percentages: for example, a typical good TCO has *T%* > 80% meaning that on average it transmits 80% of the total incident electromagnetic power. At IMEM-CNR, a Jasco V-530 spectrophotometer is used to perform routine UV-VIS-IR measurements working in the range between 300nm and 1100nm.

Absorbance measure allows to calculate the energy gap of a material using the "Tauc plot" approach [70]: plotting $(\alpha h\nu)^r$ versus $h\nu$ results in a graph with a linear region denoting the onset of absorption, and its extrapolation to the abscissa gives the energy gap of the material; here, $h\nu$ is the energy of an incident photon of frequency ν, r is a parameter that can be either 2 for direct a bandgap or 0.5 for an indirect bandgap, α is the absorption coefficient which is related to absorbance *A* and film thickness *t* by the relation $\alpha = 2.303\frac{A}{t}$.

Usually, an optical spectrum (*ABS*, *R%* or *T%*) of a thin film presents peaks and valleys. These occur when the incident wavelength has the same order of magnitude of the film thickness and causes constructive or destructive interference with the reflected light coming from the bottom of the film. Provided that the refractive index of the material is known, one can estimate the sample thickness from the position of

maxima and minima in the reflectance spectrum. This is the typical procedure used at IMEM-CNR to measure thin films thickness. Another approach uses a profilometer, an instrument specifically used to measure film thickness and surface roughness. For every studied material, comparison of thickness obtained by optical means and by profilometer gave almost identical results, so the former is assumed as standard procedure due to its simplicity.

3.1.2 Hall-effect and electrical measurements

A standard electrical characterization of a sample requires obtaining resistivity ρ, majority carrier mobility μ and concentration n. These values are acquired by an Hall-effect [71] measurement with electrical contacts following the Van der Pauw geometry [72].
A semiconductor in which a current I is passing is placed inside a magnetic field B so that the latter induces a perpendicular force on the flowing carriers; as a results, electrons are driven towards one side of the sample and holes towards the other side, giving rise to an electric field with a certain voltage V_H. In steady conditions, V_H is given by

$$V_H = \frac{I \cdot B}{n \cdot t \cdot e}$$

where t is the sample thickness and e the electron charge. The sign of $V_H$is the same of the carrier majority. Knowing $V_H$and ρ, one can calculate μ and n using the relations

$$n = \frac{I \cdot B}{V_H \cdot t \cdot e} \text{ and } \mu = \frac{1}{\rho \cdot e \cdot n}$$

Since usually V_H is very little (few millivolts), a precise measurement of the resistivity ρ is needed. This is obtained following the procedure proposed by Van der Pauw, which requires placing four small electrical contacts at each corner of an arbitrary shaped sample. Then, the technique involves a combination of reversing source current polarity and reversing the direction of the magnetic field (with a total of eight measurements) to obtain a resistance value averaged along the two horizontal and vertical directions. At IMEM-CNR this whole procedure is performed automatically by a specific automated setup, which only requires manually realizing the electrical contact on the film and placing it on a sample holder.

3.1.3 Scanning electron microscopy and Energy-dispersive X-Ray spectroscopy

A scanning electron microscope (SEM) is a device capable of producing images of an object by scanning their surface with an electron beam following a raster pattern. The atoms in the material's edge are excited by the beam and produce (among many different phenomena) secondary electrons, which are collected and

counted in order to reconstruct the surface's topography. Samples must be prepared so that they withstand high vacuum and are electrically conductive, otherwise charges tends to accumulate on their surfaces producing distorted images. The more advanced SEMs are now capable to achieve resolutions better than 1 nanometer.

The most important parameter of a SEM instrument is the Electron High Tension (EHT): it is directly related to the maximum depth of electron penetration h_{max} inside the material according to the relation

$$h_{max} = \frac{0.1 \cdot EHT^{1.5}}{\rho}$$

where ρ is the material density. The actual region of electron interaction inside the sample is "pear-shaped", with various processes occurring in different zones, as indicated by figure 3.1 [73]. Specific detectors can collect all these signals to obtain a detailed compositional, structural and morphological characterization.

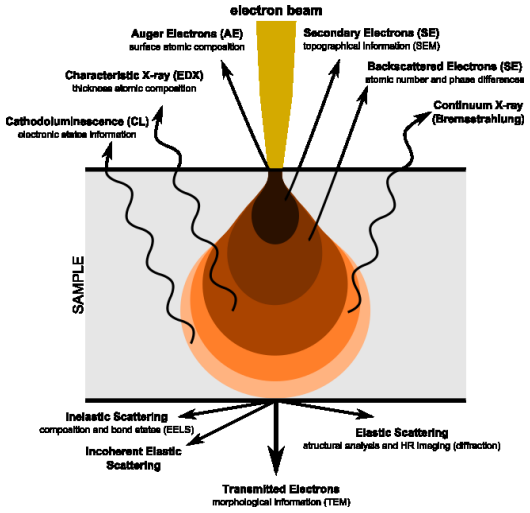

Figure 3.1: Schematic of electron beam interaction with a sample inside a SEM.

Among various processes, characteristic X-ray emission takes place when an electron of the beam collides with an inner shell electron of an atom inside the sample and ejects it from the atom itself; the hole is immediately occupied by an external shell electron, which loses energy in term of an x-ray with a distinctive frequency depending on the energy difference of the two shells. The study of x-rays emitted by the sample carries information on its composition: the peaks in the spectrum indicate which elements are present, and their relative height is related to the concentration of each element. The analysis of these x-rays is called Energy-Dispersive X-ray Spectroscopy (EDS or EDX) and it enables a fast and reliable compositional characterization. A reliable EDS measurement requires the sample to be conductive and with a thickness greater than 200/300 nm, otherwise the "pear shaped" region can reach the substrate and produce an emission of x-rays which has nothing to do with the thin layer.

At IMEM-CNR, SEM images are realized using either a Philips 515 microscope working with a maximum EHT of 30 kV or, for high-resolution pictures, a SEM-FIB Zeiss Auriga Compact microscope operating at 10 kV; it is possible to collect either surface images or cross-sectional images by simply rotating the sample holder. The Philips microscope is also equipped with an EDS Phoenix 3 apparatus using a Si:Li cooled sensors. The latter is separated from the SEM chamber by a Beryllium window in order to preserve its high vacuum. X-ray with an energy lower than 1 KeV are absorbed by this windows, thus limiting the actual detection capabilities of this EDS system: only heavier elements than Sodium are observable.

3.1.4 X-ray diffraction

X-ray diffraction (XRD) is the conventional technique used to study the crystal structure, the preferred crystallographic orientation of grains, the dimension of the unit cell and the eventual presence of unwanted phases. XRD is realized by focusing an x-ray beam onto a crystalline specimen and analyzing how it is diffracted from the sample: the various lattice planes reflects the electromagnetic wave and interference phenomena originate an emitted x-ray spectrum with peaks directly related to the crystal structure. Constructive interference is intensified by the cumulative effect of the reflection coming from successive crystallographic planes and it takes place when the phase difference of two reflected x-ray is an integer multiple *n* of the incident radiation wavelength λ at a certain angle θ according to the Bragg's law:

$$2dsin(\theta) = n\lambda$$

where λ *d* is the distance between two atomic planes. The situation is depicted in figure 3.2. As a consequence, at a given angle θ the effective diffraction angle is 2θ, naming this geometry "θ-2θ". In this thesis work only "θ-2θ" measurements were conducted, and the mail intent was to check if the sample was grown in the desired structure by comparing its spectrum to literature data.

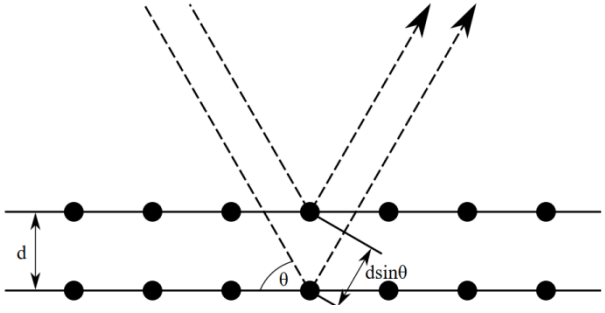

Figure 3.2: Representation of Bragg diffraction.

3.1.5 Current-Voltage measurements

The current-voltage (I-V) characteristic of a device is obtained by applying a voltage and determining the corresponding current. This is the standard technique to measure contact resistance of electrical contacts or to obtain I-V curves of a solar cell either in dark or illumination conditions. In the first case, samples were covered to avoid any external light from exciting the device; in the second case, an ABET SUN 2000 solar simulator was used, producing an AM1.5g spectrum [74] with power density of 100 mW/cm^2. The temperature was kept constant at 25°C in every measure using a cold plate. I-V curves were measured with a Keithley 2635 system. Finally, current density-voltage (J-V) curves were realized by dividing the current I by the active device area measured under an optical microscope connected to imaging software.

3.1.6 Quantum efficiency

In a solar cell, External Quantum Efficiency (EQE) gives information on the percentage of incoming photons (at a given wavelength) giving rise to an electron-hole pair contributing to the power generation. For this reason, in an EQE measurement the short circuit current of a cell is compared to the current generated by a calibration device at a given wavelength, and the EQE spectrum is then obtained by sweeping the incident light from UV to IR. The integration of this spectrum provides the J_{sc} of the solar cell. At IMEM-CNR, EQE spectra are obtained using the solar simulator previously described with a set of 16 narrow-band filters (Thorlabs FB350/1100-10) and a Silicon photodiode (Thorlabs FDS-1010-CAL) used as the calibration device. From EQE and reflectance as a percentage of illuminating intensity R_i, one can calculate the Internal Quantum Efficiency IQE using the relation:

$$IQE(\lambda) = \frac{EQE(\lambda)}{100 - R_i(\lambda)}$$

where every quantity is given at a certain wavelength λ. Only EQE measurements were realized in this thesis.

3.1.7 Secondary Ion Mass Spectroscopy

Secondary Ion Mass Spectroscopy (SIMS) is a technique used to monitor sample composition along a direction. It is realized by focusing a high-energy ion beam on a sample and measuring, with a mass spectrometer, the secondary atoms ejected from the sputtering of the material while the erosion proceeds down through the sample, resulting in a compositional analysis along the crater direction. This is useful to determine concentration gradients of elements along the film thickness. However, two potential problems must be taken into account: two ions with the same mass/charge ratio have overlapping signals and erosion from crater walls causes a memory effect.

For this thesis, SIMS measurements were realized in collaboration with FBK institute in Trento (Italy) using an instrument model Cameca SC-Ultra with a primary Cs+ ion gun with an accelerating voltage of 8 kV. The ion beam has an impact energy of 3 KeV and a current of 40 nA, and the sample is kept in high vacuum (around 10^{-9} mbar) with an applied voltage of 5 kV. Measure is realized in a 250μm×250μm raster pattern with an ion beam diameter of 75 μm and a sputtering velocity of 0.3 nm/s. All the MCs+ ion-signal profiles are normalized to the Cs+ signal. SIMS measurements were conducted to analyze the composition of CIGS bifacial solar cells along the growth direction.

3.1.8 Raman spectroscopy

Raman spectroscopy is a non-destructive technique based on the homonymous scattering phenomenon: a molecule is excited to a higher rotational or vibrational energy level due to an inelastic scattering with a photon of an incident light beam. Every molecule has its own typical vibrational spectrum, so by analyzing the light emitted from a sample it is possible to obtain much information such as chemical composition, chemical bonding and crystallographic orientation.

In this thesis, Raman measurements were conducted to monitor the Gallium content in CIGS thin films along the growth axis. This is possible because the frequency of the A_1 mode of CIGS (vibration of the anions in x-y plane with cations at rest) is linearly dependent from the Ga concentration, shifting from 184 cm^{-1} for CGS to 174 cm^{-1} for CIS. From the Raman shift R_{shift} of the A_1 mode one can calculate the GGI using the relation

$$GGI = 0.1 \cdot R_{shift} - 17.4$$

This formula was obtained by Witte et al [75] on co-evaporated CIGS and it is in acceptable agreement with our data. Nevertheless, work is being carried out to produce our own calibration curve obtained on PED-grown CIGS. In fact, the different nature of the absorber when deposited with the two techniques may result in slightly different constants in the formula above.

Depth-resolved Raman measurements were realized in collaboration with University of Parma using a micro-Raman apparatus (Horiba Jobin-Yvon Labram) equipped with a confocal microscope (Olympus BH-4) with 4, 10, 50, ULWD 50 and 100 objectives (lateral spatial resolutions of approximately 25, 10, 2.2 and 1μm). The spectrometer uses a 20 mW He-Ne laser emitting at 632.8 nm, an edge filter, a 256×1024 pixel CCD detector, a 1800 grooves/mm grating, and a density filter wheel. The instrument is calibrated at the silicon Raman peak of 520.6 cm^{-1} before each measurement. The spectra were recorded at different sample depths using the 100 objective: each datum is the mean of 4 repetitions lasting 30 s each, or the average of 30 measurements of 10 s repeated 2 times each obtained mapping a 20 μm × 40 μm sample area. Peak fitting was carried out using a Lorentzian function.

3.2 Characterization of PED-grown TCOs

3.2.1 $CuGaO_2$

There is no literature regarding deposition of $CuGaO_2$ via PED, therefore a detailed discussion is reported highlighting how various film characteristics are influenced by growth parameters.

Deposition rate

Table 3.1 report average deposition rate as a function of oxygen pressure in chamber and of PED accelerating voltages with a target-substrate distance of 6 cm and at RT.

O_2 pressure (mbar)	Average rate (Å/sec)
$6 \cdot 10^{-3}$	0.083
$8 \cdot 10^{-3}$	0.44
$1 \cdot 10^{-2}$	0.59
$2 \cdot 10^{-2}$	0.28

Voltage (kV)	Average rate (Å/sec)
14	0.24
16	0.23
18	0.25
20	0.21

Table 3.1: Average deposition rates with different oxygen pressures (first series of samples deposited at 14 kV) and PED accelerating voltages (second series of samples deposited at $1 \cdot 10^{-2}$ mbar).

The degradation of targets' surface after one or two growths is a key aspect limiting the deposition rate: in order to ensure maximum growth speed targets were manually polished after each deposition. Fastest depositions occur with an O_2 pressure of $1 \cdot 10^{-2}$ mbar: a lower pressure causes a less efficient electron discharge and a subsequent poor target ablation while a higher pressure results in a smaller plasma plume. Deposition rate is substantially independent from electron accelerating voltage above 12 kV.

Film morphology

All films display the classic aspect of PED-grown samples: the surface is covered by small droplets originated from macroscopic ablation of the target with sizes varying from micrometers to nanometers. No other particular features were observed, and, in addition, the oxygen partial pressure was found to have no influence on surface morphology.

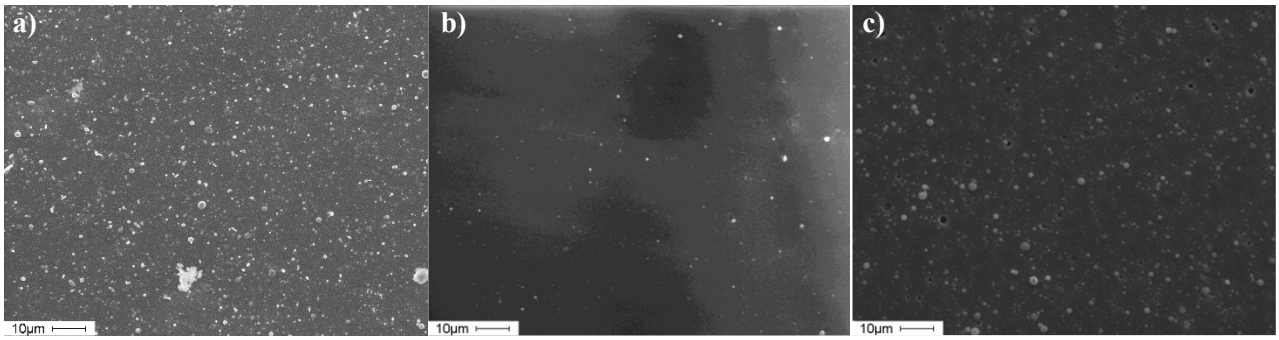

Figure 3.3: Surface of films respectively grown at 14 kV (a), 16kV (b) and 18kV (c), with an oxygen pressure of $1 \cdot 10^{-2}$ mbar and at RT. SEM was operating with EHT = 25 kV.

PED voltage has a strong influence on film morphology: as can be seen from figure 3.3, the sample grown at 18 kV presents small hollow zones mainly caused by semi-enclosed droplets which have detached themselves or by surface damaged induced by electrons during depositions. On the contrary, the sample obtained at 16 kV or 14 kV features almost no damaged areas and smaller droplets. No significant differences are instead found on film deposited at 16 kV and 14 kV, as can be seen from figure 3.3(a) and 3.3(b).

Substrate temperature has also an influence on film morphology, as indicated from figure 3.4.

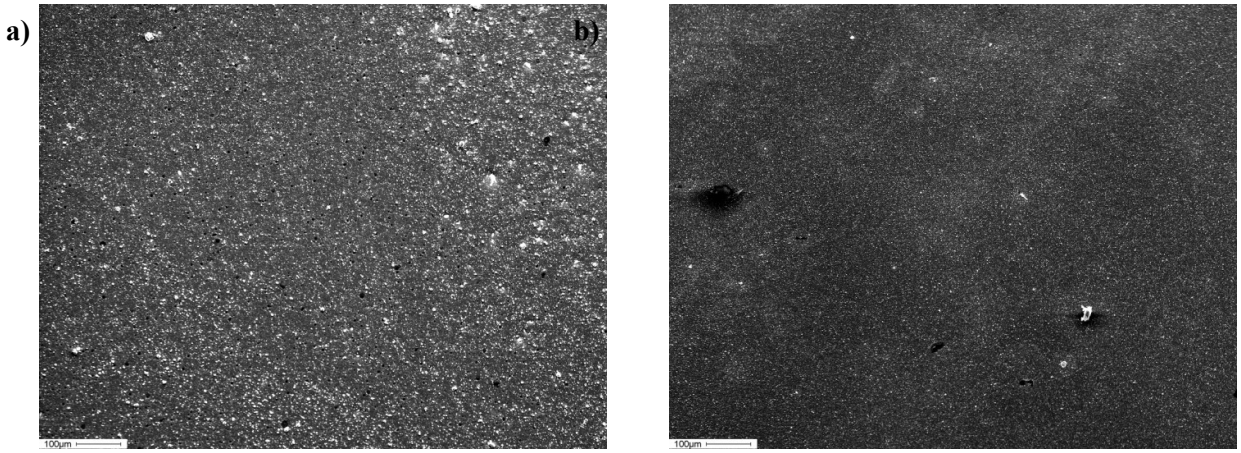

Figure 3.4: Surface morphologies of films grown respectively at RT (left) and 350°C (right), with an oxygen pressure of $1 \cdot 10^{-2}$ mbar and a PED voltage of 16 kV. SEM was operating with EHT = 25 kV.

The only notable feature is that the surface of film deposited at T = 350°C presents less damaged zones and smaller droplets: the high temperature and the consequent increased surface mobility allows them to be rearranged and partially dissolved into the growing film. This analysis indicate that the best morphology is achieved in films deposited at high temperature (T>350°C) with a PED accelerating voltage of 16 kV.

Optical characterization

Absorbance measurements were conducted to determine the sample's energy gap following the Tauc plot approach [70]. No significant differences were found among various samples, which all exhibited absorbance spectra and Tauc Plots similar to the ones reported in figure 3.5.

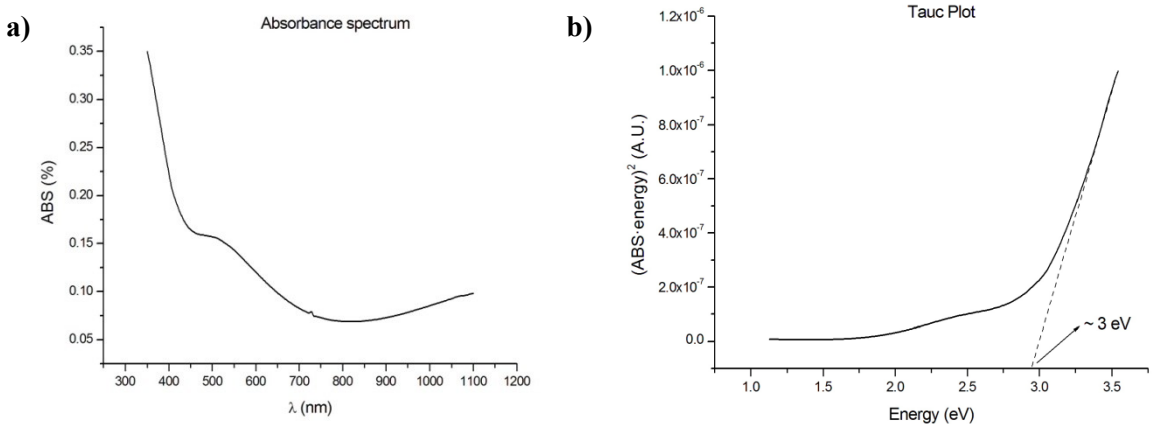

Figure 3.5: Typical absorbance spectrum (a) and Tauc Plot (b) of $CuGaO_2$ films measured between 350 nm and 1100nm. Right figure also contains the extrapolation of the linear region used to determine the band-gap.

Absorbance spectra are almost independent from every growth parameters, only a minor increase of absorbance is observed in thicker films as expected. The average value between 350 nm and 1200 nm of every deposited film is 20.3% ± 10.6%. The little shoulder around 550 nm in the absorption spectrum is responsible for the different slope of the Tauc plot between 2 eV and 2.5 eV. It could be due either to the presence of secondary phases in samples with a reduced band gap or by the Urbach's tail from localized states within the bandgap. The second explanation is probably the right one, since the shoulder also appears in the absorption spectra of samples obtained from the Cu-rich target after a high temperature annealing. In addition, no secondary phases were detected by XRD spectra, although small quasi-amorphous inclusions cannot be excluded.

The energy gap, as derived from Tauc plots, is also independent from growth parameters. Analysis of various spectra revealed that the average energy gap is 2.96 ± 0.08 eV, with data ranging from 2.8 eV to 3.1 eV. These values are all lower than those reported in literature [76] and are probably due to the formation of a gallium-rich delafossite compound with a chemical formula $Cu_{1-x}Ga_{1+x}O_2$ and x of the order of 5-6%. This excess of gallium can be caused by several possible factors, the most probable being interstitials or substitutional defects spontaneously forming during deposition.

Film composition

Film composition was investigated using the EDS technique. Only copper and gallium concentration are measurable since k-lines of oxygen have energies blocked by the beryllium window. The desired composition for pure delafossite phase would be 50%Cu and 50%Ga.

Table 3.2 reports average copper concentration in films with different oxygen pressures and PED accelerating voltage; substrate temperature does not alter sample composition.

O_2 pressure (mbar)	%Cu	Voltage (kV)	%Cu
$6 \cdot 10^{-3}$	30	14	39
$8 \cdot 10^{-3}$	35	16	40
$1 \cdot 10^{-2}$	43	18	42
$2 \cdot 10^{-2}$	43	20	42

Table 3.2: Average copper concentration with different oxygen pressure (left) and PED accelerating voltage (right). Left samples were grown with PED voltage = 16 kV, right samples were deposited with oxygen pressure = $1 \cdot 10^{-2}$ mbar.

A slight variation of the oxygen pressure leads to a major difference in film composition, with values as close as the stoichiometric one for pressures higher than $1 \cdot 10^{-2}$ mbar. A very similar trend was observed in literature for a different delafossite via Pulsed Laser Deposition [68], and therefore seems a common feature of high-energy pulsed deposition techniques of doped copper oxides.

All samples have a copper concentration lower than the desired one, which can be explained by the presence with the formation of an unwanted Ga-rich phase with a chemical formula $Cu_{0.44}Ga_{0.56}O_2$. This confirms the assumption made in the previous section and would account for the reduced bandgap.

Target composition	Average %Cu in samples
50%Cu/50%Ga	33.3 %
60%Cu/40%Ga	38.0 %
75%Cu/25%Ga	49.2 %

Table 3.3: average copper concentration in samples obtained from targets with different compositions.

Since all sample were deficient in copper, growth from Cu-rich targets with different Cu to Ga ratio were performed in order to obtain films with a stoichiometric composition. As table 3.3 reports, samples grown from a target with a ratio of 75%Cu/25%Ga have an average copper concentration of 49.2%, very close to the required stoichiometric one. Therefore, standard successive growths were realized using this non-stoichiometric target. One has to note that for these Cu-based compounds, the PED does not reproduce the composition of the target. This unusual behavior clashes with the principles of the PED and is not easily to explain. It seems that Cu is much more volatile that other elements and tends to desorb from the layer surface before being oxidized. Further work is needed to find the optimal deposition condition of $CuGaO_2$ via LTPED. Indeed, table 2.2 summarizes our best deposition conditions with our commercial PED source.

Structural and electric characterization

Figure 3.6 reports XRD spectra of a sample deposited at 450°C using the non-stoichiometric target.

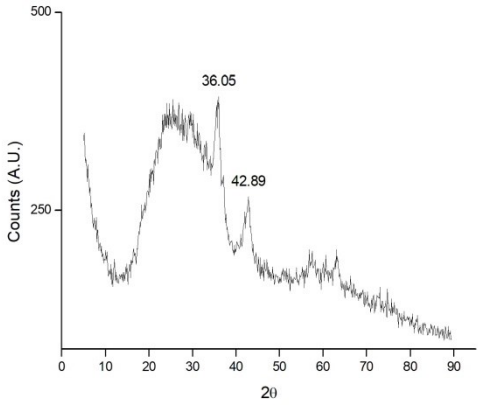

Figure 3.6: XRD spectra of sample deposited on glass substrates using a non-stoichiometric at T= 450°C.

The moderate peak at 36.05° is consistent with the (012) peak (2θ=36.1°) of delafossite phase of $CuGaO_2$ [77], confirming the presence of very small grains of crystalline delafossite still immersed in an amorphous matrix. The peak at 2θ=42.89° can instead be identified as the (200) peak of Cu_2O.

Despite growing at T as high as 450°C only small crystallites are formed with an incorrect stoichiometry. As reported in [31], the delafossite phase in the system Cu-Ga-O is the stable phase at a temperature of at least 1000°C with an oxygen pressure of 10^{-2} mbar. Therefore, in order to favor crystallization in the correct phase, samples underwent various post deposition annealing in air at a temperature higher than 1000°C with a duration ranging from 1 hour to 4 hours. It was necessary to replace glass substrates with sapphire substrates which should also help crystallization directly during deposition.

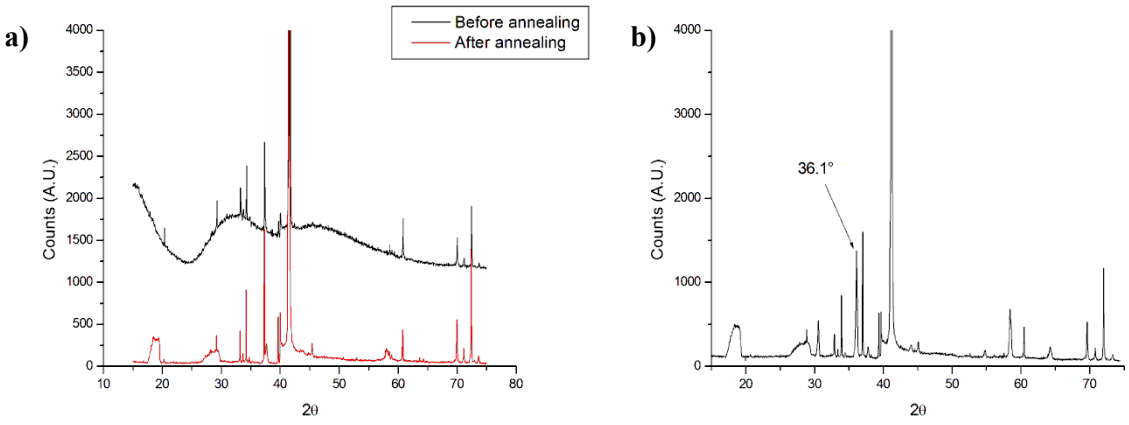

Figure 3.7: XRD spectra of sample deposited on sapphire substrates using a stoichiometric target (a) and copper-rich target (b) before (a-black curve) and after (a-red curve and right) high temperature annealing (4h, 1200°C, in air).

Figure 3.7(a) compares XRD spectra of the same sample before (black curve) and after (red curve) an annealing of 4 hours in air at 1200°C. This sample is grown using a 50%Cu/50%Ga target. The $CuGaO_2$ delafossite peak is in both spectra either absent or too small to be recognized, confirming that no crystallization in the delafossite phase occurs when depositing from a stoichiometric target. Highest peak at 41.3° is originated from sapphire substrate.

Figure 3.7(b) reports the XRD spectrum of a sample deposited using the non-stoichiometric target (75%Cu/25%Ga) after a 4 hours annealing at 1200°C in air. This spectrum is similar to those reported in the left figure except for the presence of a moderate peak at 36.1°, which is consistent with the delafossite phase of $CuGaO_2$. Therefore, a 4 hours high T annealing is necessary to nucleate small delafossite grains which are still surrounded by various copper oxides and/or amorphous material. Further work is then required to optimize the growth of crystalline $CuGaO_2$ using PED.

All samples of $CuGaO_2$ discussed in this chapter possess a high resistivity typically above 10^8 Ω·cm, behaving as electrical insulators. No attempts of doping $CuGaO_2$ with Fe, which would increase hole mobility and concentration, were made due to the difficulties to realize a crystalline delafossite phase.

Although we confirmed the formation of the $CuGaO_2$ phase, the need of the expensive sapphire substrate and the high temperature annealing hinders the application of this TCO to CIGS-based BFSCs. For this reason we focused our attention on conventional n-type TCOs.

3.2.2 Indium Tin Oxide

As anticipated in 2.3.2, the only deposition parameter that influences ITO films properties is the substrate temperature, as will be discussed in this section. Analysis of samples deposited with different PED voltages showed no significant differences in terms of transparency and resistivity. Compositional analysis of ITO using EDS is difficult since Indium and Tin have overlapping peaks in the x-ray spectrum, so it was not realized on these samples.

Structural characterization

Thanks to the high energy supplied by PED, it is possible to grow crystalline thin films of ITO on soda lime glass at a substrate temperature as low as 100°C, as indicated in figure 3.8. Samples deposited at RT have an amorphous structure.

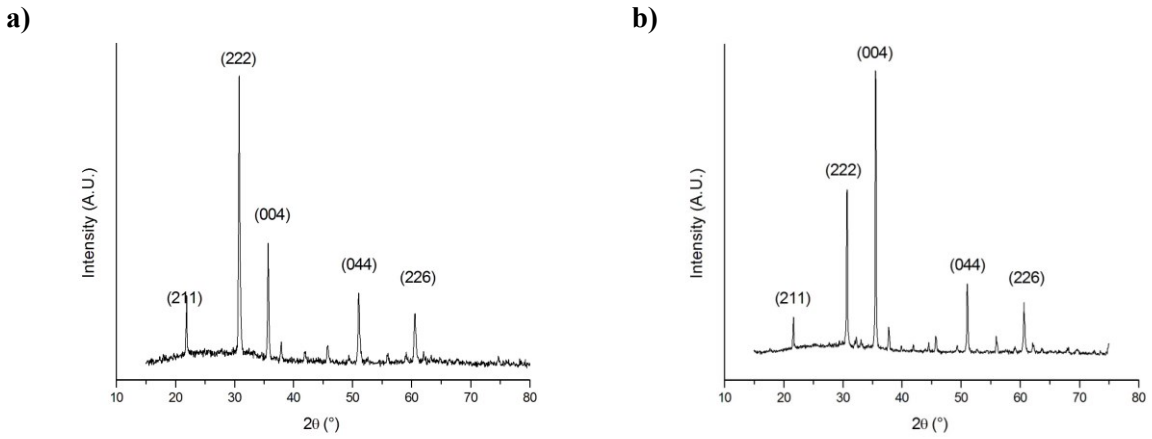

Figure 3.8: XRD spectra of ITO samples deposited on soda lime glass with a substrate temperature of 100°C (a) and 300°C (b). PED voltage was set at 15 kV, Oxygen pressure at $8 \cdot 10^{-3}$ mbar

This spectrum is comparable to those reported in literature for ITO deposited at a much higher temperature, see for example [78], and clearly indicates that the preferred orientation of PED-grown ITO is along the (222) direction for films grown at 100°C. No differences are found if ITO is deposited at 300°C (figure 3.8(b)), except for the preferred growth direction.

Optical characterization

All ITO samples deposited using Argon as background gas are semitransparent or even opaque. Two different annealing processes were then applied to enhance their optical properties:

1) standard annealing in air at 400°C for 1 hour; whereby the heating ramp takes 2 hours to reach 400°C and additional 3 hours are necessary to cool the sample down to room temperature.
2) annealing in nitrogen atmosphere for 1 hour; here the heating ramp is only one minute and the cooling ramp few minutes. For this reason, we define it as "RTA" (rapid thermal annealing) although clearly different from the one extensively applied in the semiconductor device processing.
3)

Figure 3.9(a) reports optical transmittance, obtained from absorbance data, of an ITO film as deposited (blue line) and after both annealing processes realized on two separate parts of the sample. The material became transparent only after the annealing in air, confirming that the opacity is probably due to oxygen vacancies forming during growth in Argon atmosphere.

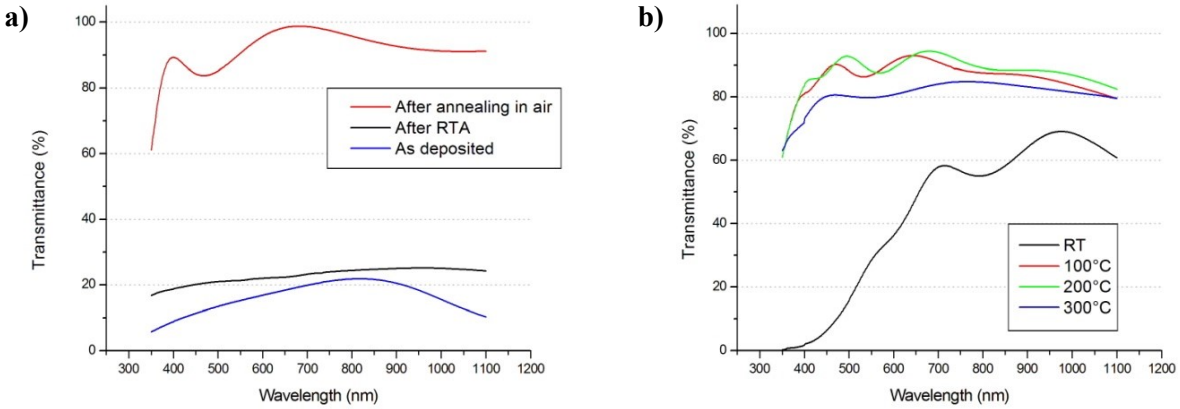

Figure 3.9: Transmittance of ITO samples deposited in argon atmosphere before and after different annealing procedures (a) and at different substrate temperatures in oxygen atmosphere (b).

In light of this result, the second series of depositions using Oxygen as processing gas resulted in much more transparent materials, as indicated by figure 3.9(b). The film grown at RT is amorphous and therefore opaque, while samples grown at temperatures above 100°C have comparable transmittances. In particular, the average transmittance between 400nm and 1200nm of films deposited at 100° and 200° is respectively 87% and 88%. This confirms that high transparency is achieved even at these low T. The average bandgap of ITO films resulted to be 3.6 eV, in agreement with data from literature [79].

Electrical characterization

Table 3.4 reports resistivity ρ, mobility μ and carrier concentration n of ITO thin films grown at different substrate temperature T.

T (°C)	ρ ($\cdot 10^{-4}$ Ω·cm)	μ (cm^2/V·s)	n ($\cdot 10^{20}$ cm^{-3})
RT	91	5.7	1.1
100	1.9	34	9.7
200	2.3	33	8.3
300	2.2	32	9.0

Table 3.4: Electrical characterization of ITO samples deposited at different temperatures. Values are obtained using Hall-effect measurements.

Film obtained at RT shows the highest resistivity due to its amorphous structure. The lowest ρ is achieved with a substrate temperature of 100°C; no significant differences can be found among samples grown at higher T in terms of ρ, μ and n. These values are comparable with top-notch samples deposited via sputtering [80] or pulsed laser deposition [81].

Electrical, structural and optical characterization indicates that PED is capable of depositing excellent ITO films with a substrate temperature as low as 100°C.

3.2.3 Doped Zinc Oxides

In light of the results of 3.2.2, this section reports optical, electrical and structural properties of AZO, GAZO and INZO only as a function of deposition temperature and background gas type. Samples deposited with different PED voltages or background gas pressures showed no significant electrical or optical differences.

Structural characterization

Figure 3.10 reports XRD spectrum and atomic force microscope surface image of AZO2, GAZO2, and INZO2 samples deposited on soda lime glass with a substrate temperature of 100°C.

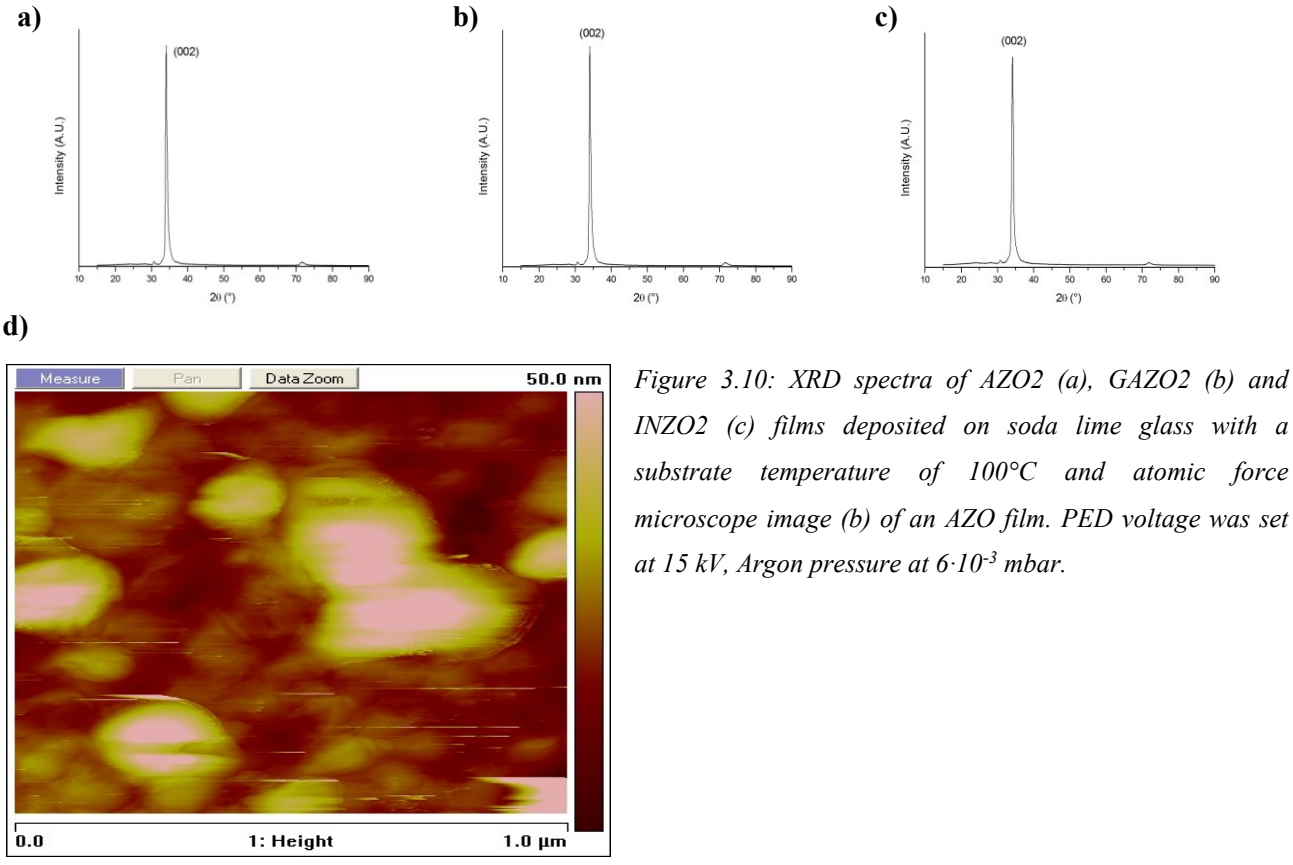

Figure 3.10: XRD spectra of AZO2 (a), GAZO2 (b) and INZO2 (c) films deposited on soda lime glass with a substrate temperature of 100°C and atomic force microscope image (b) of an AZO film. PED voltage was set at 15 kV, Argon pressure at $6 \cdot 10^{-3}$ mbar.

Samples show a crystalline structure, growing along the (002) direction, even when deposited at a substrate temperature as low as 100°C, while depositing at RT results in amorphous films. AFM image reveals an average grain size of the AZO film between 150 nm and 200 nm. No differences are found in samples deposited at 200°C or 300°C.

Optical characterization

Transmittance measurements, obtained from absorbance data, of best AZO2, AZO5, GAZO2 and INZO2 films grown at different substrate temperatures are reported in figure 3.11.

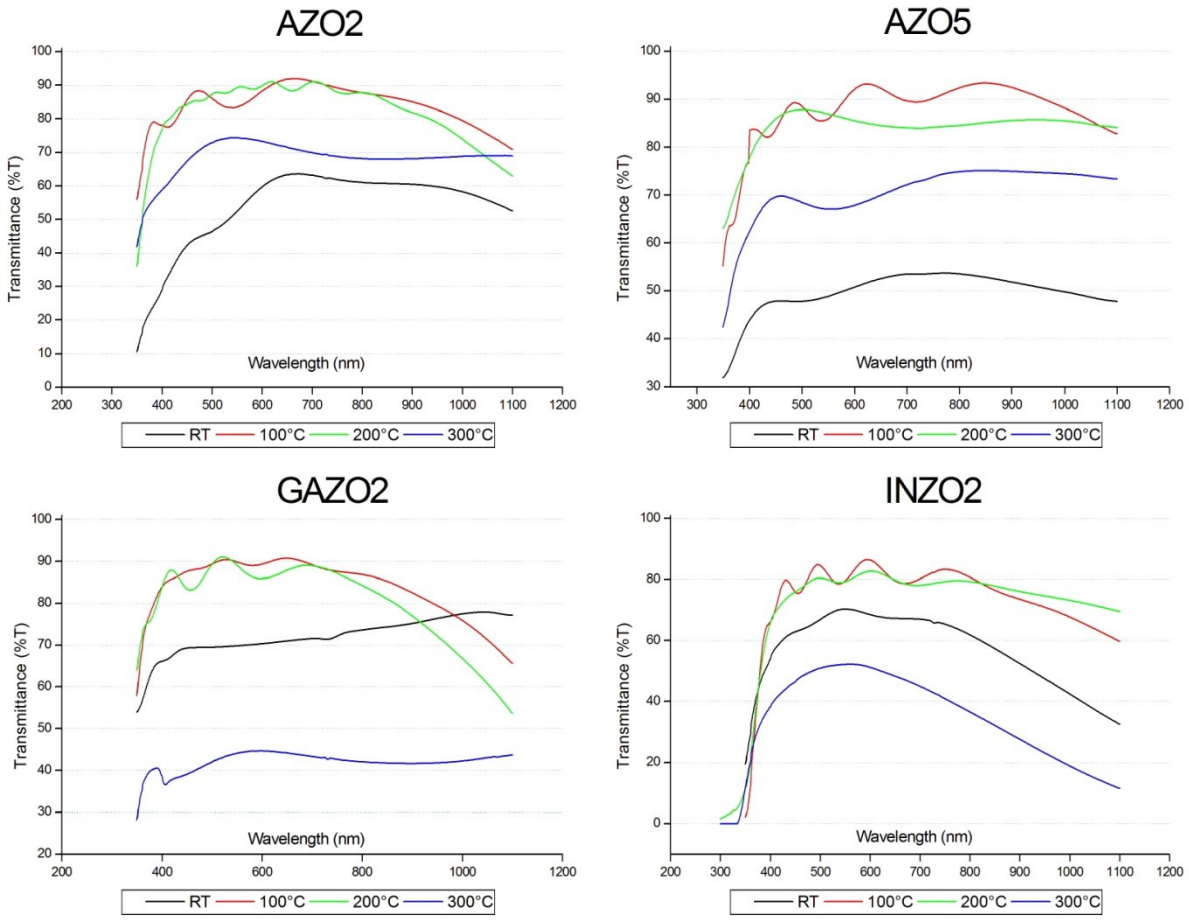

Figure 3.11: Transmittance spectra of AZO2, AZO5, GAZO2 and INZO2 samples as a function of deposition temperature, as reported in the legends. INZO9 has the same trend of INZO2 and it is not reported.

In all TCOs, the transmittance is maximized in materials deposited either at 100°C or 200°C, with average value above 80%. The lower transmittance of films grown at RT is due to their amorphous structure and, surprisingly, samples deposited at T=300°C also show a reduced transmittance. Literature [82] reports that when AZO is deposited at T>400°C Zn vacancies are formed acting as electron traps; it is probable that these defects also introduce new shallow levels near the valence band which eventually increase the absorbance of the material and justifies the reduction of the transmittance.

GAZO2 possesses a higher carrier concentration than AZO and INZO, as reported in the next section, leading to an increased free carrier absorption and a consequently smaller transmittance at wavelengths above 900nm.

All INZO films are less transparent than AZO or GAZO. Following the approach used for ITO, an INZO sample underwent two different annealing procedures at 400°C in order to enhance its optical properties: a standard annealing in air for 4 hours and an RTA in Argon for 1 hour. Moreover, two samples realized using two different gases (argon and oxygen) and the same deposition setup were compared in order to investigate potential benefits of O_2 growth ambient on optical properties.

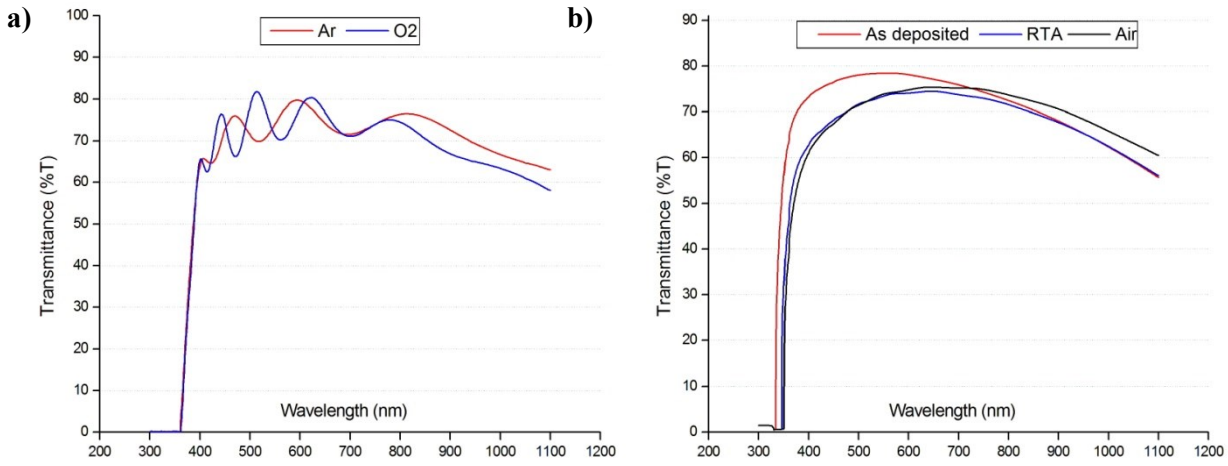

Figure 3.12: Transmittance spectra of two INZO2 samples realized using Ar or O_2 processing gas using the same deposition parameters (a) and of an INZO2 sample before and after different annealing processes (b). All films are realized at 100°C

As one can see from figure 3.12, contrary to the case of ITO no significant enhancements in transmittance are observed either annealing a sample in air or depositing in an oxygen atmosphere. The same results are obtained on INZO9 films.

Average transmittance and bandgap of the five studied TCO are reported in table 3.5. Energy gap values are consistent to that of zinc oxide and the slight increase of AZO5 and INZO9 bandgap with respect to AZO2 and INZO2 can be explained with the Burstein-Moss effect, since the former have higher carrier concentrations than the latter. Compared to AZO2 deposited by sputtering at IMEM-CNR [83], PED-grown AZO2 has fairly higher optical transmittance with an average T% of 86% compared to 81%.

	T% (%)	Bandgap (eV)
AZO2	86	3.3
AZO5	89	3.4
GAZO2	85	3.3
INZO2	76	3.3
INZO9	73	3.4

Table 3.5: Average T% (between 400nm and 1200nm) and bandgap (obtained using the Tauc plot approach) of the five studied TCO. Samples are deposited at 100°C.

As a conclusion, PED-grown TCOs at a substrate temperature as low as 100°C display excellent optical properties: while INZO samples exhibits an average transmittance never above 80%, AZO2 and GAZO2 films have values above 85% and, in the case of AZO5, near 90%. This last value is slightly higher than ITO, confirming the high quality of the TCOs grown by LTPED, and it is comparable to literature data for good AZO films deposited with different techniques at higher temperatures [84].

Electrical characterization

Table 3.6 reports resistivity ρ, mobility μ and carrier concentration n of the TCOs studied in this thesis at different substrate temperature T.

	T (°C)	RT	100	200	300
AZO2	ρ (10^{-4} Ω·cm)	21	6.4	4.9	5.4
	μ ($cm^2/V·s$)	4.9	36	34	3
	n (10^{20} cm^{-3})	6.0	3.4	3.6	3.1
AZO5	ρ (10^{-4} Ω·cm)	62	3.2	3.4	9.5
	μ ($cm^2/V·s$)	5.1	38	29	4.1
	n (10^{20} cm^{-3})	5.6	5.9	6.3	1.6
GAZO2	ρ (10^{-4} Ω·cm)	12	2.5	2.5	8.4
	μ ($cm^2/V·s$)	7.5	19	22	21
	n (10^{20} cm^{-3})	7.5	14	11	3.4
INZO2	ρ (10^{-4} Ω·cm)	27	14	15	27
	μ ($cm^2/V·s$)	6.9	7.9	9	11
	n (10^{20} cm^{-3})	4.9	6.1	4.7	2.1
INZO9	ρ (10^{-4} Ω·cm)	34	21	21	32
	μ ($cm^2/V·s$)	2.9	4.9	9.9	13
	n (10^{20} cm^{-3})	7.0	6.1	5.4	2.6

Table 3.6: Electrical characterization of the studied TCO using Hall-effect measurements.

AZO5, GAZO2 and INZO display the best electrical properties when deposited at a temperature of 100°C (AZO2 at 200°C), while growing at RT results in amorphous samples with poorer performances. In particular, at 100°C AZO5 resistivity is as low as $3.2 \cdot 10^{-4}$ Ω·cm, a value comparable to excellent AZO films reported by literature [84] obtained at higher temperatures. GAZO2 has an even lower resistivity of $2.5 \cdot 10^{-4}$ Ω·cm, very close to the best value of ITO films, a result comparable with best values reported in literature [85] for GAZO films. INZO samples show resistances one order of magnitude higher than AZO or GAZO independently of the deposition temperature. This is easily explained by considering that the experimental electron mobility in INZO is much lower than those of the other TCOs, with values never above 10 $cm^2/V·s$.

In fact, a recent literature work [86] indicate that the Indium wt% in INZO must be greater than 64% to achieve an electron mobility above 30 $cm^2/V \cdot s$. Further work is then required to enhance the electrical properties of INZO films from the electrical point of view, too.

Every zinc-based TCO studied in this thesis possesses a common feature: samples deposited at 300°C have a lower carrier concentration (and a higher resistivity) with respect to films deposited at 100°C or 200°C. Literature [82] reports an explanation for this phenomenon: when AZO is deposited or annealed at high temperature (T>400°C) a portion of Zinc can desorbe from the film leaving acceptor-type Zn vacancies in the lattice, which compensate free electrons in the conduction band leading to a reduced carrier concentration. It is very likely that the high energy supplied by PED during growth allows these processes to happen even at a temperature of 300°C.

To summarize, zinc-based TCO deposited via LTPED displays excellent electrical properties in term of resistivity and mobility when deposited at temperature as low as 100°C, with a resistivity comparable to high quality literature data. Deposition at RT or at T > 300°C leads to lower performances due to amorphous film or to carrier compensation, respectively.

3.3 Film comparison

It is useful to compare the electrical and optical properties of the TCO studied in this thesis in order to find out which is the best candidates to be used as a back contact in CIGS-based BFSC.

Results reported in 4.4.1 indicate that BFSCs deposited on commercial FTO back contacts exhibit performances comparable to standard cells deposited on Molybdenum. Therefore, the electrical and optical characterization of FTO was assumed to be the reference for choosing which PED-deposited TCOs are suitable to be implemented as back contacts. FTO transmittance (obtained from absorbance data) and electrical characterization (acquired from Hall-effect measurements) are reported in the following graphs as reference.

3.3.1 Optical transmittance

Figure 3.13 compares transmittance spectra of all studied TCO deposited at T=100°C, while table 3.7 reports average values between 400nm and 1200 nm. FTO is added as a reference. All samples had a comparable thickness of about 400 nm.

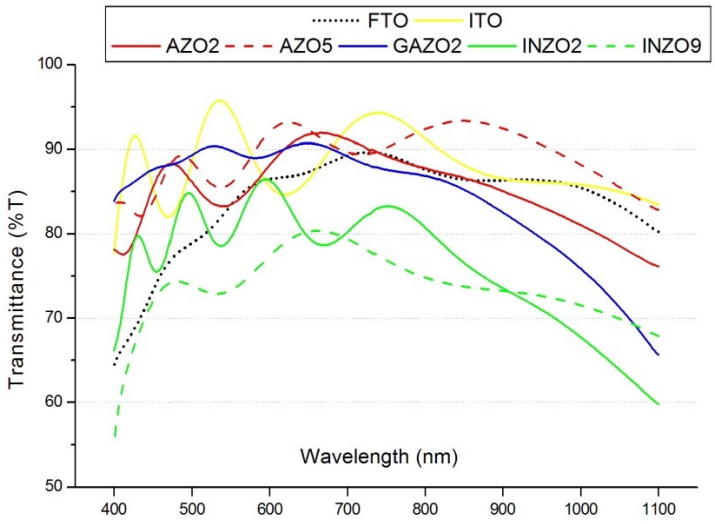

Material	Average T% (%)
FTO	84
ITO	88
AZO2	85
AZO5	89
GAZO2	84
INZO2	76
INZO9	74

Transmittance spectra (figure 3.13) and average values (table 3.7) of ITO, AZO, GAZO and INZO samples.

The most transparent materials are ITO, AZO and GAZO2: their average transmittance is above 84% (the reference one) in the whole range, and in particular AZO5 reaches up to 89%. At high wavelengths the contribution of the free carrier absorption is quite relevant for all materials and especially for GAZO2 due to its higher carrier concentration. It is worth noting that between 400nm and 600nm AZO, GAZO2 and ITO are considerably more transparent than the FTO reference.

To conclude, as far as optical properties are concerned, the best TCOs candidates to be used as transparent back contact in a CIGS BFSC are ITO and AZO2 and 5, and secondarily GAZO2.

3.3.2 Electrical properties

Figure 3.14, 3.15 and 3.16 report and compare all electrical measurements discussed in the previous paragraphs.

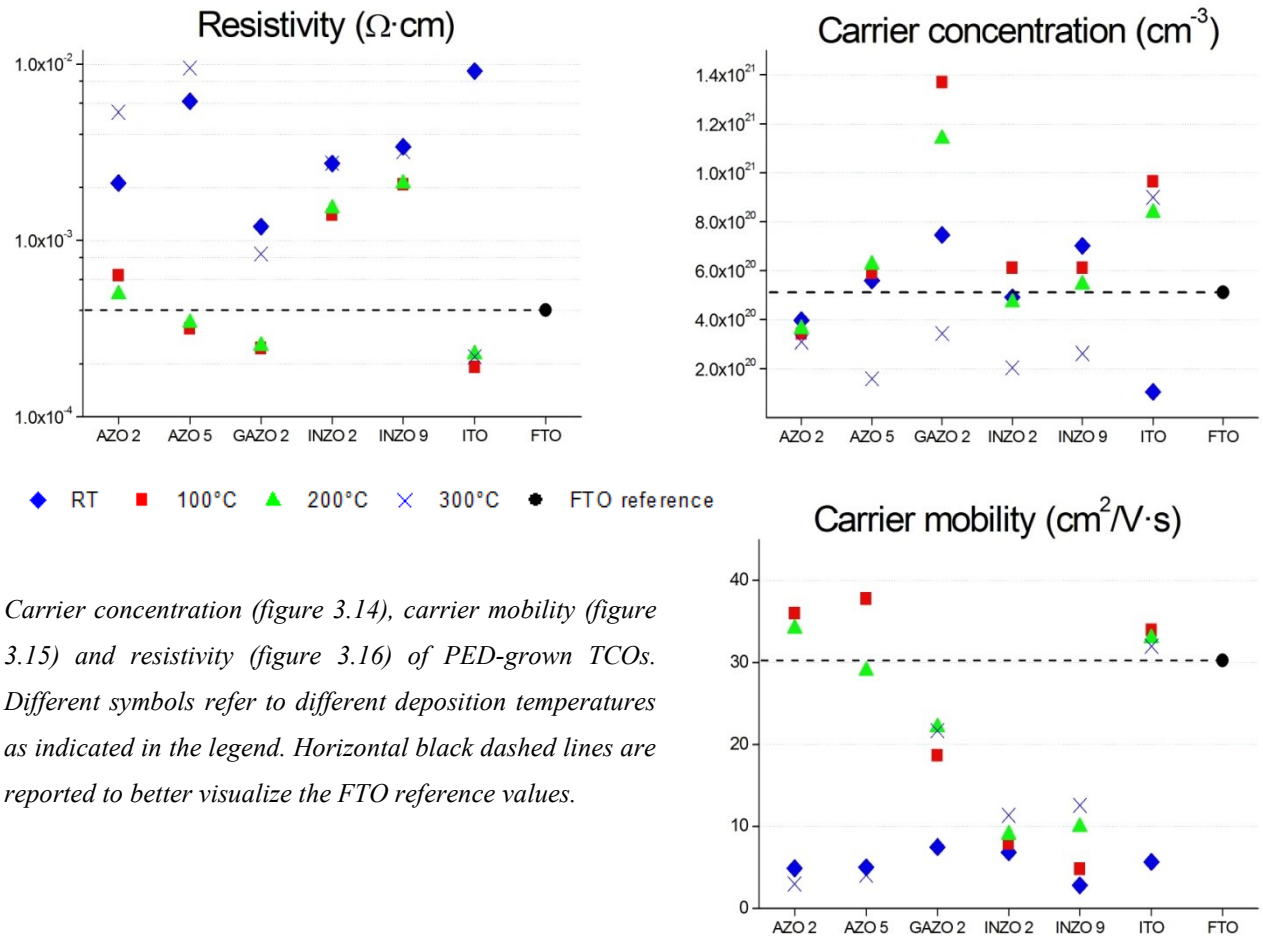

Carrier concentration (figure 3.14), carrier mobility (figure 3.15) and resistivity (figure 3.16) of PED-grown TCOs. Different symbols refer to different deposition temperatures as indicated in the legend. Horizontal black dashed lines are reported to better visualize the FTO reference values.

In light of the results reported in 4.2, an n-type TCO requires a carrier concentration greater than $5 \cdot 10^{20}$ cm^{-3} to be used as a back contact in a CIGS-based BFSC; the reference value of FTO, $5.1 \cdot 10^{20}$ cm^{-3}, is only slightly higher than this number. Figure 3.14 shows that only AZO2 does not fulfill this requirement and, remarkably, that GAZO2 possesses a carrier density even higher than ITO. This analysis proves that the usual 2% wt Al concentration in AZO is not sufficient to reach an average carrier concentration above $5 \cdot 10^{20}$ cm^{-3}, and justifies the necessity to increase Aluminum doping up to 5% wt.

Only AZO and ITO mobilities (figure 3.15) are comparable to the reference value of FTO (30 $cm^2/V \cdot s$), and GAZO2 reaches only a value as high as 20 $cm^2/V \cdot s$. The even lower mobilities of INZO are responsible for its higher resistivity.

Figure 3.16 indicates that AZO, GAZO2 and ITO are the only TCOs with a resistivity lower than the reference value of FTO ($4.0 \cdot 10^{-4}$ $\Omega \cdot cm$), and their best values are obtained at T=100°C The resistivity of INZO is in any case too high to be used as a back contact in a BFSC.

To summarize, as far as electrical properties are concerned, the best TCOs candidate to be used as transparent back contact in a CIGS BFSC are ITO, AZO5 and GAZO2: INZO has a resistivity too high while AZO2 does not possess the necessary carrier concentration.

3.4 Conclusions

$CuGaO_2$ deposited by PED is crystalline only on sapphire substrates and after a 4 hours post deposition annealing in air at temperatures above 1200°C. For this reason, although we confirmed the formation of the delafossite phase, the need of the expensive sapphire substrate and the high temperature annealing hinders the application of this TCO to CIGS-based BFSCs.

LTPED has instead proved to be a reproducible and reliable technique to grow n-type conventional TCOs. ZnO:Al 2% or 5%, ZnO:Ga 2%, ZnO:In 2% or 9% and ITO films were realized via LTPED showing a crystalline structure and excellent electrical and optical properties at a deposition temperature as low as 100°C on low cost soda lime glass substrates. The results obtained in the course of this thesis work are comparable to those reported in literature even for higher deposition temperatures.

LTPED deposited ITO, AZO and GAZO films display an average transmittance above 85% between 400nm and 1200nm and a bandgap above 3.3 eV, making them very transparent to visible, near IR and near UV radiation. Among the three materials, GAZO exhibits the greatest free carrier absorption at wavelengths above 900 nm due to its higher carrier concentration. INZO average transmittance is always at least 10% lower, and no enhancements are obtained both by performing a post deposition annealing in air or by depositing in an oxygen atmosphere.

Samples deposited at 100°C of ITO, AZO5 and GAZO2 show a resistivity lower than $4 \cdot 10^{-4}$ Ω·cm and a carrier concentration above $5 \cdot 10^{20}$ cm^{-3}. In addition, ITO and AZO have a comparable mobility above 35 $cm^2/V \cdot s$ while GAZO2 can only reach up to 20 $cm^2/V \cdot s$. All these numbers are superior to the values of commercial FTO, which is assumed as reference due to its excellent performance when used as a back contact in a CIGS-based BFSC.

By comparing the electrical and optical properties of the various TCOs, it was found that the best candidates to be used as back contacts are ITO, AZO5 and GAZO2 deposited at 100°C via LTPED.

Chapter 4: CIGS-based bifacial solar cells

This chapter reports on bifacial solar cells based on CIGS deposited by LTPED at T = 250°C onto the substrates described in the previous chapter. The experimental section regarding AZO as back contact was published in the article [87].

4.1. Introduction

In recent years, despite the introduction in PV of new emerging class of materials, for example kesterites and perovskites, the market is still dominated by standard flat panels with no important differences in terms of innovation between silicon or thin film technologies. The most remarkable results are given by the slow but steady increase in the efficiency of solar cells and modules as well as by cost reduction. However, there is a very interesting innovation recently resumed by the PV research community, namely the bifacial solar cell. This class of devices finds optimal applications in the field of building integrated photovoltaics (BIPV) [88], where PV equipment are used to replace or integrate conventional building features like rooftops or facades.

4.1.1. Principles of bifacial solar cells

A BFSC is a photovoltaic cell capable of absorbing sunlight from both the front and the backside of the device. The ideal installation of a BFSC would be in vertical arrangements, where front and back surface of the cell are exposed alternatively to illumination at different time of the day (figure 4.1(a)) or in situations where the back surface can take advantage of the albedo from the surrounding environment (figure 4.1-(b)). The effective albedo spectral irradiance depends on the materials in the close vicinity to the solar cell, as indicated by figure 4.1(c).

Figure 4.1: Examples of installation of BFSC (a and b) and albedo irradiance from different materials compared to the solar spectral irradiance (black curve) [89] (c)

As a result, a potential increase of the generated current up to 20% is possible by substituting a conventional photovoltaic cell with a bifacial cell, with a consequent reduction in terms of cost per power unit. The generated electric power can further be raised up to 50% if a concentrator is used to focus the albedo light on the back surface [90].

The realization of a bifacial device dates back to the second half of 1960 [91]; since then, many different bifacial architectures have been proposed, like polycrystalline silicon [92] [93], dye-sensitized devices [94], perovskite thin-films [95], SnS solar cells [96] and kesterite-based structures [97]. Table 4.1 [98] reports an overview of many different BFSC technologies.

Description	Concentration (Sun)	Efficiency (front or front/rear)
Buried[a] (independently confirmed)	1	21.9
Fz-Si p-type triode structure (independently confirmed)	1	21.3/19.8
Fz-Si (a-Si:H rear surface passivation) (independently confirmed)	1	20.1
Fz-Si (independently confirmed)	1	19.4/16.5
Fz-Si symmetrical (independently confirmed)	1	18.4/18.1
MISIL (independently confirmed)	1	17.1
Flexible c-Si (thickness: 110 μm, AM0)[a] (independently confirmed)	1	14.7
CdTe (Cu_xTe back contact, 40–60% transmission) (independently confirmed)	1	13.9
Si-HJT cell on commercial CZ c-Si 6" wafer using busbar-less front side metallization	1	23.14
GaAs thin film (thickness: 5 μm)	1	22.6/12.9
Zebra (n-type c-Si)	1	21.3
nPERT	1	20.63
n-type HIT screen printed	1	20.2
Sliver® solar cells	1	19.4
Remote plasma CVD		> 18/ > 18
(ITO)/(p^+nn^+)Cz-Si/(IFO) Cu contact 25 × 25 mm^2	3	17.9/17.0
(ITO)/(p^+nn^+)Cz-Si/(IFO) Cu contact 25x25 mm^2	1	17.6/16.7
Cz-Si p-type SiNx PECVD and screen printed, industrial process	1	16.6/12.8
p^+nn^{+a}	7	16.5/13.6
p^+nn^{+a}	1	15.7/13.6
GaAs thin film (thickness: 1.5 μm, AM0)	1	15.4
CIGS	1	15.2
POWER cell (16% transparency)	1	12.9
CdTe/CdS (ITO back contact)	1	10.3/2.1
Flexible dye-sensitized (if 90° bending: −6%)	1	6.8
Dye-sensitized (Ti foil based flexible)	1	6.55/4.79
Dye-sensitized (polypyrrole counter electrode)	1	5.74/3.06
Ultra-thin CdTe (0.68 μm)	1	5.7/5.0
Solid-state dye-sensitized solar cell (tandem – no color distortion)	1	3.3
Organic (50% transparency)	1	3.24
Simulated n-type HIT		27.02

[a] Not under standard test conditions.

Table 4.1: Bifacial solar cell technologies and their maximum efficiency. Data are taken from [98].

The most studied and used material for BF application is silicon. However, predicted market-share increase [99] and possible promising outcomes, such as advancements in different PV architectures like tandem solar cells, favored the realization of several different technologies reported in table 4.1.

Given that a BFSC absorbs light simultaneously from the front and the back surface, it is necessary to define a standard method to measure the power conversion efficiency but, at this time, there is not a prevalent way accepted by the scientific community. Indeed, literature reports several different approaches to define the conversion efficiency of a bifacial device [98]. The simplest way is to separately reports the efficiencies obtained illuminating only the front or the back surface, as it is done in table 4.1. Another possibility is to use the "bifaciality factor", which is defined as the ratio between the independent illuminations of the front and the back side

$$\text{Bifaciality factor } (\%) = \left(\frac{\text{front efficiency}}{\text{back efficiency}}\right) \cdot 100$$

However, there are other approaches proposed for determining the actual bifacial performance when a BFSC is illuminated from both sides at the same time. For example:

- "Separation rate": it is based on the short-circuit current density of the solar cell, which is not influenced by external resistance and is proportional to the incident light intensity [100], according to the definition:

$$Separation\ rate\ (\%) = \left(\frac{J_{SC\ front+rear}}{J_{SC\ front} + J_{SC\ rear}}\right) \cdot 100$$

- "Absolute bifacial influence": the difference Δ of any photovoltaic parameter (x) of the bifacial solar cell: $\Delta x = x_{front+rear} - (x_{front} + x_{rear})$, as reported in [98]

- "Equivalent efficiency": the efficiency possessed by a standard solar cell capable of generating the same power density as the bifacial cell under the same test conditions [101].

In this thesis, all efficiencies under bifacial illumination are expressed as "equivalent efficiencies". The geometry of the experimental setup used to conduct bifacial measurements is reported in figure 4.2: a concave glass mirror is used to reflect the light on the back of the device.

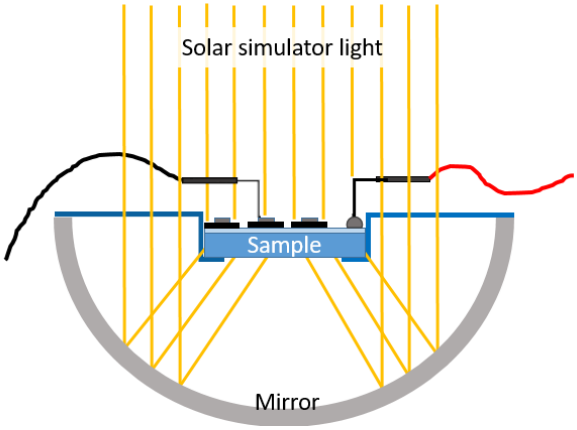

Figure 4.2: Geometry of bifacial illumination of a BFSC.

In order to precisely calibrate the light reflected from the mirror at an irradiance of 1 sun, the following method was used: i) the short-circuit current density is first measured illuminating only the front side, as the back side is covered by a black surface; ii) the cell is then turned upside down so that the front side now faces the light from the mirror; iii) the experimental setup is adjusted until the J_{sc} is equal to the previous one. This procedure ensures that both sides of the device are illuminated with an irradiance of 1 sun.

4.1.2. CIGS-based bifacial solar cells

Among various possible absorber materials, CIGS is the ideal candidate to be used in a BFSC thanks to its high PV conversion efficiency and light absorption coefficient. In fact, it is even possible to deposit few nanometers of CIGS for constructing a semi-transparent BFSC with potential application in BIPV. A standard CIGS-based BFSC is realized by substituting the opaque, metallic back contact with a TCO. The

choice of the material is crucial, since CIGS is an intrinsically p-doped material: a good electrical contact can be obtained either using a p-type TCO or a highly doped (carrier density > 10^{20} cm^{-3}) n-type TCO acting essentially as a metal. In the latter case, a tunnel junction at the interface CIGS/TCO is formed which must be electrically optimized to have an efficient carrier transit. Literature already reports CIGS-based BFSC grown on Fluorine-doped Tin Oxide (FTO) SnO_2:F [102] or Indium-Tin Oxide (ITO) In_2O_3:Sn [103] thanks to the formation of good ohmic CIGS/FTO and CIGS/ITO contacts at temperatures up to 500°C, and the PV efficiencies of these devices exceeds 15%. Unfortunately, when CIGS is deposited via conventional techniques at T > 550°C the structural and electrical properties of the TCO back contact tend to deteriorate affecting the overall BFSC performances. A possible solution to this problem relies on the deposition of a thin film of molybdenum between CIGS and TCO, which in turns lowers the back contact transmittance [104]. The situation is particularly critical in the case of CIGS deposited onto Aluminum-doped Zinc Oxide (AZO) ZnO:Al: at T>500°C gallium migrate towards the interface CIGS/TCO where it combines with oxygen forming a thin layer of gallium oxide. This material acts as an insulating barrier for electrons and strongly reduces the solar cell performances (in particular its short- circuit current) resulting in low-yield devices. For this reason, literature reports good CIGS/AZO ohmic contacts only in the presence of the thin Mo layer [105] and the high temperature growth of CIGS also imposes a limit on other substrate types for BFSC like flexible polymers (PET) or ultrathin glasses. As a conclusion, a low temperature deposition of CIGS would open new ways for both improvement of the CIGS/TCO interface and substrate preservation.

4.2 CIGS/TCO interface simulations

The deposition of CIGS, which is an intrinsically p-type semiconductor, on a heavily doped n-type TCO requires the formation of a tunnel junction. For this reason, a preliminary simulation was carried out to study carrier transport at the interface CIGS/TCO. Simulations were realized using a one-dimensional solar devices simulator called wxAMPS [106] and a two-dimensional software named Sentaurus [107]. Materials' physical parameters employed for the simulation are reported in table 4.2. The TCO taken for this simulation is a general ZnO layer (which well approximates AZO, INZO or GAZO) with no interface states.

Parameter	CIGS	TCO
Permittivity	13.6	9
Energy gap (eV)	1.17	3.4
Electron affinity (eV)	4.5	4.4
Density of states in CB (cm^{-3})	$2.2 \cdot 10^{18}$	$2.2 \cdot 10^{18}$
Density of states in VB (cm^{-3})	$1.8 \cdot 10^{19}$	$1.8 \cdot 10^{19}$
Electron mobility ($cm^2/V \cdot s$)	100	30
Hole mobility ($cm^2/V \cdot s$)	10	10

Table 4.2: Constant parameters of the simulated CIGS/TCO structure.

The most important parameter is the doping of both materials: CIGS hole concentration was varied between 10^{18} cm^{-3} and 10^{20} cm^{-3} and TCO n-doping between 10^{18} cm^{-3} and $5 \cdot 10^{20}$ cm^{-3}. The energy band under short circuit conditions at the interface was calculated for every possible combination of dopings to find out which conditions ensures a sufficiently small barrier thickness. As figure 4.3 indicates, for a n-type TCO with a doping of $5 \cdot 10^{20}$ cm^{-3} the thickness of the interface barrier increases from about 10 nm to several tens of nanometers as the free-hole density in CIGS decreases from $1 \cdot 10^{19}$ cm^{-3} to $1 \cdot 10^{18}$ cm^{-3}. In this situation, the barrier thickness is compatible with a significant tunneling of the junction current. It is worth noting that the required n-doping in the TCO is very similar to the case of FTO reference discussed in 3.3. As expected, the TCO behaves essentially as a metal since the Fermi level lies inside its conduction band.

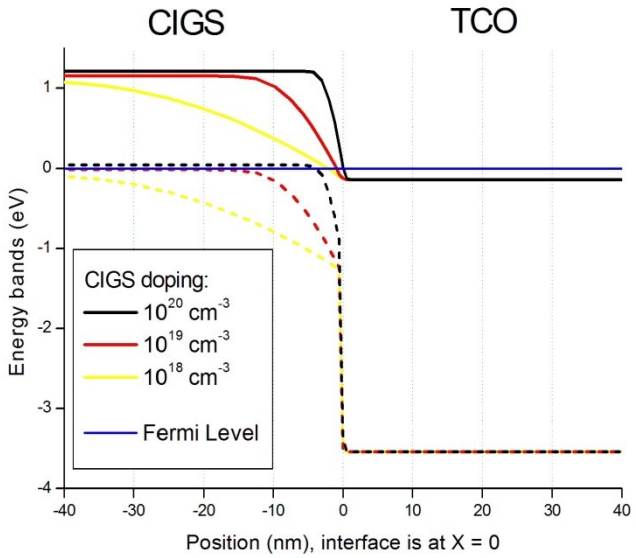

Figure 4.3: Simulated energy bands at CIGS/TCO ($n=5 \cdot 10^{20}$ cm^{-3}) interface. Solid lines are conduction bands, dotted lines are valence bands. Different colors refer to different CIGS dopings, as indicated in the inset.

In practice, the required high local p-doping in our CIGS is supplied by the thin layer of NaF deposited between the absorber and the back contact: due to the low temperature deposition of CIGS, a large fraction of the sodium contained in NaF remains located near the interface CIGS/AZO and raises the free hole density in CIGS. Assuming that the sodium acts as a classic extrinsic dopant and that its maximum incorporation in CIGS is of the order of 0.1 at% [108] then the local p-doping in CIGS is of the order of $1 \cdot 10^{19}$ cm^{-3}. For this reason, the optimization of the NaF interlayer is crucial for each different TCO to be used as a substrate in a LTPED-grown bifacial cell.

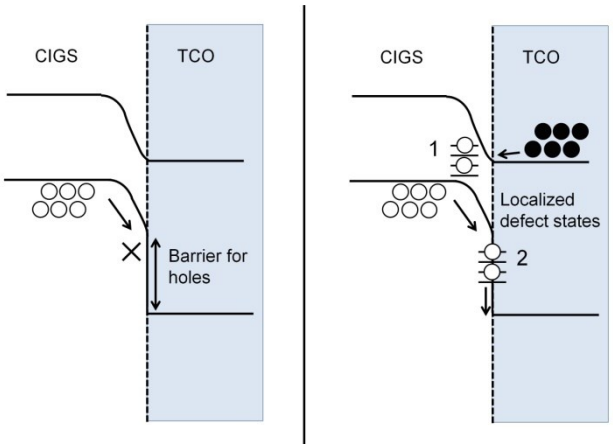

Figure 4.4: Band diagram of CIGS/TCO interface without (left) and with (right) localized defect states. White circles represent holes, black circles represent electrons. In right section arrows represents possible defect-mediated tunneling processes.

In addition, the presence of defect states at the interface CIGS/TCO has a probable influence on the carrier transport at the junction. As figure 4.4 shows, in absence of any defect state the photogenerated holes in CIGS have to cross a relatively high energy barrier (about 2.5 eV) before reaching the valence band of the TCO. The situation is rather different in the presence of localized defect states: depending on their energy and space distribution, the prevailing effect can be either trap-assisted recombination (case 1) [109] or defect-enhanced tunneling (case 2) [110]. It is very likely that the actual type and density of defect distributions are related both to the quality of the CIGS/TCO interface and to the growth technique, with LTPED being significantly different with respect to co-evaporation or sputtering. The complete understanding of the defect formation mechanisms at this interface still requires more work. The simulated J-V curve of the CIGS/TCO interface containing the two possible state distributions is reported in figure 4.5.

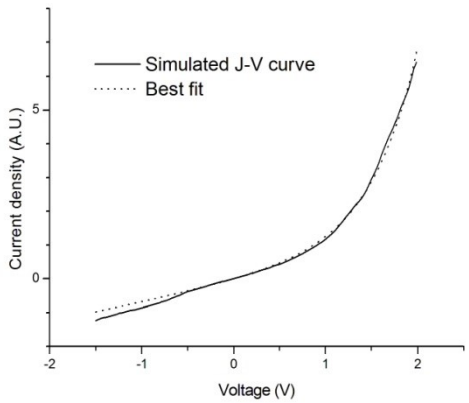

Figure 4.5: Simulated J-V curve of CIGS/TCO interface and fit with a model employing a linear and an exponential contribution.

This curve possesses two distinct trends: in the typical working range of a solar cell (between -1V and 1V) it has a quasi-ohmic behavior, while at higher voltages non-linear effects prevails; the curve can thus be fitted using a function containing a linear term (ohmic contribution) and an exponential term (thermionic emission above the barrier). To summarize, at the interface CIGS/TCO the transport mechanism is likely to be dominated by carrier tunneling through the barrier at low voltages, resulting in an ohmic-like behavior in the usual working range of a solar cell.

4.3 Electrical contact CIGS/TCO

Following the indications obtained by the simulation discussed in the previous paragraph, the studied TCOs were optimized to realize good low-resistivity contacts when coupled with CIGS in a BFSC.

The transport characteristics of the CIGS/TCO interface were investigated by preparing appropriate Au/CIGS/NaF/TCO/glass test structures (reported in figure 4.6), one for each different TCO. The Au top contact ensures a negligible contact resistance with CIGS. The sheet resistance R□ of the back contact must be as low as possible to have a working device with good efficiency. It was found that it is necessary to deposit around 300 nm of ITO and up to 800 nm of AZO5 or GAZO2 to realize a thin film with R□ < 7 Ω□ which is the average value of R□ for the commercial FTO films used as reference.

Unfortunately, the characteristic of the CIGS/GAZO2 junction could not be measured. An attempt was made to remove by chemical etching the uppermost layers of the cell described in 4.4.2 in order to expose the CIGS surface and study CIGS/GAZO2 electrical contact but it did not provide reliable results. On the contrary, as can be seen from figure 4.7, both CIGS/ITO and CIGS/AZO5 possess a low-resistivity contact with a linear J-V characteristic at low voltages (between -1V and 1V) and essentially behave as ohmic-like junctions. Linear interpolation between -1V and 1V gives the following contact resistances: $R_{CIGS/ITO}$ = 0.11 Ω·cm^2 and $R_{CIGS/AZO5}$ = 1.07 Ω·cm^2. In this latter case, the whole measurement conducted between -1.5V and 2V shows good agreement with results predicted by the theoretical simulation (see figure 4.5): the trend is linear in the typical working range of a solar cell and rectification prevails only at higher voltages.

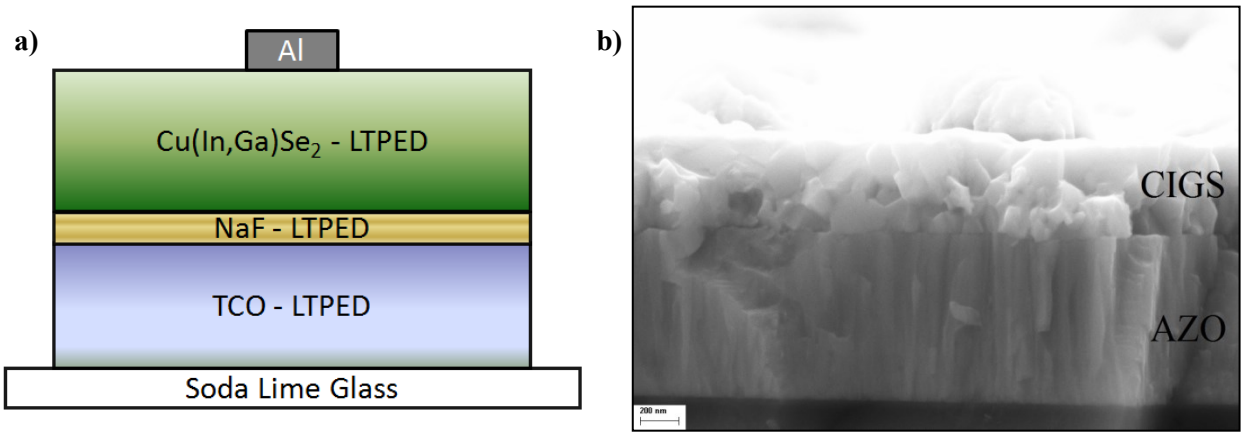

Figure 4.6: schematic (a) and SEM-FIB picture (b) of Au/CIGS/NaF/TCO structure used for ohmicity measurements.

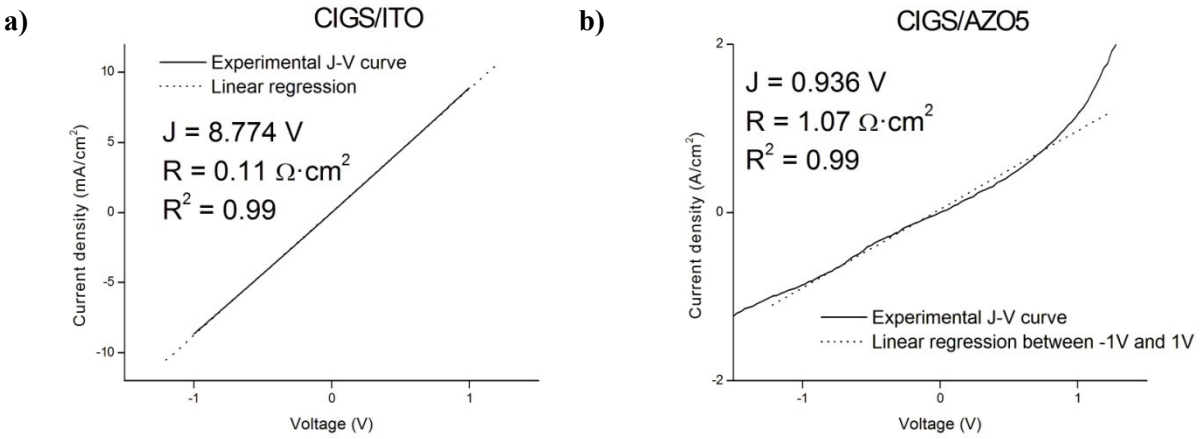

Figure 4.7: J-V curves of CIGS/ITO (a) and CIGS/AZO5 (b) structures.

The measured trend using AZO as back contact (figure 4.7(b)) is opposite to what it is reported in literature when CIGS is deposited at temperatures above 550°C[102]: this high T induces the formation of gallium oxide between CIGS and AZO, which was found to be the main cause of the poor performance of the CIGS/AZO electrical contact. In light of our results, one can assume that no Ga_2O_3 is formed when depositing both CIGS and back contact TCO via LTPED resulting in good ohmic-like junctions. SIMS and Raman measurements reported in 4.4.3 support this conclusion.

4.4 CIGS-based bifacial solar cells

The typical structure of a CIGS-based BFSC is reported in figure 4.8, where the back contact of molybdenum has been replaced by a TCO. As already mentioned, the TCO can be FTO (commercial), ITO, AZO5 or GAZO2 deposited via LTPED with an appropriate thickness. The final devices have a squared shape of 25mm x 25mm and the surface is later mechanically scribed into smaller test devices, each one with an active area ranging from 0.01 cm^2 to 0.04 cm^2.

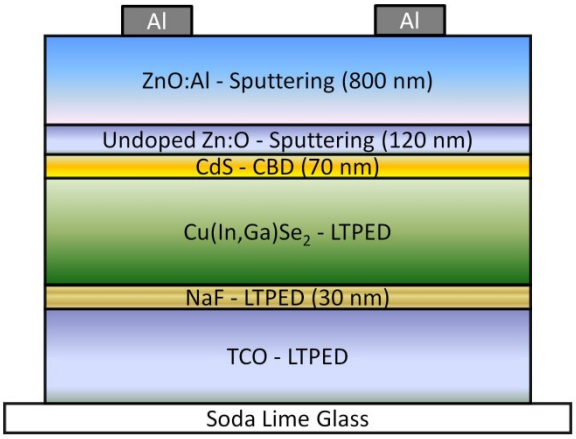

Figure 4.8: Schematic of a CIGS-based bifacial solar cell.

CIGS was deposited with two different compositions: 1) a standard GGI of 37.5% or 2) a GGI value of 20%. The first case is the GGI value that ensures the highest photovoltaic efficiency of CIGS-based solar cells deposited via LTPED. Regarding the second composition, previous results discussed elsewhere [13] already showed good performances of CIGS/ITO cells with a GGI of 37.5% and ITO deposited by sputtering, so in this thesis work we used a different composition with the intent of increasing the photogenerated current at the expenses of a moderate reduction of the open circuit voltage. No intentional gallium grading was introduced during deposition, and the CIGS thickness was either 1200 nm or 1800 nm: a smaller layer of CIGS allows to increase the short circuit current under back illumination, while a thicker CIGS is used in preliminary investigations of the device's properties using a different substrate than molybdenum.

4.4.1 BFSC with fluorine tin oxide back contact (reference)

As already introduced, a CIGS-based BFSC deposited on commercial FTO expressed a photovoltaic conversion efficiency comparable to that of an identical cell grown on molybdenum, as reported in table 4.3. This is the reason that made us assume FTO as standard reference for optimizing LTPED-deposited TCO.

Substrate	FTO			Mo
Illumination	front	back	bifacial	front
Voc (V)	652	537	637	659
Jsc (mA/cm^2)	30.8	8.6	37.8	30.4
FF (%)	73.3	55.1	69.4	73.5
Efficiency (%)	14.7	2.5	16.9	14.7
Rs (Ω·cm^2)	1.2			< 1
Rsh(Ω·cm^2)	900			~1000

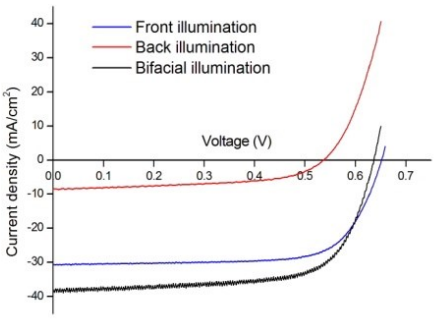

Electrical characterization of CIGS-based solar cells grown on FTO and Mo back contacts [13] (table 4.3) and J-V curves of CIGS/FTO structure under different illumination modes (figure 4.9).

It is worth noting that the efficiency obtained under front illumination using FTO as back contact is higher than the one reported in literature for an identical structure [104]. The almost identical values of FF clearly indicate that the sodium doping, which was previously optimized for molybdenum substrates, works efficiently in case of FTO, too.

4.4.2 Gallium-doped zinc oxide

A thin film of 700 nm GAZO2 deposited on glass via LTPED was used as a substrate for the CIGS/GAZO2 device. Unfortunately, despite the excellent optical and electrical properties of the back TCO, CIGS solar cells grown on GAZO2 show only a limited photovoltaic efficiency.

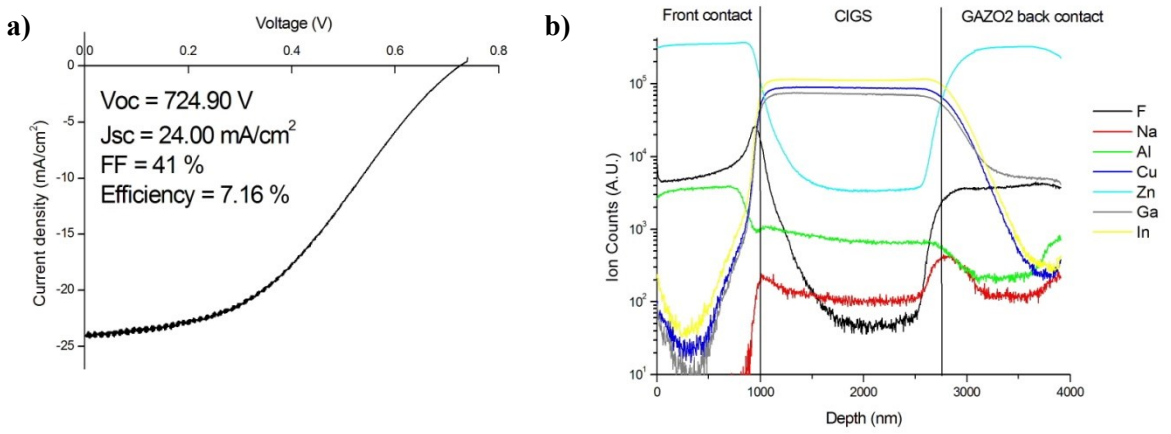

Figure 4.10: Electrical characterization and J-V curve of CIGS-based solar cells grown on GAZO2 (a) and SIMS measurement on the same device (b).

Both J-V curve and electrical characterization (figure 4.10(a)) point out that the low FF is responsible for the low performance and that it originates from a high series resistance with an average value obtained under no illumination around 25 $\Omega \cdot cm^2$. This high value is explained assuming that the interface CIGS/GAZO2 possesses a high resistivity possibly due to the formation of a thin layer of gallium oxide, similar to the case of CIGS deposited at high temperatures [104] on AZO. Therefore, SIMS measurement were performed in order to assess the possible presence of Ga_2O_3 (figure 4.10(b)). However, no Ga peaks were found at the back junction. This is a first experimental confirmation of the assumption made in 5.3: thanks to the LTPED process no gallium oxide is formed when CIGS is deposited on GAZO2 and no Ga accumulation is detected at the interface. This result rules out Ga_2O_3 as the responsible for the high series resistance observed in our sample and requires a different explanation.

Results presented in this thesis are in agreement with a recent publication of CIGS grown on GAZO back contact [111] where, contrary to the structure described above, GAZO is deposited on a thin layer of Mo to improve its current spreading and capped with MoN to prevent the formation of gallium oxide at the interface with CIGS. Although the overall PV efficiency is fairly lower than the one obtained in this thesis (4.12%), the reported J-V curves and FF are similar to those of figure 4.10. Considering that no Ga_2O_3 is found by SIMS measurements, we tend to agree with the authors of that publication that the low work function of gallium oxide [112] is responsible for the presence of a barrier at the interface CIGS/GAZO. We must however remember that there are differences between this thesis' devices and those of [111], therefore further work is needed to confirm that this explanation is definitely valid also in our solar cells grown on GAZO back contact. Nevertheless, the LTPED process produces materials with better quality and electrical properties, resulting in a CIGS/GAZO2 solar cell with a photovoltaic conversion exceeding the values reported in literature until now.

4.4.3 Aluminum-doped Zinc Oxide

CIGS/AZO5 devices were fabricated on an AZO5 thin film with a typical thickness of 700 nm. The electrical properties of the best solar cell obtained under different illumination modes are reported in table 4.4.

Our best result				Literature
Illumination	front	back	bifacial	front
Voc (V)	635.38	574.50	586.12	267
Jsc (mA/cm^2)	26.89	16.30	43.14	0.45
FF (%)	54.4	54.0	45.9	26.9
Efficiency (%)	9.30	5.06	11.60	0.04
Rs (Ω·cm^2)	0.26			
Rsh(Ω·cm^2)	905.00			

Table 4.4: Electrical characterization of CIGS-based solar cells grown on AZO5 back contacts and comparison with best literature data [104].

To the best of our knowledge, the efficiency under front side illumination (9.3%) and overall bifacial illumination (11.6%) are the highest reported in literature [113]. Indeed, we managed to realize a working CIGS-based BFSC on AZO thanks to the LTPED process which inhibits the formation of gallium oxide at the CIGS/back contact interface. It is worth noting that both the open circuit voltage and the short circuit current are very close to the typical values obtained in LTPED-grown cells on molybdenum back contacts [10] at IMEM-CNR.

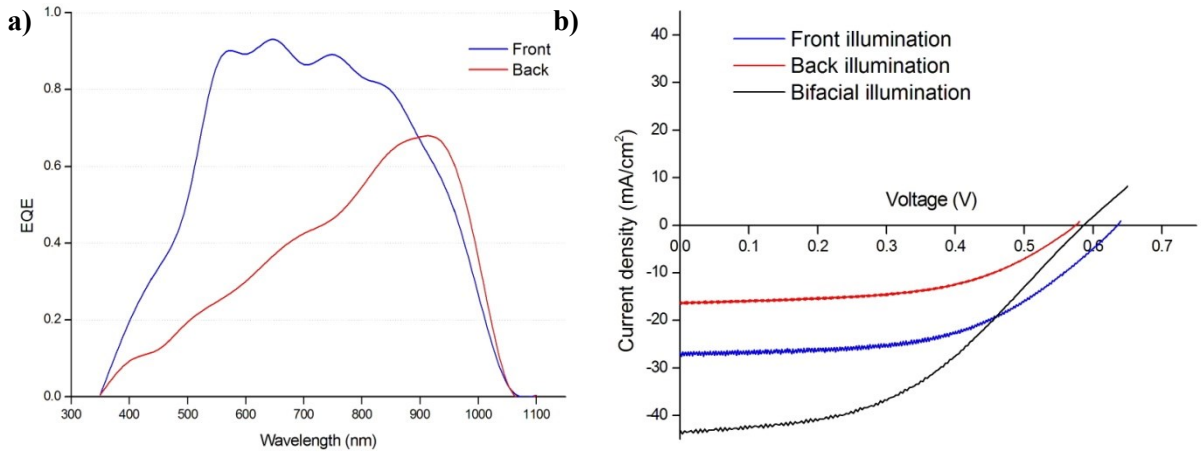

Figure 4.11: EQE measurements (a) and J-V curves (b) of CIGS/AZO5 structure under different illumination modes.

Figure 4.11(a) reports EQE measurement on this device under front and back illumination. The curve possesses the typical behavior of a BFSC: under back illumination, the EQE has a peak in the infrared region because the fraction of carriers generated towards the space-charge region increases with increasing

wavelength [114]. The rapid decrease of the collection efficiency with decreasing wavelength is due to the low carrier mobility in the neutral region of the cell. This consideration indicates that a reduction of the CIGS thickness would increase the short circuit current under back illumination, but previous experimental results [13] obtained on CIGS-based BFSC deposited on sputtered TCO have demonstrated that the effect is balanced by a reduction in Jsc under front illumination due to a smaller fraction of sunlight being absorbed from the cell. We found that a CIGS thickness of 1200 nm is the best compromise.

The J-V curves in figure 4.11(b) are affected by the relatively low value of FF compared to the standard CIGS solar cells obtained both on molybdenum or on FTO, and this feature seems to be a common issue of all CIGS/AZO cells reported so far in literature [89]. Therefore, the lack of Ga_2O_3 at the junction between the absorber and the back TCO is a necessary but not sufficient condition for the optimization of the carrier transport along this particular structure. Actually, the absence of gallium oxide was confirmed by SIMS and Raman measurements.

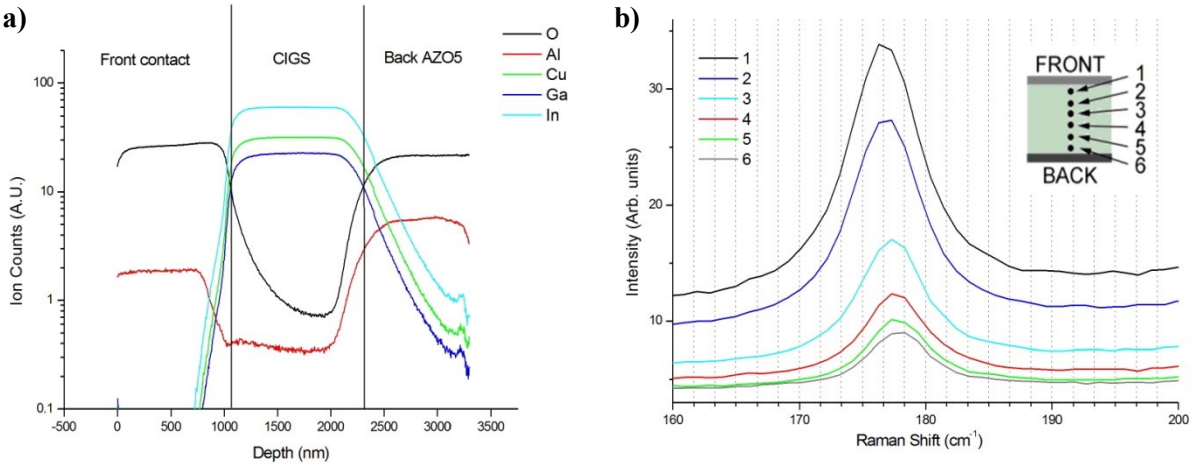

Figure 4.12: SIMS (a) and normalized Raman measurements (b) of CIGS/AZO5 structure.

In fact, figure 4.12(a) reports no peak in the trend of gallium and oxygen at the CIGS/AZO5 interface while figure 4.12(b) does not show any Raman peak related to Ga_2O_3 near the back interface (curve 6). Interestingly, there is a clear peak-shift of the A1 vibrational mode of CIGS when analyzing the structure along the growth direction (moving from the buffer layer, curve 1, to the back contact, curve 6). As suggested in previous reports [75], the position of this peak is directly related to the gallium content of the CIGS sample: the peak shifts linearly from 174 cm^{-1} for CIS to 184 cm^{-1} for CGS. As a result, the shift reported in figure 4.12(b) correspond to an estimated GGI variation of about 11% and indicates that the gallium concentration is greater near the interface with the back contact. This means that an unintentional grading of the absorber's composition formed spontaneously along the growth axis during the deposition. A similar effect was observed also for CIGS-based BFSC deposited on ITO back contacts [115] and therefore it is probably a specific feature of the LTPED deposition of CIGS which deserves further investigations. SIMS measurement is unable to confirm this compositional gradient, as the smallest size of the craters produced by

the sputtering beam is much larger than the typical scale of thickness variation associated to the roughness of the CIGS film and this prevents any significant quantitative assessments due to memory effects. The excellent ohmic behavior of CIGS/AZO electrical contact and the SIMS results would confirm that no continuous Ga_2O_3 insulating layer forms at the interface between absorber and TOCO, although the presence of isolated islands of Ga_2O_3 with thickness below interface roughness cannot be excluded. The main results obtained on the CIGS/AZO5 junction (simulation of interface, ohmicity of interface and realization of the BFSC) prove that AZO5 can be used as an indium-free and non-toxic alternative to ITO or FTO in bifacial solar cells. These results were recently published in a specific article [87].

4.4.4 Indium Tin Oxide

The average thickness of ITO films used as back contacts in CIGS-based BFSC was 300 nm and solar devices were realized with a GGI = 0.2 in CIGS. Table 4.5 contains the best electrical parameters of PED-deposited ITO, sputtered ITO and literature reference.

ITO-PED			ITO-sputtering [13]	Literature [104]
Illumination	front	back	front	front
Voc (V)	580.05	402.44	641	651
Jsc (mA/cm^2)	35.83	3.84	29.9	34.4
FF (%)	72.0	35.8	61.5	68.2
Efficiency (%)	14.96	0.55	11.8	15.2
Rs (Ω·cm^2)	0.60		1.3	
Rsh(Ω·cm^2)	415		710	

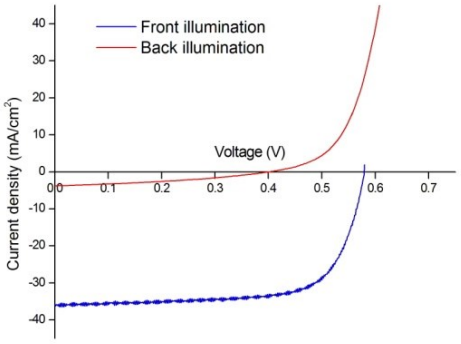

Electrical characterization of CIGS-based solar cells grown on PED-deposited ITO back contacts and comparison with best literature data [104] and sputtered ITO [13] (table 4.5); J-V curves of CIGS/PED-ITO BFSC (figure 4.13).

The results achieved on the structure CIGS/ITO are comparable or superior, in case of Jsc and FF, to the best literature data. It is important to underline that the greater Voc reported by literature corresponds to a graded CIGS. Nevertheless, we managed to reach an efficiency under front illumination only 0.2% lower than literature data thanks to the high quality of materials deposited via LTPED and of the CIGS/ITO junction without applying any gallium grading or other technological improvements.

As already mentioned, CIGS composition was different in samples deposited on sputtered ITO (GGI = 0.37) and PED-deposited ITO (GGI = 0.2). Reducing the gallium content in CIGS has the effect of lowering the energy gap and consequently shifting the absorption edge towards higher wavelengths. This turns out in a net improvement of the photogenerated current at the cost of a reduction of Voc. Considering that in a BFSC the

back TCO has a relatively high R□, we exploited this approach to minimize the reduction of Jsc due to losses in the back contact by increasing the net current generated by the device.

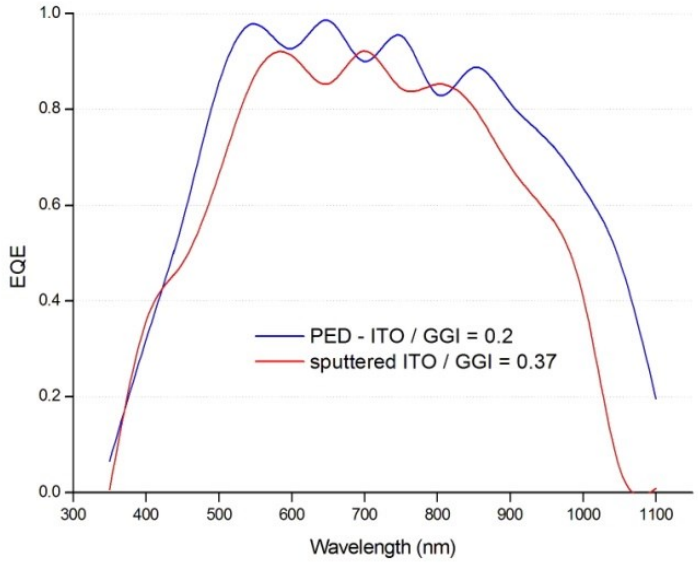

Figure 4.13: EQE of CIGS-based BFSC with different GGI in CIGS.

Figure 4.13 reports EQE measurements of the two samples deposited with different GGI and substrates, where it is evident that the cell with GGI = 0.2 has higher absorption at high wavelength. In addition, the increased absorption between 400nm and 500nm is due to the enhancements in CdS deposition reported in 1.5.4. Under front illumination, the cumulative effect of these two features and the overall optimization of CIGS/ITO junction increased the device's efficiency from 10.90% to a remarkable 14.96% and the FF from 61% to 72%, comparable to the reference values obtained with FTO and Mo back contacts.

4.5 Large-area BFSCs

Despite the great efforts aimed at improving the TCO, the electrical resistivity of ITO and AZO5 does not go below $3.17 \cdot 10^{-4}$ Ω·cm and $1.92 \cdot 10^{-4}$ Ω·cm, respectively. These values are 40-50 times bigger than the typical resistivity of molybdenum ($5.31 \cdot 10^{-6}$ Ω·cm) and introduce a major problem in the perspective of developing large-area BFSCs. In fact, all results presented in the previous section are very promising but obtained on a small active region, usually around 0.02-0.03 cm^2 (the standard area of a test device scribed on the surface of a deposited sample). With such small area the series resistance of the back contact is negligible. On the contrary, on larger areas the back TCO Rs becomes dominant and significantly reduces the generated current and the FF value.

For a more quantitative assessment, the problem can be simulated considering two ideal CIGS-based BFSCs deposited on two TCO, one with a R□ = 1 Ω□ and the other with R□ = 7 Ω□. The former value is an estimation in excess of the typical R□ of Mo substrates, while the latter value is selected because the FTO

thin film reference exhibits an average sheet resistance of 7 Ω□. With these hypotheses, one cm^2 area back contacts would possess a series resistance of, respectively, Rs = 1 $\Omega \cdot cm^2$ and Rs = 7 $\Omega \cdot cm^2$. Results of simulations indicate that the increase of Rs has a considerable impact on the device's electrical performances: the FF drops from 76% to 51% and the J-V curve differs considerably from the ideal case, as reported in figure 4.14.

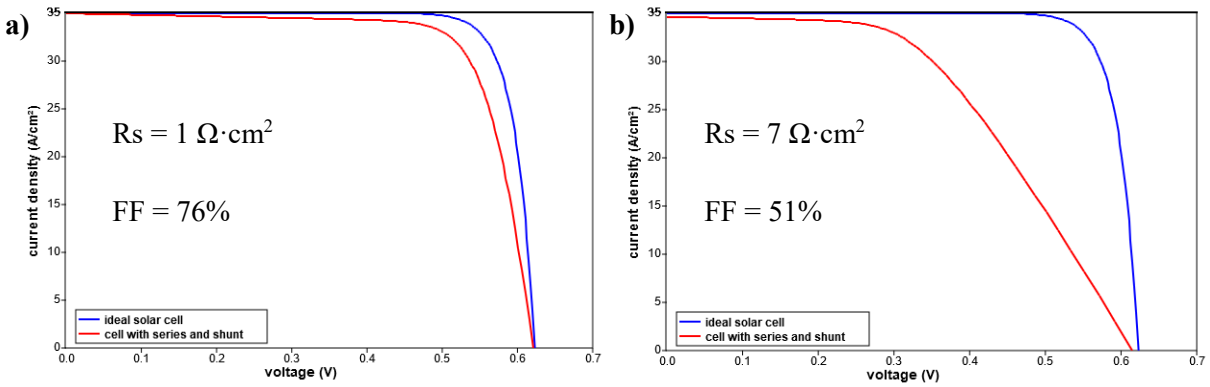

Figure 4.14: Simulated J-V curves of a solar cell with Rs = 1 Ω·cm² (a) and 7 Ω·cm² (b). Rsh is set at 1000 Ω·cm².

From these results, it is evident that the realization of a large area CIGS-based BFSC necessarily requires to drastically reduce the back contact series resistance. Hence, in this section we propose an innovative solution to this problem.

In order to limit the TCO's series resistance, we modified the deposition process by forming a metallic grid on the glass substrate prior to deposition of the back TCO. The geometrical pattern of the metal grid allows a more efficient drain of the photo-generated carriers, thus reducing the power loss, while minimizing the shading effects. In practice, the presence of this grid should diminish the effective R□ of the back contact and should also permit the deposition of a thinner TCO with potential benefits on the transmittance. The schematic cross section of a BFSC employing this novel idea and an actual picture of a substrate with a metallic grid are depicted in figure 4.15.

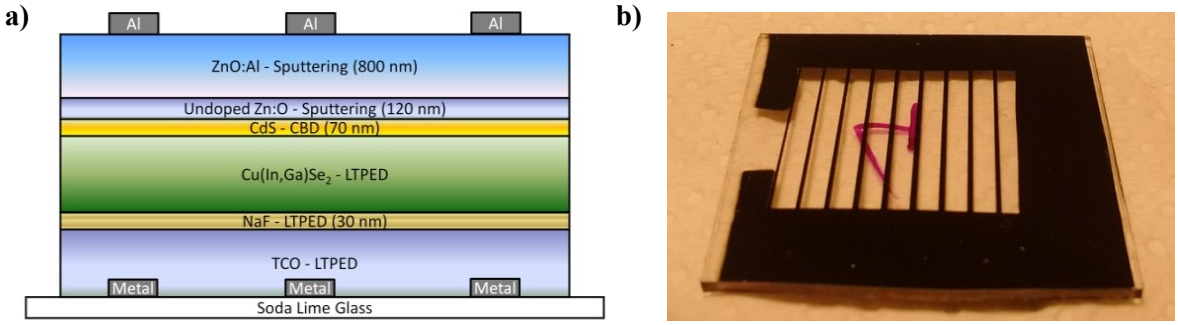

Figure 4.15: structure of BFSC deposited on a substrate with a metallic grid (a) and picture of a substrate used for preliminary depositions (b).

Of course, it is necessary to find an optimal metal for the metallic grid and the best TCO as back contact. Initial experiments were made with aluminum (being low cost and already used in the metallic contacts on the front TCO) or molybdenum (the standard substrate for CIGS-based solar cells) and ITO as back contact, in view of its excellent results discussed in the previous section. A future work perspective will deal with the substitution of ITO with AZO5, the low-cost and no-toxic alternative to ITO. Molybdenum metallic grids were fabricated by sputtering in collaboration with UNIPR while aluminum grids were sputtered at IMEM-CNR.

The device realized on the aluminum metallic grid does not show any photovoltaic behavior, as indicated by figure 5.16-a. A possible explanation can be inferred from Raman measurements realized on this sample, reported in figure 5.16-b and 5.16-c.

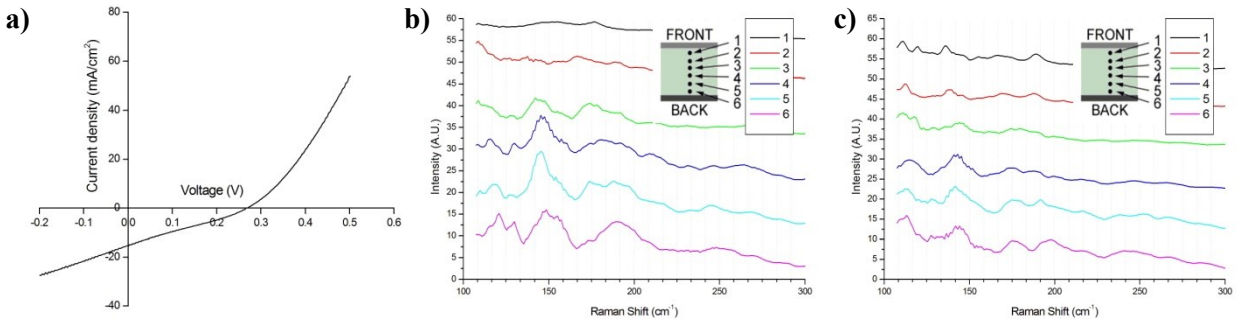

Figure 4.16: J-V curve (a) and Raman spectra of CIGS/AZO/Mo-grid sample measured on the metallic grid (b) and between grid lines (c).

In both cases, the A1 vibrational mode of CIGS is absent and a new peak is present with a Raman shift of 141 cm^{-1} in measurement conducted near the CIGS/AZO interface. This peak can be attributed to the presence of $Cu(In,Al)Se_2$ [116] especially in the film above the metallic grid (figure 4.16(b), curve 5 and 6). This result indicates that aluminum has migrated from the metallic grid into CIGS and has modified its local composition forming $Cu(In_{1-x},Al_x)Se_2$ with an effective value of x varying in different positions in the sample. The Al migration has probably occurred during the substrate heating required for CIGS deposition. Increasing the thickness of the TCO above the metallic grid does not reduce this phenomenon, therefore aluminum is not suited to be used in the metallic grid.

On the contrary, the cell realized on molybdenum metallic grid + ITO templates showed very promising results. Table 4.6 compares electrical parameters of the best device realized on pure ITO and ITO-on-Mo grid.

Substrate	ITO	ITO on Mo grid
Area (cm^2)	**0.02**	**0.068**
Voc (V)	580	572
Jsc (mA/cm^2)	35.61	35.59
FF (%)	72	68
Efficiency	14.96	13.69
Rs ($\Omega \cdot cm^2$)	**0.6**	**0.5**
Rsh ($\Omega \cdot cm^2$)	415	1554

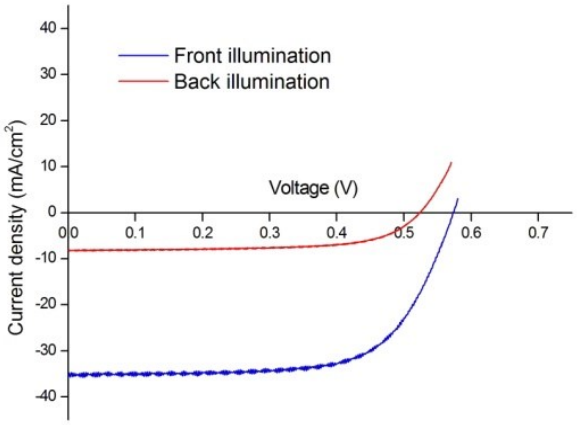

Best photovoltaic parameters of BFSC realized on ITO and ITO on Mo grid (table 4.6) and J-V curves of CIGS/ITO/Mo grid structure (figure 4.17).

The most important preliminary result is that the total active area of the cell has increased about 3.5 times maintaining the series resistance constant; the efficiency of this preliminary device (13.69 %) is only 1% lower than the best sample deposited on ITO. In addition, the higher Rsh is due to a surface effect: the mechanical scribing of the surface leads to the formation of shunt paths in the edge of the test device, and their influence is reduced in larger areas justifying the increase of Rsh. To conclude, the metallic grid has a positive impact on both series resistance and shunt resistance and paves the way to realization of large area devices.

4.6 Conclusions

A working CIGS-based bifacial solar cell was realized on AZO as back contact and exhibits an equivalent bifacial efficiency of 11.6% under 1-sun illumination and with an absorber thickness of 1200 nm. To date, this is the highest value reported in literature for CIGS-based BFSC on AZO back contacts. This result was achieved thanks to the LTPED deposition of CIGS on AZO. In fact, the low temperature deposition of the absorber prevents the formation of unwanted Ga_2O_3 at the interface CIGS/AZO which acts as an insulating barrier and impedes the device operation. The formation of gallium oxide was previously recognized by literature to be the main cause of device misfunctioning, and the absence of Ga_2O_3 was confirmed by SIMS and Raman measurements. Furthermore, Raman spectra indicate that a spontaneous gallium concentration gradient is present in the device, probably as a characteristic feature of CIGS deposition in a highly energetic system such as PED.

CIGS-based BFSC realized on PED-deposited ITO showed photovoltaic properties comparable or even superior (FF and Jsc) to the best literature data. This result is achieved thanks to two contributions: high

quality materials and optimization of the device structure. Actually, GGI in the absorber was modified to increase the generated current counterbalancing the electrical losses of the back contact.

An architecture including a metallic grid is proposed for large area thin film BFSCs. The presence of the metallic grid ensures an ehnanced collection of the photogenerated carriers and a reduced sheet resistance of the back contact. Preliminary results indicate that the best result is obtained using ITO deposited on a molybdenum metallic grid. In this case, we realized a solar cell with performances comparable to the best CIGS/ITO sample over a 3.5 times larger area, while maintaining constant the series resistance. This is an important promising results in view of realizing larger CIGS-based BFSCs.

Conclusions and perspectives

The main result of this thesis is the obtainment of CIGS-based bifacial solar cells using LTPED-deposited AZO and ITO as back contacts. Electrical and optical optimization of both the TCOs and the CIGS/TCO interface allowed reaching such important results.

CIGS-based bifacial solar cells realized on ITO achieved excellent photovoltaic properties. To counterbalance the electrical losses occurring in the back contact, the gallium concentration in the absorber was modified to raise the current generated by the device. This resulted in a higher efficiency with respect to an identical structure realized using the standard GGI value in the absorber, pushing the efficiency under front illumination up to 14.96% and the fill factor up to 72%. To date, this efficiency is comparable to the best literature data (the fill factor is even superior to state-of-the-art device) without the implementation of gallium grading or antireflection coatings, leaving ample possibilities to further increase the performance of BFSCs deposited on ITO.

CIGS-based BFSC realized on AZO exhibited an equivalent bifacial efficiency of 11.6% under 1-sun illumination with CIGS thickness of 1200 nm. This result exceeds the values reported in literature for this type of structure. Such remarkable outcome was made possible thanks to the LTPED deposition of the absorber which prevents the formation of unwanted Ga_2O_3 at the interface CIGS/AZO. Actually, as previously reported, gallium oxide acts as an insulating barrier for photogenerated carriers causing the device to misfunction. The absence of Ga_2O_3 in the devices studied in this work was confirmed by SIMS and Raman measurements. In addition, Raman spectra indicate that a positive gallium concentration gradient is present in the absorber, probably occurring spountaneously during CIGS deposition in a highly energetic system such as LTPED. Considering that AZO is a low-cost (In-free) and no-toxic alternative to ITO or FTO, the demonstration of a CIGS-based bifacial solar cell on AZO represents a considerable step forward in the field of the building integrated photovoltaic. This device still requires to be optimized in order to reach the efficiencies of the CIGS/ITO structures; in particular, the relatively low value of the fill factor indicates that preventing the formation of gallium oxide at the CIGS/AZO interface is a necessary but not a sufficient condition for maximizing the transport properties of the cell.

A novel approach to fabrication of large-area bifacial solar cells was also proposed and tested. On big areas, the sheet resistance of the oxide back contact becomes the dominant contribution in the overall series resistance of the solar cell. To realize large-area devices, the contact resistance must therefore be minimized. The proposed approach is based on the deposition of the transparent back contact onto a glass substrate

covered by a metallic grid. The presence of this metallic grid allows a more efficient collection of the photogenerated carriers, thus drastically reducing the sheet resistance of the back contact. Preliminary experiments show that the most appreciable results are obtained by depositing CIGS/ITO stack on a molybdenum metallic grid. A device with such architecture indeed showed performances comparable to the best cell deposited on pure ITO over a 3.5 times smaller area, and the series resistance was found to be the same. This is a promising results in view of realizing larger CIGS-based BFSCs.

The results discussed above are to be primarily ascribed to the optimization of LTPED-deposited TCOs. In fact, all studied TCOs deposited at T=100°C exhibited excellent optical and electrical properties, coupled to good crystalline structure. The measured values of transmittance and specific resistivity indeed compare well with those of state-of-the-art materials grown at higher temperatures. In particular, ITO, AZO and ZnO:Ga films exhibited an average optical transmittance above 85% (between 400nm and 1200nm), a bandgap above 3.3 eV and a resistivity lower than $4 \cdot 10^{-4}$ Ω·cm, confirming that LTPED is a reproducible, reliable and low-cost process to deposit n-type conventional TCOs at low temperatures.

The results presented in this thesis confirm that CIGS-based bifacial cells deposited via LPTED are feasible. To achieve further progress in this field, one can still work on two fronts. First, it is necessary to improve the bifacial cells deposited on AZO by optimizing the transport at the CIGS/AZO interface, in order to obtain the same excellent performances that was reached with the CIGS/ITO structure. Secondly, it is crucial to identify the most suitable metal for fabrication of the metallic grid and, at the same time, to improve the deposition of AZO on the metallic grid to get a mechanically stable template for subsequent deposition of the absorber.

This would definitely pave the way to AZO as a non-toxic and cost-effective alternative to ITO.

List of publications and conference talks

Conference talks

- F. Pattini et al., CIGS Bi-Facial solar cells, presented at EMRS 2016 – spring meeting, Lille (France), 2-6 May 2016;
- N. Cavallari et al., CIGS-based thin film solar cells grown on TCO back contacts, presented at EMRS 2016 – fall meeting, Warsaw (Poland), 19-22 September 2016;
- M. Mazzer et al., Progress on Low-Temperature Pulsed Electron Deposition of CuInGaSe2 Solar Cells, presented at Materials 2016, Catania (Italy), 12-16 December 2016;
- E. Gilioli et al., Low-cost thin film solar cells for BIPV applications, it will be presented at CIMTEC 2018, Perugia (Italy), 4-14 june 2018.

Scientific Publications

- M. Mazzer et al., Progress on low-temperature pulsed electron deposition of $CuInGaSe_2$ solar cells, *Energies*, vol. 9, no. 3, pp. 1–11, 2016
- N. Cavallari et al., Low temperature deposition of bifacial CIGS solar cells on Al-doped Zinc Oxide back contacts, *Appl. Surf. Sci.*, vol. 412, pp. 52–57, 2017
- N. Cavallari et al., Progress toward large area deposition of CIGS-based bifacial solar cell, to be published

Acknowledgments

I want to express my most thoughtful thanks to all those people that helped me in very different ways to go through difficulties and successfully complete my PhD work. I begin by thanking my supervisors Dr. Edmondo Gilioli and Prof. Roberto Fornari. It is thanks to their coordinated efforts that I could join the PED-team at IMEM-CNR while maintaining collaboration and duties at the University. They were kindly supporting me all the time, especially in the final rush for submitting the thesis on time.

I wish also thank many other colleagues at IMEM-CNR: Drs. Stefano Rampino and Francesco Pattini, for their support during my working days at IMEM-CNR, Dr. Matteo Bronzoni for the deposition of CIGS in my devices, Dr. Massimo Mazzer and Dr. Enos Gombia for many fruitful discussions, Dr. Filippo Annoni for always being helpful whenever I needed a hand, Drs. Davide Calestani and Marco Villani for the advices in operating the SEM microscope, Dr. Giovanna Trevisi for helping me with electrical measurements, Giulia, Michele and Dedè for all the cheerful moments we spent together in many occasions.

Moreover, I thank my colleagues Greta, Elena and Silvia who shared their PhD experience with me and contributed to make my PhD period a less problematic with mutual support and encouragements.

Additionally, I want to thank all my friends and team members who gave me many appreciated happy moments during these years of doctoral studies: Anna, Andrea, Davide, Francesco, Federico, Ilaria, Matilde, Nicole, Silvia, Simone.

A very special thank to my mother Daniela and my aunt Adriana who have always believed in me and stood by my side, especially when I needed them mostly. The biggest thank is for my dad Massimo, who was my strongest supporter in life, and continued to be my source of encouragement and inspiration after he passed away shortly after beginning this PhD work.

References

[1] http://www.eia.gov/outlooks/archive/ieo13/.

[2] https://www.eia.gov/outlooks/ieo/exec_summ.php.

[3] United Nation. Adoption of the Paris Agreement. Conference of the Parties - 21st session. Paris : s.n., 2015.

[4] International Energy Agency (IEA): Photovoltaic Power System (PVPS) programme. IEA-PVPS Editorial 27th October 2016.

[5] International Energy Agency (IEA): 2016 Snapshot of global photovoltai markets.

[6] https://www.nrel.gov/pv/.

[7] S. R. Kodigala, *Cu(In1-xGax)Se2 Based Thin Film Solar Cells*. 2011

[8] M. Gloeckler and J. R. Sites, Band-gap grading in Cu(In,Ga)Se2 solar cells, *J. Phys. Chem. Solids*, vol. 66, no. 11, pp. 1891–1894, 2005

[9] T. Wada, N. Kohara, S. Nishiwaki, and T. Negami, Characterization of the Cu(In,Ga)Se_2/Mo interface in CIGS solar cells, *Thin Solid Films*, vol. 387, no. 1–2, pp. 118–122, 2001

[10] M. Mazzer et al., Progress on low-temperature pulsed electron deposition of $CuInGaSe_2$ solar cells, *Energies*, vol. 9, no. 3, pp. 1–11, 2016

[11] S. Rampino, M. Bronzoni, L. Colace, P. Frigeri, E. Gombia, and C. Maragliano, Low-temperature growth of single-crystal Cu(In,Ga)Se2 films by pulsed electron deposition technique, *Sol. Energy Mater. Sol. Cells*, vol. 133, pp. 82–86, 2015

[12] F. Pattini, M. Bronzoni, F. Mezzadri, F. Bissoli, E. Gilioli, and S. Rampino, Dynamics of evaporation from CuGaSe2 targets in pulsed electron deposition technique, *J. Phys. D. Appl. Phys.*, vol. 46, no. 24, p. 245101, 2013

[13] F. Annoni, Progress in photovoltaic cells based on Low-Temperature Pulsed-Electron-Deposited Cu(In,Ga)Se_2 films, 2017

[14] H. Sato, T. Minami, S. Takata, and T. Yamada, Transparent conducting p-type NiO thin films prepared by magnetron sputtering, *Thin Solid Films*, vol. 236, no. 1–2, pp. 27–31, 1993

[15] H. Kawazoe, M. Yasukawa, H. Hyodo, and M. Kurita, P-type electrical conduction in transparent thin films of $CuAlO_2$, *Nature*, vol. 389, no. 6654, pp. 939–942, 1997

[16] S. Nandy, A. Banerjee, E. Fortunato, and R. Martins, A Review on Cu_2O and Cu-Based p-Type Semiconducting Transparent Oxide Materials: Promising Candidates for New Generation Oxide Based Electronics, *Rev. Adv. Sci. Eng.*, vol. 2, no. 4, pp. 273–304, 2013

[17] H. Otha, K. Kawamura, M. Orita, M. Hirano, N. Sarukura, and H. Hosono, Current injection emission from a transparent p–n junction composed of p-$SrCu_2O_2$/n-ZnO, *Appl. Phys. Lett.*, vol. 77, no. 4, p. 475, 2000

[18] A. Kudo, H. Yanagi, Y. Yano, K. Ueda, H. Hosono, and H. Kawazoe, Fabrication of transparent p–n heterojunction thin film diodes based entirely on oxide semiconductors, *Appl. Phys. Lett.*, vol. 75, no. 18, p. 2851, 1999

[19] H. Ohta, M. Orita, and M. Hirano, abrication and characterization of ultraviolet-emitting diodes composed of transparent p-n heterojunction, p-$SrCu_2O_2$ and n-ZnO, *Appl. Phys. Lett.*, vol. 89, no. 10, p. 5720, 2001

[20] A. Renaud et al., $CuGaO_2$: a promising alternative for NiO in p-type dye solar cells, *J. Mater. Chem.*, vol. 22, no. 29, p. 14353, 2012

[21] H. Kawazoe, H. Yanagi, K. Ueda, and H. Hosono, Transparent p-Type Conducting Oxides: Design and Fabrication of p-n Heterojunctions, *MRS Bull.*, vol. 25, no. August, pp. 28–36, 2000

[22] L. Kleinman and K. Mednick, Self-consistent energy bands of Cu_20, *Phys. Rev. B*, vol. 21, no. 4, p. 1549, 1980

[23] H. Yanagi, K. Ueda, S. Ibuki, T. Hase, H. Hosono, and H. Kawazoe, Transparent p- and n-Type Conductive Oxides With Delafossite Structure, *MRS Proc.*, vol. 623, 2000

[24] P. Barquinha, R. Martins, L. Pereira, and E. Fortunato, P-Type Transparent Conductors and Semiconductors, in *Transparent Oxide Electronics*, 2012, pp. 63–100

[25] K. Ueda, T. Hase, H. Yanagi, H. Kawazoe, and H. Hosono, Epitaxial growth of transparent p-type conducting $CuGaO_2$ thin films on sapphire (001) substrates by pulsed laser deposition, *J. Appl. Phys.*, vol. 89, no. 3, p. 1790, 2001

[26] Q.-J. Liu, Z.-T. Liu, J.-C. Chen, L.-P. Feng, and H. Tian, First-principles study of structural, mechanical, electronic and optical properties of 3R- and 2H-$CuGaO_2$, *Phys. B Condens. Matter*, vol. 406, no. 18, pp. 3377–3382, 2011

[27] J. Tate et al., p-Type oxides for use in transparent diodes, *Thin Solid Films*, vol. 411, no. 1, pp. 119–124, 2002

[28] S. C. Dixon, D. O. Scanlon, C. J. Carmalt, and I. P. Parkin, n-Type doped transparent conducting binary oxides: an overview, *J. Mater. Chem. C*, vol. 4, no. 29, pp. 6946–6961, 2016

[29] A. . Katkov and A. . Lykasov, Spinel phase relations in the Fe_3O_5-$CuFe_2O_4$ system, *Inorg. Mater. Transl. from Neorg. Mater. Orig. Russ. Text*, vol. 39, no. 2, pp. 171–174, 2003

[30] D. Shishin, T. Hidayat, E. Jak, and S. A. Decterov, Critical assessment and thermodynamic modeling of the Cu-Fe-O system, *Calphad Comput. Coupling Phase Diagrams Thermochem.*, vol. 41, pp. 160–179, 2013

[31] A. P. Amrute, Z. Łodziana, C. Mondelli, F. Krumeich, and J. Pérez-Ramírez, Solid-state chemistry of cuprous delafossites: Synthesis and stability aspects, *Chem. Mater.*, vol. 25, no. 21, pp. 4423–4435, 2013

[32] Y. Kumekawa, M. Hirai, Y. Kobayashi, S. Endoh, E. Oikawa, and T. Hashimoto, Evaluation of thermodynamic and kinetic stability of $CuAlO_2$ and $CuGaO_2$, *J. Therm. Anal. Calorim.*, vol. 99, no. 1, pp. 57–63, 2010

[33] V. Varadarajan and D. P. Norton, $CuGaO_2$ thin film synthesis using hydrogen-assisted pulsed laser deposition, *Appl. Phys. A Mater. Sci. Process.*, vol. 85, no. 2, pp. 117–120, 2006

[34] M. H. A. Bakar, L. M. Li, K. A. Mohamad, S. Sulaiman, S. Salleh, and A. Alias, Effect of Annealing Temperature on $CuGaO_2$ Thin Films Deposited by RF Sputtering Technique, *J. Adv. Res. Appl. Mech.*, vol. 14, no. 1, pp. 12–17, 2015

[35] C. Bouzidi, H. Bouzouita, A. Timoumi, and B. Rezig, Fabrication and characterization of $CuAlO_2$ transparent thin films prepared by spray technique, *Mater. Sci. Eng. B Solid-State Mater. Adv. Technol.*, vol. 118, no. 1–3, pp. 259–263, 2005

[36] M. Neumann-Spallart, S. P. Pai, and R. Pinto, PLD growth of $CuAlO_2$, *Thin Solid Films*, vol. 515, no. 24 SPEC. ISS., pp. 8641–8644, 2007

[37] N. Tsuboi, T. Moriya, S. Kobayashi, H. Shimizu, K. Kato, and F. Kaneko, Characterization of $CuAlO_2$ thin films prepared on sapphire substrates by reactive sputtering and annealing, *Jpn. J. Appl. Phys.*, vol. 47, no. 1 PART 2, pp. 592–595, 2008

[38] H. Kim and C. M. Gilmore, Electrical, optical and structural properties of indium–tin–oxide thin films for organic light-emitting devices, *J. Appl. Phys.*, vol. 86, no. 11, pp. 6451–6461, 1999

[39] Z. Chen, W. Li, R. Li, Y. Zhang, G. Xu, and H. Cheng, Fabrication of highly transparent and conductive indium-tin oxide thin films with a high figure of merit via solution processing., *Langmuir*, vol. 29, pp. 13836–42, 2013

[40] J. Du et al., Highly transparent and conductive indium tin oxide thin films for solar cells grown by reactive thermal evaporation at low temperature, *Appl. Phys. A*, vol. 117, no. 2, pp. 815–822, 2014

[41] S.-W. Chen, C.-Y. Bai, C.-C. Jain, C.-J. Zhan, and C.-H. Koo, Durability of Indium Tin Oxide-Silver-Indium Tin Oxide Films against Moisture Investigated Through The Wettability of The Top Oxide Layer, *Mater. Trans.*, vol. 48, no. 8, pp. 2230–2234, 2007

[42] K. Maruyama, Toshiro and Fukui, Indium tin oxide thin films prepared by chemical vapor deposition, *J. Appl. Phys.*, vol. 70, no. 1992, pp. 3848–3851, 1999

[43] F. Kurdesau, G. Khripunov, A. F. da Cunha, M. Kaelin, and A. N. Tiwari, Comparative study of ITO layers deposited by DC and RF magnetron sputtering at room temperature, *J. Non. Cryst. Solids*, vol. 352, no. 9–20

SPEC. ISS., pp. 1466–1470, 2006

[44] Metal Prices in the United States Through 2010 By U.S. Geological Survey National Minerals Information Center staff, pag 66-67. pp. 66–67

[45] https://infinity-h2020.eu/.

[46] http://cordis.europa.eu/project/rcn/193859_en.html.

[47] A. Muthukumar, Fluorine doped tin oxide (FTO) thin film as transparent conductive oxide (TCO) for photovoltaic applications, *AIP Conf. Proc.*, vol. 1, pp. 710–711, 2013

[48] A. E. Rakhshani, Y. Makdisi, and H. A. Ramazaniyan, Electronic and optical properties of fluorine-doped tin oxide films, *J. Appl. Phys.*, vol. 83, no. 2, pp. 1049–1057, 1998

[49] Ü. Özgür et al., A comprehensive review of ZnO materials and devices, *J. Appl. Phys.*, vol. 98, no. 41301, 2005

[50] T. Minami, H. Nanto, and S. Takata, Highly Conductive and Transparent Aluminum Doped Zinc Oxide Thin Films Prepared by RF Magnetron Sputtering, *Jap. J. Appl. Phys.*, vol. 23, no. Part 2, No. 1, p. L280, 1984

[51] K. H. Kim, K. C. Park, and D. Y. Ma, Structural, electrical and optical properties of aluminum doped zinc oxide films prepared by radio frequency magnetron sputtering, *J. Appl. Phys.*, vol. 81, no. 12, pp. 7764–7772, 1997

[52] J. Hu and R. Gordon, Textured aluminum-doped zinc oxide thin films from atmospheric pressure chemical-vapor deposition, *J. Appl. Phys.*, vol. 71, p. 880, 1992

[53] W. Tang and D. C. Cameron, Aluminum-doped zinc oxide transparent conductors deposited by the sol-gel process, *Thin Solid Films*, vol. 238, no. 1, pp. 83–87, 1994

[54] A. V. Singh and R. M. Mehra, Highly conductive and transparent aluminum-doped zinc oxide thin films prepared by pulsed laser deposition in oxygen ambient, *J. Appl. Phys.*, vol. 90, no. 11, pp. 5661–5665, 2001

[55] V. Assunção et al., New challenges on gallium-doped zinc oxide films prepared by r.f. magnetron sputtering, *Thin Solid Films*, vol. 442, no. 1–2, pp. 102–106, 2003

[56] N. Ito, Y. Sato, P. K. Song, A. Kaijio, K. Inoue, and Y. Shigesato, Electrical and optical properties of amorphous indium zinc oxide films, *Thin Solid Films*, vol. 496, no. 1, pp. 99–103, 2006

[57] S. Tricot, C. Boulmer-Leborgne, M. Nistor, E. Millon, and J. Perrière, Dynamics of a pulsed-electron beam induced plasma: application to the growth of zinc oxide thin films, *J. Phys. D. Appl. Phys.*, vol. 41, no. 17, p. 175205, 2008

[58] M. Nistor, N. B. Mandache, and J. Perrière, Pulsed electron beam deposition of oxides thin films, *J. Phys. D. Appl. Phys.*, vol. 41, no. 16, p. 165205, 2008

[59] M. Nistor, F. Gherendi, M. Magureanu, and N. B. Mandache, Time-resolved spectroscopic study of a pulsed electron beam ablation plasma, *J. Optoelectron. Adv. Mater.*, vol. 7, no. 2, pp. 979–984, 2005

[60] R. Henda, O. Al-Shareeda, A. McDonald, and A. Pratt, Deposition of iron pyrite via pulsed electron ablation, *Appl. Phys. A Mater. Sci. Process.*, vol. 108, no. 4, pp. 967–974, 2012

[61] Q. Jiang, F. Matacotta, M. Konijnenberg, G. Müller, and C. Schultheiss, Deposition of $YBa2Cu3O_{7-x}$ thin films by channel-spark pulsed electron beam ablation, *Thin Solid Films*, vol. 241, no. 1–2, pp. 100–102, 1994

[62] S. Rampino, F. Bissoli, E. Gilioli, and F. Pattini, Growth of $Cu(In,Ga)Se_2$ thin films by a novel single-stage route based on pulsed electron deposition, *Prog. Photovolt Res. Appl.*, vol. 21, no. 4, p. 588, 2011

[63] G. Muller and C. Schultheiss, Deposition by means of pulsed electron beam ablation, *High-Power Part. Beams, 1994 …*, 1994

[64] M. D. Strikovski, J. Kim, and S. H. Kolagani, Plasma Energetics in Pulsed Laser and Pulsed Electron Deposition, in *Springer Handbook of Crystal Growth*, 2010, pp. 1193–1211

[65] S. Tricot, N. Semmar, L. Lebbah, and C. Boulmer-Leborgne, ZnO sublimation using a polyenergetic pulsed electron beam source: numerical simulation and validation, *J. Phys. D. Appl. Phys.*, vol. 43, no. 6, p. 65301, 2010

[66] R. D. G Comsa, Simple model for the desorption of hydrogen from Ni surfaces, *Chem. Phys. Lett.*, vol. 49, no. 3, pp. 512--515, 1977

[67] R. J. Choudhary, S. B. Ogale, S. R. Shinde, V. N. Kulkarni, and T. Venkatesan, Pulsed-electron-beam deposition of transparent conducting SnO_2 films and study of their properties, *Appl. Phys. Lett.*, vol. 84, no. 9, p. 1483, 2004

[68] V. C. Alan, N. B. Aran, R. Aline, and Y. Cedric, A Structural Study of Delafossite-type $CuInO_2$ Thin Films, *J. Phys. Conf. Ser.*, vol. 249, no. 1, p. 12045, 2010

[69] M. Yang et al., Copper doped nickel oxide transparent p-type conductive thin films deposited by pulsed plasma deposition, *Thin Solid Films*, vol. 519, no. 10, pp. 3021–3025, 2011

[70] J. Tauc, R. Grigorovici, and A. Vancu, Optical properties and electronic structure of amorphous Ge and Si, *Phys. Stat. Sol.*, vol. 15, p. 627, 1966

[71] E. H. Hall, On a New Action of the Magnet on Electric Currents, *Am. J. Math.*, vol. 2, no. 3, pp. 287–292, 1879

[72] L. J. Van der Pauw, A method of measuring specific resistivity and Hall effect of discs of arbitrary shape, *Philips Res. Reports*, vol. 13, pp. 1–9, 1958

[73] J. Potts, T. Smith, and H Cheng, Electron beam pumped lasing in ZnSe grown by molecular beam epitaxy, *Appl. Phys. Lett.*, vol. 50, no. 1, p. 336, 1987

[74] http://rredc.nrel.gov/solar/spectra/am1.5/.

[75] W. Witte, R. Kniese, A. Eicke, and M. Powalla, Influence of the Ga content on the $Mo/Cu(In,Ga)Se_2$ interface formation, *Conf. Rec. 2006 IEEE 4th World Conf. Photovolt. Energy Conversion, WCPEC-4*, vol. 1, pp. 553–

556, 2007

[76] J. Robertson, P. W. Peacock, M. D. Towler, and R. Needs, Electronic structure of p-type conducting transparent oxides, *Thin Solid Films*, vol. 411, no. 1, pp. 96–100, 2002

[77] R. B. Gall, N. Ashmore, M. A. Marquardt, X. Tan, and D. P. Cann, Synthesis, microstructure, and electrical properties of the delafossite compound $CuGaO_2$, *J. Alloys Compd.*, vol. 391, no. 1–2, pp. 262–266, 2005

[78] M. Veith, C. Bubel, and M. Zimmer, A novel precursor system and its application to produce tin doped indium oxide, *Dalt. Trans.*, vol. 40, no. 1, pp. 6028–6032, 2011

[79] J. C. C. Fan and J. B. Goodenough, X-ray photoemission spectroscopy studies of Sn-doped indium-oxide films, *J. Appl. Phys.*, vol. 48, no. 8, p. 3524, 1977

[80] S. Ishibashi, Y. Higuchi, Y. Ota, and K. Nakamura, Low resistivity indium–tin oxide transparent conductive films. II. Effect of sputtering voltage on electrical property of films, *J. Vac. Sci. Technol. A Vacuum, Surfaces, Film.*, vol. 8, no. 3, pp. 1403–1406, 1990

[81] J. P. Zheng and H. S. Kwok, Low resistivity indium tin oxide films by pulsed laser deposition, *Appl. Phys. Lett.*, vol. 63, no. 1, pp. 1–3, 1993

[82] T. Koida, T. Kaneko, and H. Shibata, Carrier Compensation Induced by Thermal Annealing in Al-Doped ZnO Films, *Materials (Basel).*, vol. 10, no. 141, pp. 1–18, 2017

[83] F. Pattini et al., Comparative study about Al-doped zinc oxide thin fi lms deposited by Pulsed Electron Deposition and Radio Frequency Magnetron Sputtering as Transparent Conductive Oxide for Cu $(In,Ga)Se_2$ - based solar cells, *Thin Solid Films*, vol. 582, pp. 317–322, 2015

[84] H. Kim and C. M. Gilmore, Transparent conducting aluminum-doped zinc oxide thin films for organic light-emitting devices, *Appl. Phys. Lett.*, vol. 76, no. 3, p. 259, 2000

[85] L. Pereira et al., Highly stable transparent and conducting gallium-doped zinc oxide thin films for photovoltaic applications, *Sol. Energy Mater. Sol. Cells 92*, vol. 92, pp. 1605–1610, 2008

[86] R. Menner, S. Paetel, W. Wischmann, and M. Powalla, Indium zinc oxide window layer for high-ef fi ciency $Cu(In,Ga)Se_2$ solar cells, *Thin Solid Films*, vol. 634, pp. 160–164, 2017

[87] N. Cavallari et al., Low temperature deposition of bifacial CIGS solar cells on Al-doped Zinc Oxide back contacts, *Appl. Surf. Sci.*, vol. 412, pp. 52–57, 2017

[88] J. Benemann, O. Chehab, and E. Schaar-Gabriel, Building-integrated PV modules, *Sol. Energy Mater. Sol. Cells*, vol. 67, no. 1–4, pp. 345–354, 2001

[89] J. P. Singh, T. M. Walsh, and A. G. Aberle, A new method to characterize bifacial solar cells, *Prog. Photovolt Res. Appl.*, vol. 15, no. February 2013, pp. 659–676, 2007

[90] A. Cuevas, A. Luque, J. Eguren, and J. del Alamo, 50 Per cent more output power from an albedo-collecting

flat panel using bifacial solar cells, *Sol. Energy*, vol. 29, no. 5, pp. 419–420, 1982

[91] H. Mori, U.S. patent No. 3,278,811

[92] Y. Ohtsuka, H, Sakamoto, M, Tsutsui, K, Yazawa, J. Wiley, S. Energy, and S. P. Corp, Bifacial Silicon Solar Cells with 21.3 Front Efficiency and 19.8 Rear Efficiency, *Prog. Photovoltaics Res. Appl.*, vol. 8, pp. 385–390, 2000

[93] S. Saha, R. A. Rao, L. Mathew, M. Ainom, and S. K. Banerjee, A novel low-cost method for fabricating solar cells, *Conf. Rec. IEEE Photovolt. Spec. Conf.*, pp. 2250–2253, 2012

[94] J. Wu et al., Bifacial dye-sensitized solar cells: a strategy to enhance overall efficiency based on transparent polyaniline electrode., *Sci. Rep.*, vol. 4, p. 4028, 2014

[95] F. Fu et al., Low-temperature-processed efficient semi-transparent planar perovskite solar cells for bifacial and tandem applications, *Nat. Commun.*, vol. 6, p. 8932, 2015

[96] A. Wangperawong et al., Bifacial solar cell with SnS absorber by vapor transport deposition, *Appl. Phys. Lett.*, vol. 105, no. 17, 2014

[97] M. Espindola-Rodriguez, Y. Sánchez, H. Xie, D. Sylla, E. Saucedo, and M. Placidi, Efficient Bifacial $Cu_2ZnSnSe_4$ Solar Cells, *Photovolt. Spec. Conf.*, pp. 8–10, 2015

[98] R. Guerrero-Lemus, R. Vega, T. Kim, A. Kimm, and L. E. Shephard, Bifacial solar photovoltaics - A technology review, *Renew. Sustain. Energy Rev.*, vol. 60, pp. 1533–1549, 2016

[99] ITRPV - International Technology Roadmap for Photovoltaic: 2013 Results.

[100] H. Ohtsuka, M. Sakamoto, M. Koyama, K. Tsutsui, T. Uematsu, and Y. Yazawa, Characteristics of bifacial solar cells under bifacial illumination with various intensity levels, *Prog. Photovoltaics Res. Appl.*, vol. 9, no. 1, pp. 1–13, 2001

[101] L. Kreinin, N. Bordin, N. Eisenberg, P. Grabitz, S. Hasenauer, and D. Obhof, Industrial production of bifacial solar cells: design principles and latest achievements, in *Konstanz, Bifi Workshop*, 2012

[102] T. Nakada, Y. Hirabayashi, T. Tokado, D. Ohmori, and T. Mise, Novel device structure for $Cu(In,Ga)Se_2$ thin film solar cells using transparent conducting oxide back and front contacts, *Sol. Energy*, vol. 77, no. 6, pp. 739–747, 2004

[103] E. J. Friedrich, J. F. Trigo, J. Ramiro, C. Guillén, J. M. Merino, and M. León, Effect of the ITO substrate on the growth of $Cu(In,Ga)Se_2$, CuGa3Se5, CuGa5Se8 and CuIn3Se5 thin films by flash evaporation, *J. Phys. D. Appl. Phys.*, vol. 42, no. 8, p. 85401, 2009

[104] T. Nakada, Microstructural and diffusion properties of CIGS thin film solar cells fabricated using transparent conducting oxide back contacts, *Thin Solid Films*, vol. 480–481, pp. 419–425, 2005

[105] P. J. Rostan, J. Mattheis, G. Bilger, U. Rau, and J. H. Werner, Formation of transparent and ohmic

ZnO:Al/$MoSe_2$ contacts for bifacial Cu(In,Ga)Se_2 solar cells and tandem structures, *Thin Solid Films*, vol. 480–481, pp. 67–70, 2005

[106] Y. Liu, Y. Sun, and A. Rockett, A new simulation software of solar cells - WxAMPS, *Sol. Energy Mater. Sol. Cells*, vol. 98, pp. 124–128, 2012

[107] C. Maragliano, L. Colace, M. Chiesa, S. Rampino, and M. Stefancich, Three-dimensional Cu(InGa)Se_2 photovoltaic cells simulations: Optimization for limited-range wavelength applications, *IEEE J. Photovoltaics*, vol. 3, no. 3, pp. 1106–1112, 2013

[108] S. Rampino et al., 15% efficient Cu(In,Ga)Se_2 solar cells obtained by low-temperature pulsed electron deposition, *Appl. Phys. Lett.*, vol. 101, no. 13, pp. 1–5, 2012

[109] J. Chantana, H. Arai, Y. Niizawa, and T. Minemoto, Ohmic-like contact formation at the rear interface between Cu(In,Ga)Se_2 and ZnO:Al in a lift-off Cu(In,Ga)Se_2 solar cell, *Thin Solid Films*, vol. 616, pp. 17–22, 2016

[110] L. El Mir and J. C. Bourgoin, Defect-Enhanced Electron Transport through Semiconductor Barriers, *Phys. Status Solidi*, vol. 207, no. 2, pp. 577–594, 1998

[111] Q. Sun, K.-B. Kim, and C.-W. Jeon, Characteristics of Ga-Rich Cu(In,Ga)Se_2 Solar Cells Grown on Ga-Doped ZnO Back Contact, *J. Nanosci. Nanotechnol.*, vol. 16, no. 5, pp. 5053–5057, 2016

[112] V. Bhosle, J. T. Prater, F. Yang, D. Burk, S. R. Forrest, and J. Narayan, Gallium-doped zinc oxide films as transparent electrodes for organic solar cell applications, *J. Appl. Phys.*, vol. 102, no. 2, p. 23501, 2007

[113] F. Mollica et al., Light absorption enhancement in ultra-thin Cu(In,Ga)Se_2 solar cells by substituting the back-contact with a transparent conducting oxide based reflector, *Thin Solid Films*, vol. 633, pp. 202–207, 2017

[114] S. H. Moon et al., Printable, wide band-gap chalcopyrite thin films for power generating window applications, *Sci. Rep.*, vol. 4, no. 1, p. 4408, 2015

[115] M. Mazzer et al., Bifacial CIGS solar cells grown by Low Temperature Pulsed Electron Deposition, *Sol. Energy Mater. Sol. Cells*, vol. 166, no. August 2016, pp. 247–253, 2017

[116] O. Meglali, A. Bouraiou, N. Attaf, and M. S. Aida, The effect of Al and In concentrations on the properties of electrodeposited Cu(In,Al)Se_2 using two electrode system without the addition of complexing agents, *Optik (Stuttg).*, vol. 140, pp. 709–717, 2017

Abbreviations

ABS	Absorbance
AZO	ZnO:Al
AZO2	ZnO:Al 2%wt
AZO5	ZnO:Al 5%wt
BFSC	Bifacial solar cell
BIPV	Building integrated photovoltaic
CBD	Chemical bath deposition
CIGS	$Cu(In,Ga)Se_2$
EDS	Energy dispersive X-ray spectroscopy
EF	Fermi level energy
EG	Energy gap
EHT	Electron high tension
EQE	External quantum efficiency
FF	Fill factor
FTO	Fluorine tin oxide
GAZO	ZnO:Ga
GAZO2	ZnO:Ga 2%wt
GGI	[Ga]/[Ga+In]
INZO	ZnO:In
INZO2	ZnO:In 2%wt
INZO9	ZnO:In 9%wt
IR	Infrared
ITO	Indium tin oxide
I-V	Current vs Voltage
J	Current density
JSC	Short circuit current
J-V	Current density vs Voltage
LTPED	Low temperature pulsed electron deposition
n	Carrier concentration
PED	Pulsed electron deposition
PV	Photovoltaic
PVD	Physical vapor deposition
R□	Sheet resistance
RS	Series resistance
RSH	Shunt resistance
RT	Room temperature
RTA	Rapid thermal annealing
SEM	Scanning electron microscope
SIMS	Secondary ion mass spectroscopy
SLG	Soda lime glass
T	Temperature
T%	Transmittance
TCO	Transparent conductive oxide
UV	Ultraviolet
UZO	Undoped zinc oxide
VIS	Visible
VOC	Open circuit voltage
XRD	X-ray diffraction
α	Absorption coefficient
η	Efficiency
λ	Wavelength
μ	Carrier mobility
ρ	Resistivity